CORA Cork Open Research Archive
Cartlann Taighde Oscailte Chorcaí

Title	Bedrock target analysis for ROV rockdrill sampling and existing sample stratigraphic and mineralogical verification (BeTar_drill)
Authors	Strachan, Ruaihri
Publication date	2021-03
Original Citation	Strachan, R. 2021. Bedrock target analysis for ROV rockdrill sampling and existing sample stratigraphic and mineralogical verification (BeTar_drill). MRes Thesis, University College Cork.
Type of publication	Masters thesis (Research)
Rights	© 2021, Ruaihri Strachan. - https://creativecommons.org/licenses/by-nc-nd/4.0/
Download date	2026-11-06 18:00:31
Item downloaded from	https://hdl.handle.net/10468/11891

UCC
University College Cork, Ireland
Coláiste na hOllscoile Corcaigh

Ollscoil na hÉireann, Corcaigh

National University of Ireland, Cork



Bedrock Target analysis for ROV Rockdrill sampling and existing sample stratigraphic and mineralogical verification (BeTar_drill)

Thesis presented by

Ruaihri Strachan, B.Sc. (Hons)

for the degree of

Masters of Science

University College Cork

Geology, School of Biological, Earth and Environmental Sciences

Head of School: Prof. Andrew Wheeler

Supervisor(s): Prof. Andrew Wheeler, Dr. Aaron Lim, Dr. Pat Meere, Dr. Richard Unitt

March 2021

Contents

1. Introduction 1

1.1. Seafloor geological investigation 1

1.1.1. Seabed mapping 1

1.1.2. Remotely Operated Vehicles 3

1.1.3. Structure-from-Motion Photogrammetry 6

1.1.4. Submersible rock drilling 9

1.2. Regional setting 11

1.2.1. Irish Atlantic Margin 11

1.2.2. Study site 12

1.3. Aims and Objectives 13

2. Materials and Methods 15

2.1. MBES data 15

2.2. ROV video and still imagery 18

2.3. Bedrock suitability mapping 20

2.3.1. Terrain variables 20

2.3.2. Spatial analysis 22

2.3.3. Accuracy assessment 23

2.4. Photogrammetry 24

2.5. ROV rock sampling 27

2.6. Sample analysis 28

2.6.1. Raman spectroscopy 28
3. Results 31
3.1. Bathymetry and backscatter 31
3.2. ROV video 33
3.3. Rock type distribution 37
3.4. Suitability modelling 39
3.5. DOMs 54
3.6. Petrography 54
4. Discussion 57
4.1. Bedrock mapping in the PBC 57
4.2. Geology of the PBC 59
4.3. Outcrop models 61
4.4. Implications 62
5. Conclusions 64
References 66
Appendices 79
Appendix A – Datamining results 80
Appendix B – Bedrock observations 89
Appendix C – Outcrop models 90

List of figures

Figure 1: Main elements of a typical work class ROV setup. 5

Figure 2: Simplified summary of SfM photogrammetric modelling 8

Figure 3: Summary of deep sea drilling operations in the last 50 years. 10

Figure 4: Map of Irish offshore 12

Figure 5: MBES data for PBC study area with transect and sampling locations 16

Figure 6: Backscatter data for PBC study area 17

Figure 7: Summary of workflow used for SfM photogrammetric modelling 26

Figure 8: Hydraulic rockdrill front of the Holland 1 ROV. 27

Figure 9: Rock samples (R1 and R2) bagged and thin sections for each. 28

Figure 10: Image of thin section surface, with approximate area of analysis 29

Figure 11: High resolution image mosaic of sample R1. 30

Figure 12: Slope gradient maps (shaded) describing features in the study area 31

Figure 13: Rock types identified in the PBC based on ROV video footage. 36

Figure 14: Footage from the shallower upslope area of the PBC. 37

Figure 15: Box whisker plots for each of the quantitative terrain variables. 40

Figure 16: Backscatter data (left) with reclassified backscatter (right) 41

Figure 17: Bathymetry data (left) with reclassified bathymetry (right) 42

Figure 18: Derived slope layer (left) with reclassified slope (right) 43

Figure 19: Derived aspect layer (left) with reclassified aspect (right) 44

Figure 20: Derived curvature (left) with reclassified mean curvature (right). 45

Figure 21: Derived broad scale BPI layer (left) with reclassified BPI (right). 46

Figure 22: Derived fine scale BPI layer (left) with reclassified BPI (right). 47

Figure 23: Derived roughness layer (left), with reclassified roughness (right). 48

Figure 24: Derived rugosity layer (left) with reclassified rugosity (right)). 49

Figure 25: Map of PBC study area showing output of normalised BSI.....50

Figure 26: BSI results plotted over terrain in Zone 1, with features labelled. 51

Figure 27: BSI results plotted over terrain in Zone 2, with features labelled. 52

Figure 28: BSI results plotted over terrain in Zone 2, with features labelled. 53

Figure 29: Petrology and mineralogy for smaple R1.....55

Figure 30: Patrography and mineralogy for sample R2. 56

Figure 31: Overview of key datamining findings.. 80

Figure 32: Findings from TTR13 (courtesy of GSI). 88

Figure 33: Overview map of PBC bedrock observations and validation data 89

Figure 34: Model 1 from the PBC (approx.. 20 m in length).....90

Figure 35: Model 2 from the PBC (approx.. 5 m in length).....91

Figure 36: Model 3 from the PBC (approx.. 4 m in length).....92

Figure 37: Model 4 from the PBC (approx.. 3 m in length).....93

Figure 38: Model 5 from the PBC (approx.. 12 m in length).....94

Figure 39: Model 6 from the PBC (approx.. 13 m in length).....95

Figure 40: Model 7 from the PBC (approx.. 12 m in length).....96

Figure 41: Model 8 from the PBC (approx.. 9 m in length).....97

Figure 42: Model 9 from the PBC (approx.. 2 m in length).....97

Figure 43: Model 10 from the PBC (approx.. 7 m in length). 98

Figure 44: Model 11 from the PBC (approx.. 5 m in length). 99

Figure 45: Model 12 from the PBC (approx.. 1.5 m in length). 100

Figure 46: Model 13 from the PBC (approx.. 3 m in length). 101

Figure 47: Model 14 from the PBC (approx.. 3 m in length). 101

Figure 48: Model 15 from the PBC (approx.. 9 m in length). 102

Figure 49: Model 16 from the PBC (approx.. 10 m in length). 103

Figure 50: Model 17 from the PBC (approx.. 4 m in length). 104

List of tables

Table 1: Summary of available robotic seafloor drilling systems.....11

Table 2: Summary of ROV dives used for this study. 18

Table 3: Summary of terrain variables used for bedrock suitability mapping. 21

Table 4: Summary of 3D models developed during the study). 54

Table 5: Potential outcrop exposure encountered during SeaRover 1 (2017). 82

Table 6: Potential outcrop exposure encountered during SeaRover 2 (2018). 83

Table 7: Potential outcrop exposure encountered during SeaRover 3 (2019). 84

Table 8: Summary of samples collected during CE14011. 85

Table 9: Summary of dredge samples recovered during CE11017.....85

Table 10: Summary of geological samples acquired by IFREMER. 87

Abbreviations

AUV Autonomous Underwater Vehicle

BPI Bathymetric Position Index

BSI Bedrock Suitability Index

CTD Conductivity Temperature Depth

CWC Cold-water coral

DOM Digital Outcrop Model

DP Dynamic Positioning

DVL Doppler Velocity Log

IAM Irish Atlantic Margin

IQR Interquartile Range

LARS Launch and Recovery System

MBES Multibeam echosounder

PBC Porcupine Bank Canyon

ROV Remotely Operated Vehicle

SAC Special Area of Conservation

SfM Structure-from-Motion

SIFT Scale Invariant Feature Transform

SLAM Simultaneous Localization and Mapping

TCU Topside Control Unit

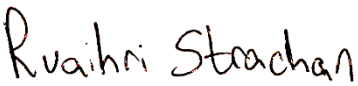
TMS Tether Management System

USBL Ultrashort baseline

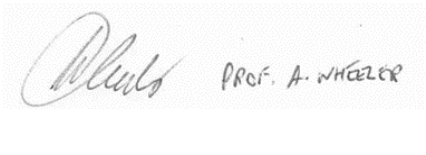
VOM Virtual Outcrop Model

Declaration

This is to certify that the work I am submitting is my own and has not been submitted for another degree, either at University College Cork or elsewhere. All external references and sources are clearly acknowledged and identified within the contents. I have read and understood the regulations of University College Cork concerning plagiarism.

Signed 

Ruaihri Strachan, author.

Signed 

Professor Andy Wheeler and Dr. Aaron Lim, primary supervisors.

Acknowledgements

My deepest appreciation goes to a number of people in relation to this masters, and the 18 months which surround it.

Firstly, I would like to sincerely thank the crew of RV Celtic Explorer and the Holland 1 ROV. As a fresh graduate, you gave me your time and advice while I was learning, when I was figuring out what I wanted to continue doing, and it ultimately led me to pursuing this incredible research project, and now a career, a path not many people get to go down. For this I will always be grateful, and that message goes out to David O'Sullivan and Oisín Callery also, who not only gave me advice, they gave me opportunity and tools which would prepare me for my masters and beyond.

I'd like to thank the School of BEES, the staff and the students within it. Even though it was a flying visit, I was made feel welcome the second I walked into the real republic, with a funny accent, and not much of a clue where I was going. From the first office all the way to the cave, thank you to the people I've shared a space with, be it with the research, lunches or kicking a ball around the back of the Butler Building. A special mention to Christine, thank you for sorting things when I couldn't!

I'd like to thank Xavier Monteys and Adriano Mazzini for their detailed discussions relating to TTR13. I'd also like to thank Peter Heath, Ronan O'Toole, and Aileen Bohan for their help and advice when it came to data or seabed mapping in general.

With regards to the rock sample analysis, I would like to thank Mohit and Richard for introducing me to the Raman, for their extensive help in the lab early on in the project and throughout the remote working of 2020. I'd like to also thank Odhrán, who took me under his wing in many ways with regards to the Raman analysis, and always made time to discuss the rock samples.

With regards to the supervisory team, I would like to express my gratitude to Richard, Andy, and Pat for their massive boosts on confidence and moral when I had blinders on, especially Pat. Aaron, you took a chance on me coming into the group, that chance I will never forget, and I have valued every moment working together through this masters and offshore. I'm lucky to call you a colleague, let alone a friend who I highly regard as a role model and aspire to move forward with research the way you've shown me.

The dream team, where can I start. John, Ev, Larissa, Ger, Luke, Siobhán. Felix, Alicia. It's rare to fall into such a sound bunch of people, with a high graft and work ethic, and even better craic. I'll miss the cave big time, the bouncing of ideas (and abuse), but I know that this is not the end, and I'm excited to see you all again very soon.

I'd like to thank my parents, Ian and Patricia, for supporting me through my notions when it comes to the deep sea. My brother Liam, for listening and pushing me on when times got tough during the year, and Jake, for always being there. I'd like to thank my

girlfriend Lorna, and her family, Bernadette, Kevin and Colum, Kitty and Cat. An unexpected weekend restriction ended in 3 months of me being in your home, and you never made me feel out of place. I sincerely thank you for this. Lorna, you know how to keep me on the straight and narrow, and thank you for being so kind. I won't let you down.

Thank you Flash, and Blue, for always knowing when to come in and get me away from the screen.

Funding acknowledgements

This research uses data and survey results acquired during a project undertaken on behalf of the Irish Shelf Petroleum Studies Group (ISPSG) of the Irish Petroleum Infrastructure Programme Group 4. . Shiptime relating to this research is funded under the National Development Plan, National Grant-aided Shiptime Programme. SeaRover is part supported by the Irish government and the European Maritime and Fisheries Fund as part of the EMFF Operational Programme (2014 – 2020).

Ruaihri Strachan is supported by research grant IS18/04b, funded by the Irish Shelf Petroleum Studies Group (ISPSG) of the Irish Petroleum Infrastructure Programme (PIP) Group 4 (and its member companies).

Abstract

The dynamic seascapes found in continental margin settings generally host many vertical structures, such as fault escarpments and submarine canyon systems. This terrain is exemplified on the Irish Atlantic Margin (IAM) by the Porcupine Bank Canyon (PBC). Bedrock has been found here in the past, however, surveying in these areas continues to be a difficult task due to issues regarding access and sampling conditions. As a result, a lack of both knowledge and detail generally exists for offshore outcrop, which is in stark contrast to typical terrestrial geological data. Modern advances in marine robotics and seafloor imaging techniques has allowed for renewed offshore scientific expeditions in deep marine settings, being guided by high-resolution topographical data (gathered through multibeam echosounding) and Remotely Operated Vehicles (ROVs). Here, updated high-resolution bathymetric data, coupled with bedrock samples that have been drilled in-situ and a series of video transects spread out across the PBC have been used to develop methods for offshore geological 'fieldwork', through marine bedrock mapping and sample characterisation, whilst also using footage to recreate the seafloor through Structur-from-Motion (SfM) photogrammetry, in order to produce accurately scaled, lifelike, geological outcrop models.

The steps presented within this thesis with regards to bedrock mapping tie in with marine geomorphometry and habitat suitability modelling techniques. This attempts to quantitatively describe the surface of the seafloor, and identify key terrain attributes for which bedrock has previously been encountered and proven to occur. Further terrain data can then be reclassified based on the interquartile ranges (IQRs) for these characteristic sections, identifying potential occurrence of outcrop in non-surveyed areas. This study applies these methods across more than 2000 km^2 of canyon terrain,

and have yielded a 60% accuracy for bedrock predictions. These geological maps, coupled with high-definition video footage and physical rock samples, have allowed for a reappraisal of the bedrock encountered within the PBC. Bedrock samples indicate an underlying basement rock of lower greenschist facies metamorphosed igneous rocks.

17 detailed bedrock models have been constructed through the ROV footage also, and through this process, a robust method for applying SfM photogrammetry to offshore deep marine video imagery has been outlined. This has been successful across different surveys which were conducted in the PBC in recent years. The outputs from these models can further be used to record structural detail on bedrock exposed in these complex terrains, aid in distinguishing between lithologies, and also aid in planning future sampling opportunities (through rotary drilling or similar systems).

The methods outlined herein aim to enhance future geological studies in the Irish offshore, whilst also providing a potential tool for ecological studies which aim to target bedrock surrogates for investigation. Through large scale mapping programs, both in Ireland and abroad, public and institutional, a massive opportunity exists to build on from this PBC 'proof of concept' study, bridging the void which generally persists when it comes to knowledge on deep marine environments.

Keywords: marine geological mapping, submarine canyon, bathymetry, spatial analysis, continental margin, bedrock drilling, photogrammetry

1. Introduction

There is a noticeable contrast in detail between Ireland's terrestrial geological understanding and that of its offshore, an area ten times larger than the Irish mainland (www.gsi.ie/en-ie/data-and-maps). The inherent challenges with seabed surveying has resulted in limited groundtruthed observations for bedrock exposure on the seafloor in the region, and poor data quality persists amongst available data. Outcrop can generally be encountered in complex seascapes, and access to these terrains is often hindered by harsh and unpredictable working conditions. This study tackles these challenges, demonstrating how advancements in marine robotics and seabed mapping and imaging techniques can be applied to investigating the hard rock geology of the seafloor. The practical approaches presented in this thesis provide a possible solution to marine geological 'fieldwork', the methods of which can be further applied to future sampling opportunities and regional studies in the Irish offshore and further afield.

1.1. Seafloor geological investigation

1.1.1. Seabed mapping

The seabed is typically mapped using a multibeam echosounder (MBES), comprising a set of acoustic transceivers which detect and measure the returns from emitted 'beams' (athwart), and their reflected intensities (Lamarche and Lurton, 2018; Lurton and Lamarche, 2015; Wölfl et al., 2019). These systems are generally ship-mounted but can also be deployed on submersible vehicles (Escartín et al., 2017; Murton et al., 2019; Robert et al., 2017), enabling the acquisition of bathymetric data in complex or unconventional terrains. Higher acoustic frequencies will provide increased spatial

resolution over shorter athwartships ranges (De Moustier and Matsumoto, 1993). Thus, it is important to consider that MBES sounding density and resolution (i.e. footprint) decreases with depth as a consequence of the beam geometry and lower acoustic frequencies used (Wilson et al., 2007). Advances in bathymetric data collection and processing is benefitting advancements in the branch of marine geosciences known as geomorphometry (Lucieer et al., 2018), the quantitative analysis of the seafloor surface (Lecours et al., 2016; Pike, 2000). The analysis of corrected MBES data produces bathymetric models and acoustic backscatter mosaics that can be used to further identify the spatial distribution of local relief and other derivatives (such as slope and rugosity), bottom type and composition (Brown et al., 2019; Fonseca and Mayer, 2007; Misiuk et al., 2018; Schimel et al., 2018).

The ocean's on Earth cover 71% of its surface (Eakins and Sharman, 2010; Mayer et al., 2018, Weatherall et al., 2015), much of which has a scarce availability of information as a result of under sampling and limited observations (Levin et al., 2019). These marine environments are often said to have been 'mapped', which is a common misconception, as it has been done predominantly through satellite altimetry-derived bathymetry, producing the likes of the General Bathymetric Chart of the Oceans (GEBCO) (GEBCO, 2020). The resolutions available in this data for marine research purposes is often inadequate and lacks reasonable coverage and detail (Wölfl et al., 2019). Recent efforts are actively reducing these data gaps through international collaborations, including the Nippon Foundation – GEBCO Seabed 2030, a collaborative project between the Nippon Foundation of Japan and GEBCO aiming to produce the definitive map of the world ocean floor (Mayer et al., 2018; Wölfl et al., 2019), and EMODnet, a European initiative for collating and disseminating marine

data and a selection of useful products (EMODnet, 2020; Kaskela et al., 2019; Martín Míguez et al., 2019). A select few national mapping programmes (e.g. MAREANO (Norway), INFOMAR (Ireland) and MAREMAP (UK)) have achieved significant data coverage within their national territories, whilst also setting the standard at a global level for bathymetric mapping, prompting significant geoscience research and findings in offshore settings (Bøe et al., 2020; Dove et al., 2016; O'Toole et al., 2020; Thorsnes et al., 2016). A push to survey areas that are logistically and accessibly challenging has also evolved in recent years, examples of which include bathymetric charting of the polar regions on Earth (Arndt et al., 2013; Jakobsson et al., 2020), as well as the Five Deeps Expedition (Stewart and Jamieson, 2019), which successfully mapped and explored the five deepest points on Earth, and similar challenging expeditions, such as the recent search for the *Endurance* in the Weddell Sea (Dowdeswell et al., 2019, 2020).

1.1.2. Remotely Operated Vehicles

A Remotely Operated Vehicle (ROV) is a submersible machine which can be operated from the surface by means of a tether (a physical link) and control station (operators), using surface supplied power and communications for manoeuvring and task execution (Bogue, 2015; Christ and Wernli, 2014). ROVs can be categorised into three different classes (observation, inspection and working class), distinguishable by their size, weight and operational ratings (Capocci et al., 2017). These have evolved in recent decades from military and industry specific platforms, used in asset management, infrastructure inspection and recovery operations (McLean et al., 2018,

2020), to become a valuable resource for scientific research in deep marine settings (JNCC, 2018; Macreadie et al., 2018). Deep diving survey platforms exist that are manned submersible systems, such as the *Limiting Factor* (Caladan Oceanic), *Alvin* (WHOI), *Nautile* (IFREMER) and *Shinkai 6500* (JAMSTEC), which have the advantage of being untethered, and can be used to access and sample the seabed (Zhang et al., 2019). An Autonomous Underwater Vehicle (AUV) has this similar untethered advantage, however, their design is unsuitable for physical interaction with the seabed, and are used primarily for surveying large areas from a flying altitude above the seabed (Wynn et al., 2014).

Working class ROVs are generally heavy and robust submersible systems which can operate at great depth, routinely, and carry out meticulous tasks through the use of their manipulator arms and auxiliary systems (Christ and Wernli, 2014; Nakajoh et al., 2016; Sivčev et al., 2018). Typically, work class ROV systems will comprise of a high-spec ROV (Figure 1), a topside control unit (TCU) and umbilical tether connecting the surface to the submersible (providing power and a means of control for lights, cameras and thrusters, as well as sending live telemetry data between the ROV and TCU), which is occasionally connected to a submerged tether management system (TMS), but will often have a dedicated launch and recovery system (LARS), for routine deployment and recovery operations from a vessel using dynamic positioning (DP)(JNCC, 2018).

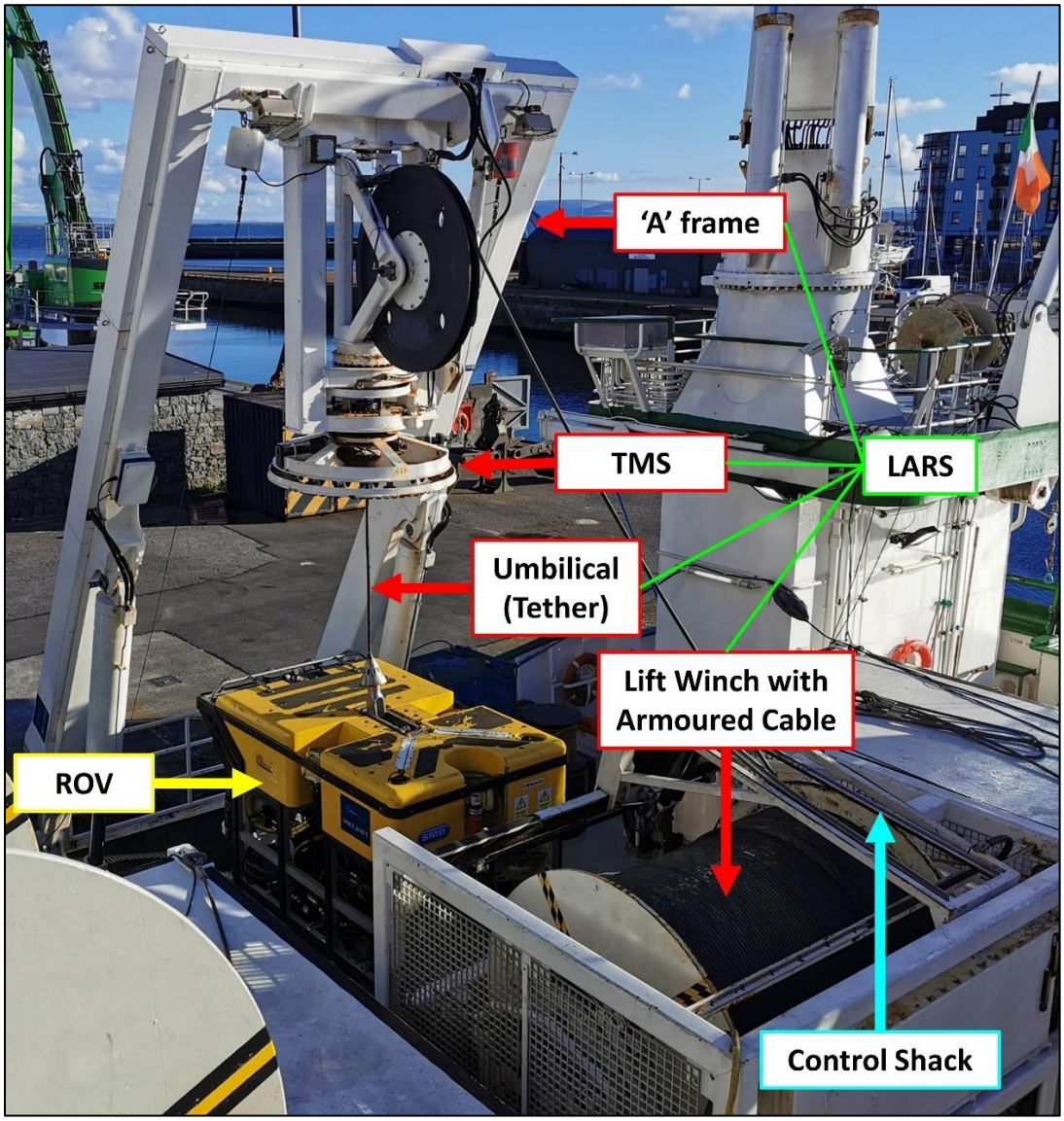


Figure 1: Main elements of a typical work class ROV setup (exemplified on back deck of RV Celtic Explorer by the Holland 1 ROV).

A work class ROV itself will have many onboard systems, including a means for navigation and positioning (e.g. ultrashort baseline (USBL) beacons and Doppler velocity logs (DVLs)), high-resolution visual recording capabilities (cameras, lighting and scaling lasers), means for taking and storing a range of samples (push cores, slurp hose, niskin bottles, debris collected by manipulator), and other environmental sensors such as conductivity temperature depth (CTD) sensors and sonar systems (see Section

2.2. for examples of the above based on the *Holland 1* ROV). The opportunities arising from work class ROVs being used for research purposes has coined the term 'science' class ROV (Hudson et al., 2005; Macreadie et al., 2018), as these machines can have operatable systems added or subtracted from the submersible or its skid based on surveying requirements, enabling pioneering deep sea exploration. Examples of pioneering research being conducted by science class ROVs include vertical mapping of benthic habitats (Huvenne et al., 2011; Robert et al., 2017) and the 2D and 3D studies of coral mound habitats (Lim et al., 2020, 2018).

1.1.3. Structure-from-Motion Photogrammetry

Structure-from-Motion (SfM) photogrammetry is capable of deriving the 3D structure of a surface or an environment through a series of overlapping and offset images (Westoby et al., 2012). This works similarly to how the human eye would determine the 3D aspect of an object (i.e. stereoscopic vision), by identifying correspondence between multiple features observed sequentially due to motion (Figure 2)(Storlazzi et al., 2016). After data collection the process in which SfM photogrammetry is generally conducted can be described as follows:

- Using a suitable dataset of input imagery (see Section 2.4. for further details), a matching process is performed across the sequential and overlapping images, identifying corresponding points or 'features' that are distinctly observed in two or more images (Shan et al., 2020). This initial process is known as Scale Invariant Feature Transform (SIFT), where keypoint descriptors (or features) allows the imagery data to be transformed into scale invariant coordinates

(Lowe, 2004). In many cases, the keypoints may be down sampled and tie points are identified, those matches considered most reliable, and further used to optimize available processing power in the image matching process (McCarthy and Benjamin, 2014).

- Feature points are then used to build a map of the environment within the imagery whilst simultaneously determining the location of the moving device which acquired the data, a process referred to as visually based Simultaneous Localization and Mapping (SLAM)(Jeon and Lee, 2020; Shan et al., 2020). A sparse point cloud is created from the arbitrary coordinate system calculated through the SIFT and SLAM process (Eltner and Sofia, 2020).
- Based on the image network geometry determined in the sparse point cloud, further dense image matching is conducted for resolving finer structures from multiple viewing angles, determining a corresponding 3D point for as many pixels as possible in the imagery (Eltner and Sofia, 2020). This allows for a dense point cloud to be created, which is further used to reconstruct the complex shape and textures of surfaces being modelled (Shan et al., 2020).
- For the imagery dataset, positioning information for the footage and scaling measurements (e.g. parallel lasers or lengths of scaled features) are used to accurately reference and position the model that has been created (Bayley and Mogg, 2020).

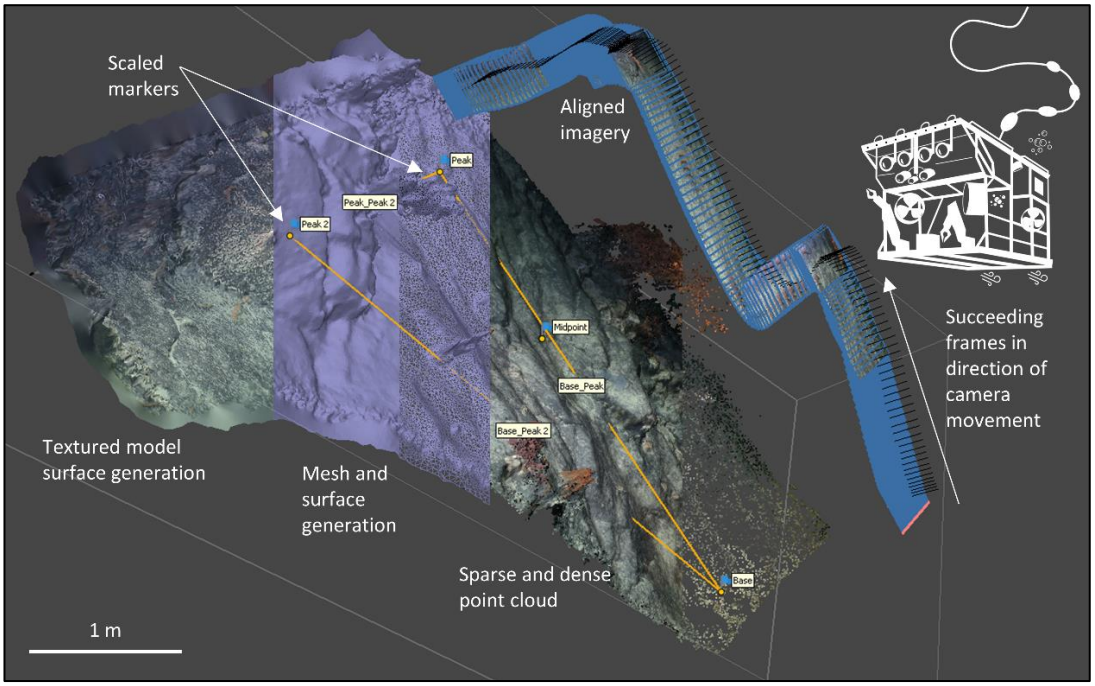


Figure 2: Simplified summary of SfM photogrammetric modelling process.

In the context of geosciences, SfM photogrammetry is proving itself to be an invaluable tool due to its reduced user supervision and required expertise for data acquisition (Micheletti et al., 2015; Smith et al., 2016), availability of low-cost commercial and open-source software for data processing and visualisation (Remondino et al., 2012), and their outputs of high-resolution elevation datasets for further geomorphic analyses (Carrivick et al., 2016; Eltner and Sofia, 2020). For deep marine settings, ROVs equipped with HD video cameras can now readily collect imagery that is adequate for SfM applications (Kocak et al., 2008).

Digital Outcrop Models (DOMs), also referred to as Virtual Outcrop Models (VOMs), are geometrically and visually lifelike representations of hard rock outcrops (Gonzaga et al., 2018; Marques et al., 2020). Due to their detail and accurate scaling, these data have become useful for virtually based geological fieldwork through interpretive software and experiences (Buckley et al., 2019; Caravaca et al., 2020; McCaffrey et

al., 2010, 2005; Nesbit et al., 2018). CloudCompare (CloudCompare, 2021) is an open source point cloud and 3D mesh editing and processing software often coupled with SfM photogrammetric methods (freely available at www.cloudcompare.org). A number of plugins for this software have proven useful for geological applications, including the Facets plugin (Dewez et al., 2016) and Compass plugin (Thiele et al., 2019). Facets uses a least square fitting algorithm to extract geological planes from a DOMs surface (Nagendran et al., 2019; Tung et al., 2018). Compass works on a *least-cost-path* approach, in which points of a DOM and their nearest neighbours are linked progressively between user-defined control points, with paths moving closer to the end point at each link in order to trace a geologically feasible structure (Thiele et al., 2017). There is a strong degree of semi-automation to using these plugins and software, making them suitable for a range of structural and detailed applications on DOMs, exemplified by studies such as the mapping of complex fracture systems (Massiot et al., 2017; Sayab et al., 2018).

1.1.4. Submersible rock drilling

Probing the Earth's interior has been a venture pursued since the late 1950s with the proposal of *Project Mohole*, a deep sea drilling program attempting to sample the crust and shallow mantle in order to further understand crustal composition, structure and its evolution (Umino et al., 2013). Since then, scientific ocean drilling has become a global effort, embodied today by the *International Ocean Discovery Program (IODP)* and its specialised drilling vessels (e.g. DV *JOIDES Resolution* and DV *Chikyu*), building on multiple deep sea drilling efforts in recent decades (Figure 3).

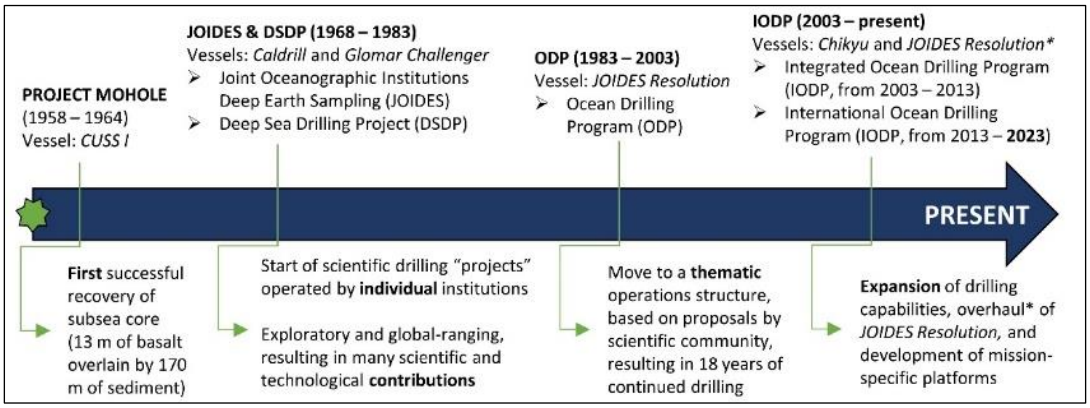


Figure 3: Summary of deep sea drilling operations in the last 50 years (Becker et al., 2019).

Remotely operated drilling systems have also evolved through dedicated platforms (Table 1) and opportunistic surveying strategies (Meredyk et al., 2020). Advantages of these systems include operation on available ships-of-opportunity, reduced mobilization costs, operations in rougher conditions due to the decoupling of the drill system and vessel, deep water sample storage avoiding midwater recovery infrastructure and rapid initiation of drilling operations at the seafloor in comparison to typical stabilization of a drill bit during deep sea spud-in operations (McGinnis et al., 2009). These advantages together significantly reduce logistical and financial constraints relating to typical drill rig and vessel operations, and have also prompted the availability of multiple robotic drilling systems available for scientific sampling today (Table 1).

System	Operator	Manufacturer	Type	Core	Depth (m)
3 m drill (USA)	U. of Washington	Williamson & Assoc.	Rod	3 m x 30 mm	5000
RD1 (UK)	BGS	British Geological Survey	Rod	6 m x 49 mm	2000
RD2 (UK)				15 m x 49 mm	3500
Oriented Rock Drill (UK)				0.8 m x 35 mm	6000
BMS1 (Japan)	JOGMEC	Williamson & Assoc.	Rod	20 m x 44 mm	6000
BMS2 (Japan)				20 m x 44 mm	6000
PROD (Australia)	Benthic Geotech	MD Research, Hugh Frazer & Assoc., Williamson & Assoc.	Rod	125 m x 54 mm	2000

MeBo (Germany)	MARUM	Prakla Bohrtechnik, Schilling Robotics	Rod (Wireline)	50 m x 80 mm	2000
ACS (India)	NIOT	Williamson & Assoc.	Wireline	150 m x 66 mm	3000
Rovdrill (USA)	Canyon Offshore	Perry Slingsby	Rod	20 m x 53.1 mm	3000
MBARI Drill (USA)	NDSF	MBARI, Holloway	Rod	1 m x 32 mm	3000

Table 1: Summary of available robotic seafloor drilling systems (adapted from McGinnis, 2009).

In a multidisciplinary context, bedrock sampling during surveys of opportunity are emerging through the use of ROVs equipped with bespoke rock sampling capacities, including manipulators and robotic grips (Backus et al., 2020; Trotter et al., 2019), jackhammer (Meredyk et al., 2020), and shallow rock coring capabilities (Murton et al., 2019). Although these types of surveys are maximising their resources, careful consideration must be taken when sampling true *in-situ* bedrock, as this can easily be misconstrued as erratic debris, which can often be in the vicinity of the study site (Huggett and Kidd, 1983; Kidd et al., 1990).

1.2. Regional setting

1.2.1. Irish Atlantic Margin

The Irish Atlantic Margin (IAM) has developed in relation to the southernmost evolution of the NE Atlantic region, a passive margin which has experienced a shared and complex development history (Doré et al., 1999; Stoker et al., 2017). Regional observations along the IAM include Precambrian, Caledonian and Variscan structural fabrics which have influenced basin development and segmentation, crustal thinning, variation in basin trends which have changed through time, phases of development from Permo-Triassic through Jurassic rifting, with intermissions of thermal subsidence and basin inversion, development of thick Cretaceous and Cenozoic successions, and major igneous activity (Naylor and Shannon, 2011, 2005).

1.2.2. Study site

The Porcupine Bank Canyon (PBC) incises the IAM at approximately 52°N and 15°W, between -480 m and -4400 m water depth (Figure 4), being one of the most substantial submarine canyons situated along the Irish continental margin (Dorschel et al., 2010). The head of the PBC cuts into the western fringes of the Porcupine Bank horst-block, progressing west through the small, elongated Cillian Basin (Tertiary) and South Bróna Basin (Mesozoic) horst margin sub-basins, extending into deeper waters on the eastern limits of the much larger Rockall Basin (Naylor et al., 1999; Naylor et al., 2001). The neighbouring Porcupine Basin graben is underlain by an extremely thinned crust (O'Reilly et al., 2006), with intrusions of mafic volcanic flows and sills (Gagnevin et al., 2018; Watremez et al., 2016).

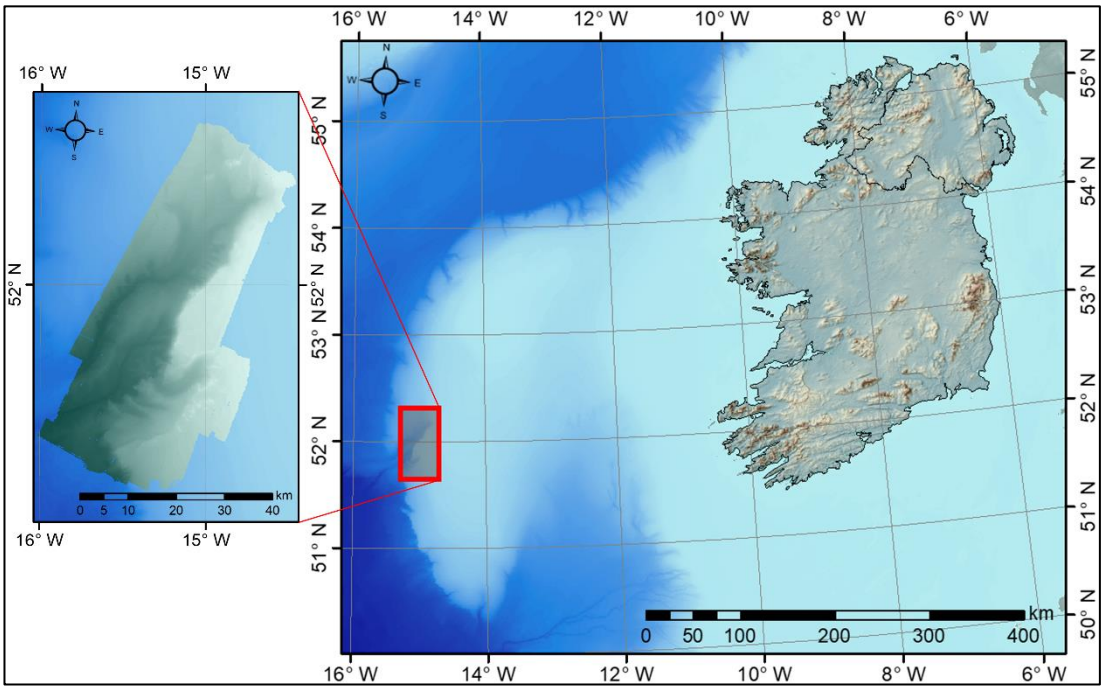


Figure 4: Map of Irish offshore showing part of the IAM (right) and location of the study area (left), the PBC, enclosed within the red box (bathymetry acquired through the EMODnet Bathymetry Consortium (2020)).

Submersible geological surveying and rock dredging slightly further south from the study site (Auffret and Auzende, 1986) has characterised a highly metamorphic basement, covered by Palaeozoic sediments and a tabular Mesozoic cover for this part of the IAM (Auffret et al., 1987; Auzende et al., 1989; D. G Masson et al., 1989). More recent side-scan sonar surveying through the use of the deep-towed submersible (TOBI) in the south of the study site has previously indicated the presence of rock outcrop and large escarpment features in deeper areas of the PBC (Dorschel et al., 2009; O'Reilly et al., 2001; Wheeler et al., 2005). Elongated escarpment features have also been identified along the SE upslope area of the study site through side-scan imagery (Ivanov et al., 2004) and recent multibeam bathymetry (Lim et al., 2020), where the accumulation of authigenic phosphatic deposits provide suitable hardgrounds for cold-water coral (CWC) mounds to develop and thrive (Mazzini et al., 2012). This part of the study site has since been designated as a Special Area of Conservation (SAC) in 2006, due to the diversity of species thriving in tandem with the carbonate mound structures and bottom conditions (Appah et al., 2020; Lim et al., 2020), followed by the rest of the PBC being designated in 2016, by the EU Habitats Directive (92/43/EEC).

1.3. Aims and Objectives

The overall aims of this study is to facilitate opportunities for the detailed characterisation of hard rock geology found in the marine environment. This broad scope is realised through the following objectives:

i. Develop transferable GIS methods to delimit typical seafloor terrain for bedrock exposure to occur in. This draws on habitat suitability modelling and marine geomorphometry techniques, where key geomorphic variables for deep marine outcrop can be derived from digital terrain datasets (e.g. bathymetry and backscatter data) and classified based on groundtruthed video observations from the PBC.

ii. Using the high resolution video observations to develop a robust method for creating detailed 3D models of deep marine outcrop imaged using an ROV via SfM photogrammetry. These models will be used to guide future ROV rock sampling opportunities in similar settings.

iii. Carry out a detailed petrographic analysis of seafloor bedrock samples collected *in situ* by means of a submersible rockdrill.

2. Materials and Methods

2.1. MBES data

MBES data used in this study were collected onboard RV *Celtic Explorer* (Figure 5). In 2019, regional mapping for the PBC area was completed using ship-based bathymetric mapping (Lim and Shipboard Party, 2019), building on initial renewed mapping efforts in the PBC from 2018 (Lim and Shipboard Party, 2018). This hull-mounted mapping was accomplished using Kongsberg Maritime EM302 operating at 30 kHz. The echosounder is integrated with a sound velocity probe, C-Nav navigation, a motion reference unit and dedicated processing unit. 864 soundings were acquired per ping. The survey was conducted at a constant speed of 8 kts in a series of parallel lines across the PBC, with an approximate swath width of 2500 m.

All data planning and acquisition was managed and stored using the Seafloor Information System (SIS) by Kongsberg Maritime. The data was stored as *.all files, and data processing was carried out using QPS Qimera for bathymetry, and QPS FMGT for backscatter.

The multibeam bathymetry and backscatter data (Figure 6) was projected to UTM Zone 28N and gridded at 25 m resolution. These data were exported as *.tif files for further spatial analysis.

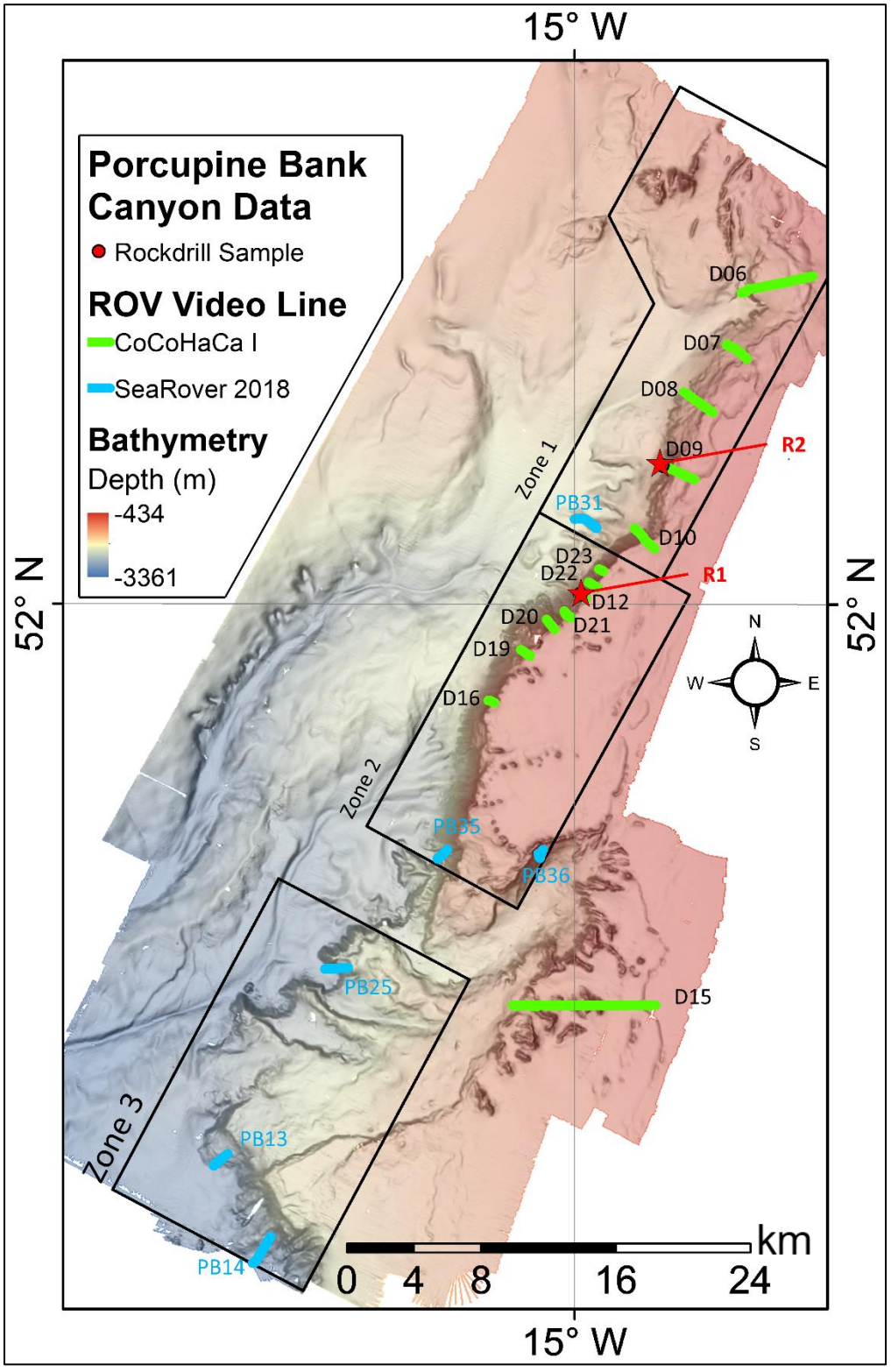


Figure 5: MBES data for PBC study area (25 m resolution; outlined in Figure 4), with transect and sampling locations plotted and three subzones delimited.

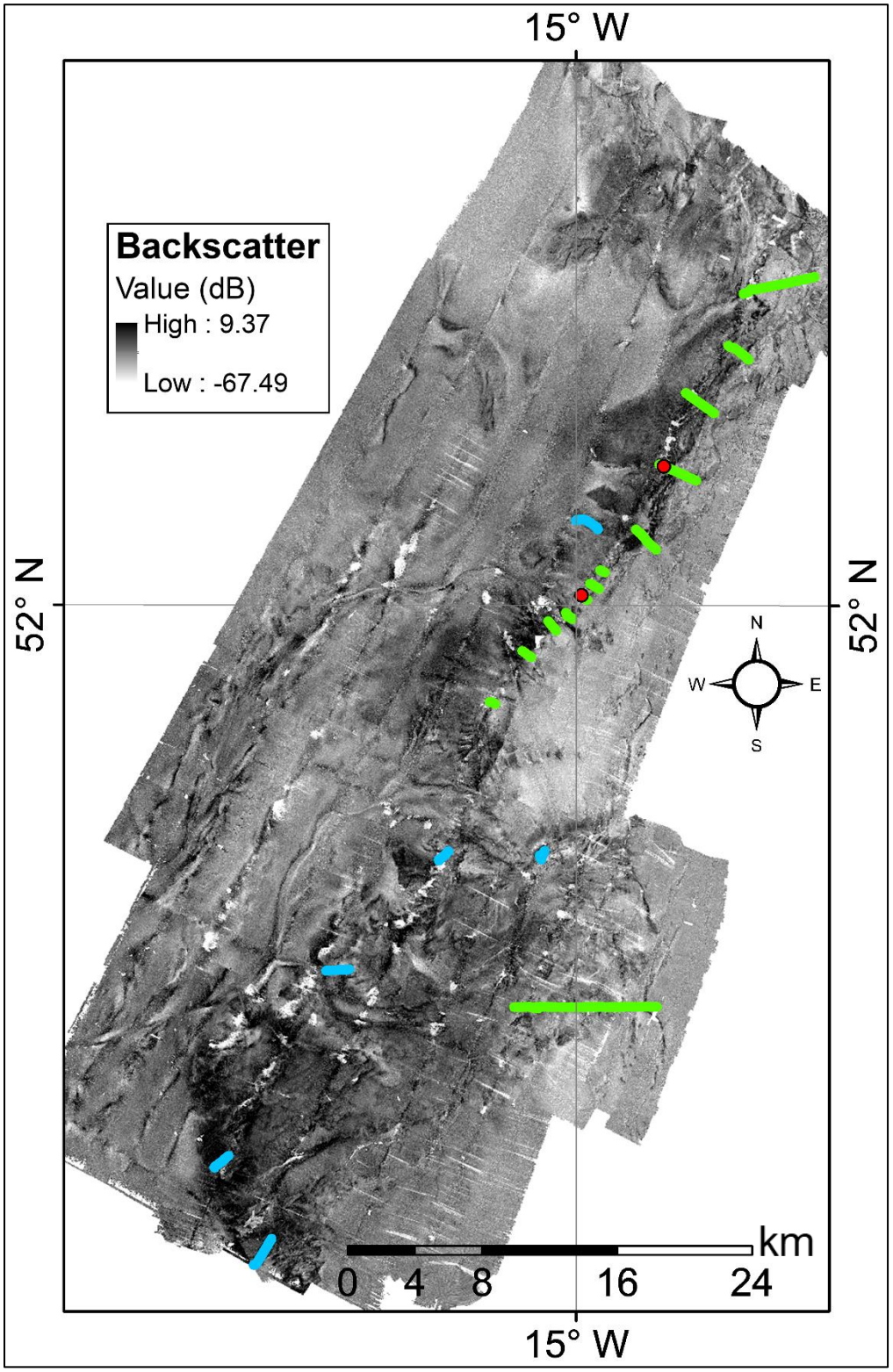


Figure 6: Backscatter data for PBC study area (25 m resolution), video lines included for reference.

2.2. ROV video and still imagery

Imagery data used in this study has been collected in the PBC using the Holland 1 ROV on board ILV *Granuaile* and RV *Celtic Explorer* during cruises QuERCi I and II (Wheeler and Shipboard Party, 2016, 2015), CoCoHaCa I (Wheeler and Shipboard Party, 2017) and SeaRover (O'Sullivan and Shipboard Party, 2018) (Figure 5; Table 2).

Survey	Date	Dive	Start Pos.	End Pos.	Depth (m)	Footage
CoCoHaCa I	23/06/2017	D06	52.1700 ; -14.8523	52.1792 ; -14.7886	1251 - 639	03:43:34
	23/06/2017	D08	52.1161 ; -14.9035	52.1050 ; -14.8781	1233 - 644	01:59:20
	24/06/2017	D09	52.0774 ; -14.9270	52.0682 ; -14.8933	1250 - 574	02:25:03
	24/06/2017	D10	52.0418 ; -14.9474	52.0316 ; -14.9305	1237 - 685	02:11:31
	24/06/2017	D12	52.0061 ; -14.9961	52.0034 ; -14.9902	1053 - 674	01:04:37
	25/06/2017	D15	51.7785 ; -15.0546	51.7820 ; -14.9288	1075 - 591	*07:33:00
	26/06/2017	D19	51.9758 ; -15.0474	51.9722 ; -15.0392	987 - 749	01:05:43
	26/06/2017	D20	51.9920 ; -15.0246	51.9861 ; -15.0174	992 - 716	00:58:24
	26/06/2017	D21	51.9965 ; -15.0092	51.9950 ; -15.0081	985 - 873	00:44:01
	27/06/2017	D21a	51.9951 ; -15.0067	51.9930 ; -15.0030	869 - 625	00:22:19
	27/06/2017	D22	52.0126 ; -14.9882	52.0096 ; -14.9799	1000 - 698	01:02:54
	27/06/2017	D23	52.0197 ; -14.9786	52.0194 ; -14.9787	1000 - 719	00:45:41
SeaRover 2018	15/07/2018	PB25	51.8014 ; -15.2187	51.8023 ; -15.1985	2533 - 2010	02:29:06
	15/07/2018	PB14	51.6408 ; -15.2812	51.6554 ; -15.2656	2839 - 2490	03:01:13
	18/07/2018	PB13	51.6949 ; -15.3159	51.7004 ; -15.3034	2786 - 2476	02:05:51
	19/07/2018	PB35	51.8614 ; -15.1204	51.8665 ; -15.1118	2000 - 1678	03:22:16
	19/07/2018	PB36	51.8621 ; -15.0303	51.8667 ; -15.0276	952 - 799	01:51:36
	19/07/2018	PB31	52.0333 ; -15.0000	52.0419 ; -14.9807	1722 - 1497	02:48:38
Supplementary Dives						
QuERCi I	20/06/2015	D07	52.0065 ; -14.9952	51.9826 ; -15.0290	1122 - 629	*03:02:48
QuERCi II	26/05/2016	D02	52.0055 ; -14.9939	52.0053 ; -14.9941	830 - 722	*01:00:00
	26/05/2016	D03	51.9901 ; -15.0459	52.9804 ; -15.0400	1200 - 900	*04:20:00
CoCoHaCa I	26/06/2017	D16	51.9428 ; -15.0764	51.9471 ; -15.0703	966 - 754	*00:54:37

*Table 2: Summary of ROV dives with observed bedrock exposure used for this study (*dives with poor navigation or discussion purposes only). D07 (QuERCi I) and D02 (QuERCi II) are proximal to D12 (CoCoHaCa I). D03 (QuERCi II) is located in deeper water, north of D19 (CoCoHaCa I).*

The ROV is fitted with an oblique forward-facing high-definition camera capable of recording at 1080i resolution, and a 5 MP digital stills camera. Two 400 W hydrargyrum medium-arc iodide (HMI) lamps are mainly used for lighting throughout the video transects, and two 24 V red lasers (spaced 10 cm apart) are used for scale. The high-definition video data is stored as a *.mov file. The original timecode for the video footage can be viewed using QuickTime Player, and this time was correlated to USBL positioning information for the ROV in order to accurately georeference areas and features of interest.

The video transects are concentrated along the southern flank of the PBC. Some of the transects are located along the canyon break, along the upper margin edge, and some in deeper waters (Figure 5; Table 2). The video dives had an approximate trajectory starting from the west in deeper water moving east to a shallower depth, travelling in an upslope direction. Each video transect was reviewed carefully for sections of exposed bedrock. Any areas with *in-situ* outcrop were noted and interpreted in order to identify the different rock types present in the study area. ROV video data was complimented by high-resolution digital still imagery, which was taken regularly along the video transects for features of interest. Occasionally, interpreting the outcrop is impeded by the presence of dense benthic communities, poor visibility along the transect line, metalliferous crusts and variable amounts of sediment cover over the bedrock. In these circumstances, efforts have been made to incorporate different video angles at a lower resolution in order to identify the different lithologies present.

ROV positioning data for sections of exposed bedrock were resampled using the Generate Points Along Lines tool in ESRI ArcMap 10.6, spacing points along the

transect line at 5 m intervals. This reduced potential oversampling bias for observation data relating to changes in ROV speed in seafloor of variable relief or prolonged positioning in larger cliff-like terrain.

2.3. Bedrock suitability mapping

A combination of the resampled observation data from ROV imagery and spatial analysis of the gridded bathymetry and backscatter data were used to identify suitable seafloor terrain in the PBC for outcrop to occur in. Raster grids (*.tif) of the processed MBES data (Figure 5 and 6) and resampled georeferenced outcrop observations (see Appendix B) were integrated into a geographic information system (GIS) for further spatial analysis based on bathymetric derivatives (referred from here on as terrain variables).

2.3.1. Terrain variables

A selection of quantitative terrain variables were derived from the original bathymetric data using tools in ESRI ArcMap 10.6 (Table 3). These variables were chosen based on their efficiency in delineating and representing rock outcrop on the seafloor, as identified by previous studies aiming to identify bedrock from bathymetry data (Bellec et al., 2017; Brown et al., 2017a; Elvenes et al., 2019; Joo et al., 2020; Misiuk et al., 2018). Each variable is calculated over an analysis window of 3 x 3 cells surrounding a central pixel, the size of which is defined by the raster resolution being used (in this case 25 m) (Wilson et al., 2007). The tools mentioned in the following are from the Spatial Analyst toolbox in ESRI ArcMap 10.6, unless otherwise stated. From all the

terrain variables, the Extract Multi Values to Points tool was used to extract attribute values for each terrain variable to the resampled positioning data.

Terrain Variable	Description	Method	Source(s)
Bathymetry Backscatter	Seafloor terrain (i.e. water depth in metres) Hardness or reflectance of seafloor based on composition	Original raster	(Brown et al., 2017b; Copeland et al., 2013; Guinan et al., 2009; Joo et al., 2020b; Neves et al., 2014)
Slope Aspect Mean Curvature	Change in water depth along steepest seafloor incline Orientation of seafloor at a given point Boundaries of distinct seafloor features	Slope tool Aspect tool Curvature tool and Focal Statistics tool	(Walbridge et al., 2018; Wilson et al., 2007)
Broad Scale BPI Fine Scale BPI	Seafloor position relative to the surrounding terrain (indication of crests and troughs in seascape)	*Benthic Terrain Modeller (BTM)	(Lundblad et al., 2006; Walbridge et al., 2018; Wright et al., 2005)
Roughness Rugosity	Indication of terrain heterogeneity, relative to variations in seabed morphology	Focal Statistics tool	(Lecours, 2017; Wilson et al., 2007)

*Table 3: Summary of terrain variables used for bedrock suitability mapping and their respective tools for derivation (*environmental classification tool).*

Slope is the change in elevation along the steepest incline on the seafloor (Wilson et al., 2007), and is inherently linked to the stability of seafloor sediments and to the local acceleration of currents, relating to erosion, sediment mobilisation, and seafloor bedform development (Dolan and Lucieer, 2014). *Curvature*, defined as the rate of change of slope (Walbridge et al., 2018), is useful in delimiting regions on the seafloor which are relatively distinct to one another, in terms of changes in benthic flow speed and direction (Walbridge et al., 2018). In this case, *mean curvature* has been used as it provides a good general summary of surface curvature in order to identify positive outcropping features on the seafloor (Wilson et al., 2007). Aspect is a measure of surface direction (Walbridge et al., 2018). *Bathymetric Position Index (BPI)* classifies seascape structures based on the change in slope position over two scales, which ensures that scale dependent phenomena are captured within the bathymetry

(Walbridge et al., 2018). BPI is calculated based on the difference between the focal point of a cell and the mean elevation of the surrounding cells within a user defined analysis window (Lundblad et al., 2006). BPI was calculated at broad scale, with an inner radius of 1 and outer radius of 10 (scale factor of 250), and fine scale, with an inner radius of 1 and outer radius of 4 (scale factor of 100) for hull-mounted bathymetry. *Rugosity* is a common descriptor of terrain heterogeneity in marine applications, with various modes of calculation (Walbridge et al., 2018). For this study, rugosity, or terrain 'complexity', was estimated via surface *roughness* as well as standard deviation of bathymetry, as it proved useful in identifying rock outcrop, and limited the encapsulation of carbonate mound features identified through similar methods. Roughness was derived by finding the difference between the maximum and minimum bathymetric values within the 3 x 3 rectangular window (Wilson et al., 2007). The standard deviation of the original bathymetry was also calculated as a form of rugosity (D. C. Dunn and Halpin, 2009; Grohmann et al., 2011; Lecours et al., 2016). Supplementary figures showing the terrain derivatives used during the bedrock suitability mapping prior to reclassification are presented in Section 3.4.

2.3.2. Spatial analysis

In order to identify suitable terrain in the study area for bedrock exposure to occur in, the Extract Multi Values to Points tool was used to extract attribute values for each terrain variable to the resampled observation points. 20% of these points were randomly excluded for an accuracy assessment of the final suitability model (see

Section 2.3.3). The remaining points were used to identify key attribute ranges for each terrain variable for where bedrock was observed along the ROV transects.

Four classes were identified for each terrain variable. These classes were based on the interquartile ranges (IQRs) of the extracted attribute values, which describe the statistical distribution of bedrock observations between the upper (75^{th} percentile) and lower (25^{th} percentile). The optimal range was chosen to be +/-10% of the IQR from the median, followed by the rest of the IQR, values outside of the IQR and the remaining unrecorded variable values. Using the Reclassify tool, each terrain variable were reclassified to these four classes, determining prime terrain characteristics for outcrop to occur in based on individual variables. Using the Raster Calculator tool, the reclassified variables were multiplied together, calculating pixels with high or low values depending on the accumulative output of suitable or unsuitable classes. These values were normalised in order to identify outcrop suitability based on a range from 0 - 100, described here as the *bedrock suitability index* (BSI).

2.3.3. Accuracy assessment

The 20% of the observation points that were excluded from the spatial analysis were used to test the accuracy of the BSI in the final map output. BSI values were extracted to these points. From this, points which were correctly or incorrectly classified as suitable for bedrock exposure to occur in were recorded. Similar to Copeland et al. (2013), Neves et al. (2014) and Joo et al. (2020), the accuracy was then calculated by the percentage of correctly classified observation points from the assessment dataset.

2.4. Photogrammetry

Sections of interest were identified along each video transect in order to make detailed 3D models of rock outcrop. Suitable sections for modelling were chosen based on the visibility at the seafloor, a consistent ROV speed throughout the video recording and no visible obstructions or physical disruptions which would hinder the ROV during the data collection (e.g. submarine cables, ghost nets and challenging terrain), ensuring that the area of interest remained clearly visible at high-resolution throughout area of interest.

For an outcrop of interest, the video timestamp was noted for the start and end point of that section along the transect line where exposure occurs. Using this time interval, individual frames could then be extracted from the original video footage. This was completed using FFMPEG 4.3, an open source software run through the command line (available at www.ffmpeg.org/download), using the following string of text:

```
ffmpeg -ss 00:00:00 -to 00:00:00 -i IN_Dive_X.mov -r 5
OUT_%03d.png
```

Where:

-ss	indicates the starting time of the video section
-to	indicates the ending time of the video section
-i	locates the input video file for the ROV dive
-r	determines the number of frames per second (fps) to be extracted
%03d	will write frame names with 3 successive digits
.png	indicates that each frame will be stored as a *.png image file

Frames were extracted within a working folder on a hard drive where the original video footage was stored. Frames (48 bit depth HD) were extracted at 5 fps, ensuring sufficient overlap and quality in the imagery dataset. This worked consistently across

different transects from different surveys, where ROV speed may differ slightly, based on site terrain and surveying conditions. Once extracted, frames were restored locally for further 3D modelling.

The photogrammetry was worked on using Agisoft Metashape 1.5.1, a standalone software, successor to the widely used Agisoft PhotoScan. The modelling procedure was conducted as follows (Figure 7):

- An initial project file was saved in the folder containing the imagery being worked on. Imagery was then imported and image quality was estimated. Image quality between $0.7 \leq 1+$ was deemed suitable for modelling. Images with < 0.7 image quality are often dark, distorted or may have momentarily encountered poor visibility (e.g. ROV collision, propulsion and sediment suspension). Images of poor quality were rarely encountered through the extraction process, as sections along the transect chosen for modelling were of suitable criteria (see above).
- Following the project set up, imagery was aligned (high to highest accuracy) in order to identify approximate image positions and build a sparse point cloud (composed of tie points). During this step, if imagery was not correctly aligned, the process was repeated, building on the initial alignment, ensuring all imagery was being used where possible.
- Once imagery was aligned, key frames along the transect where georeferenced by importing a *.csv containing the frame number and its positioning (coordinates and depth), based on the ROV's USBL positioning. All

coordinates being used in the referencing and modelling process (including camera and marker references) were in UTM 28 North.

- Reference markers were placed manually in the imagery data on clearly identifiable features (e.g. the corner of a fracture, sessile marine life and material on the seafloor). Each model contains multiple markers that were georeferenced based on the available USBL data, and scaled based on the red lasers (spaced 10 cm apart) used by the ROV during surveying. This positioned each model into its correct orientation and ensured that the model surface would be true to scale.
- Once the initial sparse point cloud was correctly referenced, a dense point cloud was generated. These points were further used to create a mesh and DEM for each model. The final step in creating the 3D model involved generating a surface and texture for the mesh previously mentioned, which creates the final appearance of the 3D surface based on colours from the input imagery. An orthomosaic was also generated for each of the modelled sections.

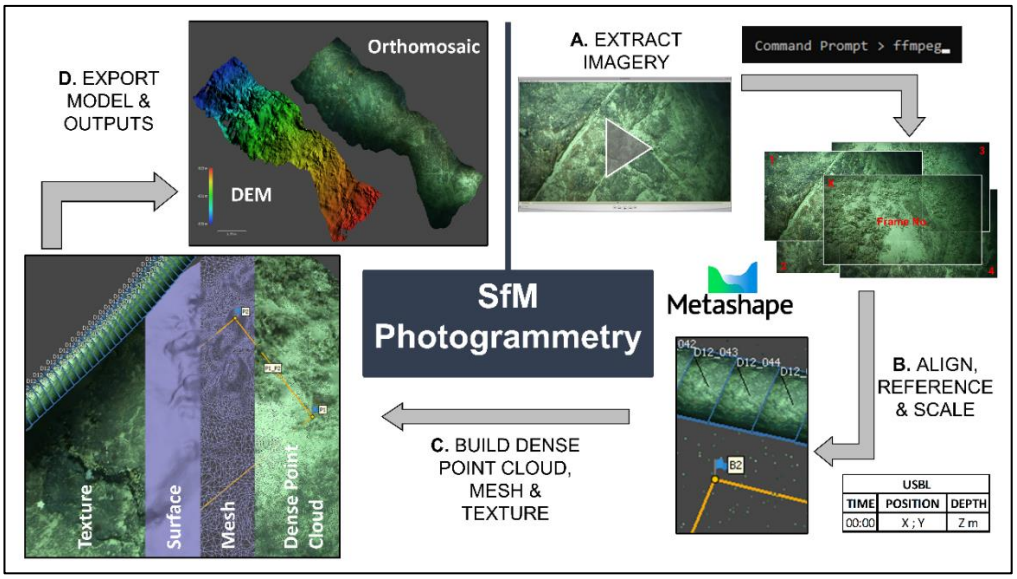


Figure 7: Summary of workflow used for SfM photogrammetric modelling of offshore outcrop.

2.5. ROV rock sampling

Two rock samples were acquired from the PBC during the CoCoHaCa I research survey on board ILV Granuaile (Wheeler and Shipboard Party, 2017). This was facilitated by means of a hydraulic rock drill mounted to the retractable tool sled of the Holland 1 ROV (Figure 8). Sampling was possible when the ROV could land safely facing a rock face.

Drilling was conducted by extending the ROV's tool sled forward, ensuring no vibrations or movement of the ROV and a safe collection of sample. The barrel of the rockdrill has a diameter of 40 mm. The procedure was monitored through the live video feed, and took approximately 25 minutes at each location.



Figure 8: Hydraulic rockdrill mounted to the tool sled at the front of the Holland 1 ROV (A), and rockdrill sampling in action (B) on the seafloor (D26, approx. -1132 m).

2.6. Sample analysis

A standard petrographic thin section was made for each of the two rock samples (Figure 9). Further Raman mapping and analysis was carried out on the polished surfaces of the rock samples themselves. Petrographic images obtained using Huawei P30 Pro (mounted to eye lens of petrographic microscope).



Figure 9: Rock samples (R1 and R2) bagged and thin sections for each.

2.6.1. Raman spectroscopy

Raman data were acquired using an inVia Qontor confocal spectrometer by Renishaw. A 50 mW DPSS laser at 532 nm wavelength was focused through a research grade Leica microscope with a 50x objective in order to acquire Raman spectra. A diffraction grating of 1800 lines/mm was set for light dispersion. Raman signal were analysed using a Centrus CCD detector (1040 x 256 pixels) by Renishaw. An area was picked on each of the thin sections for each sample for analysis (Figure 10).

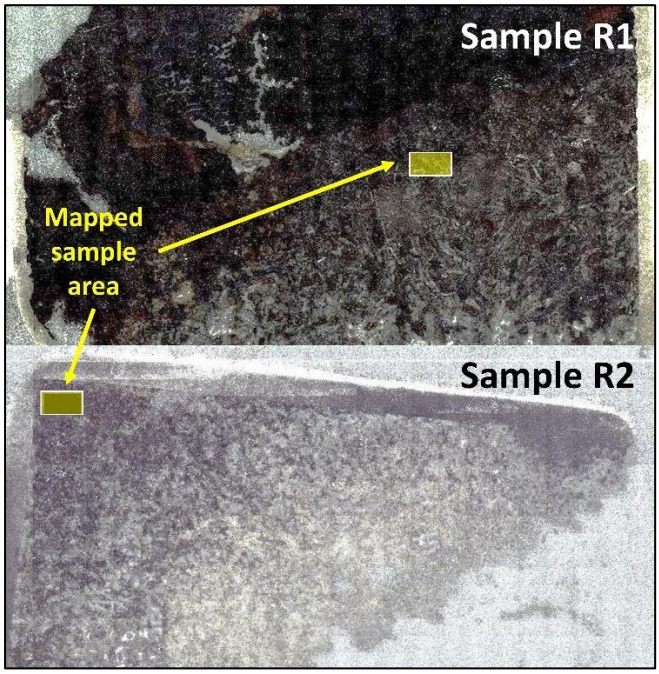


Figure 10: Image of thin section surface, with approximate area for each thin section for which Raman mapping was conducted.

A fragment of Sample R1 has been cut, polished and resin mounted for further analysis. The polished surface was reanalysed using the Raman instrumentation described above, in order to identify any apatite grains present in the sample (Figure 11). Each grain identified has been given a coordinate relative to the sample itself, and can further be used for dating methods (via LA-ICPMS). This grain notation process was carried out using high-resolution imagery of the sample surface and its Raman data in ESRI ArcMap 10.6. Due to unforeseen circumstances, the planned dating analysis for this study could not be completed on the rock sample material before the completion of this thesis.

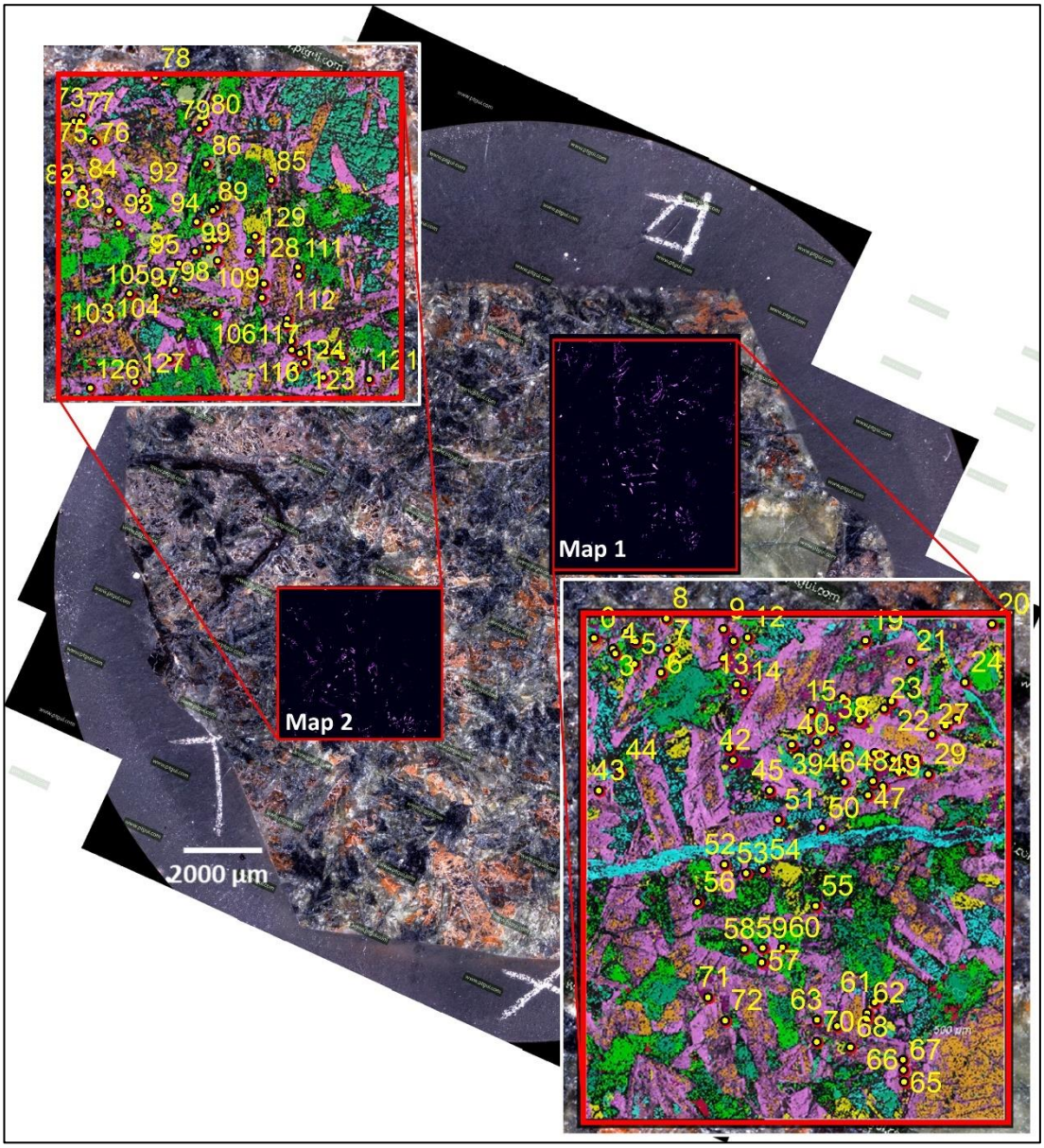


Figure 11: High resolution image mosaic of sample R1 fragment with apatite data plotted, ready prepared for further dating analysis (which could not be completed). Numbering describes individual apatite grains (mapped) in the sample fragment.

3. Results

3.1. Bathymetry and backscatter

The MBES data covered an area of 2055 km^2 in the PBC. A moderate to steeply sloping margin divides the study area, separating a shallower upper canyon head and break in the east (minimum depth recorded -434 m) from the deeper abyssal plain in the west (maximum depth recorded -3361 m). The study area can be separated into three subzones (Figure 12). These zones have been identified based on differences in general seabed morphological features and changes in local relief.

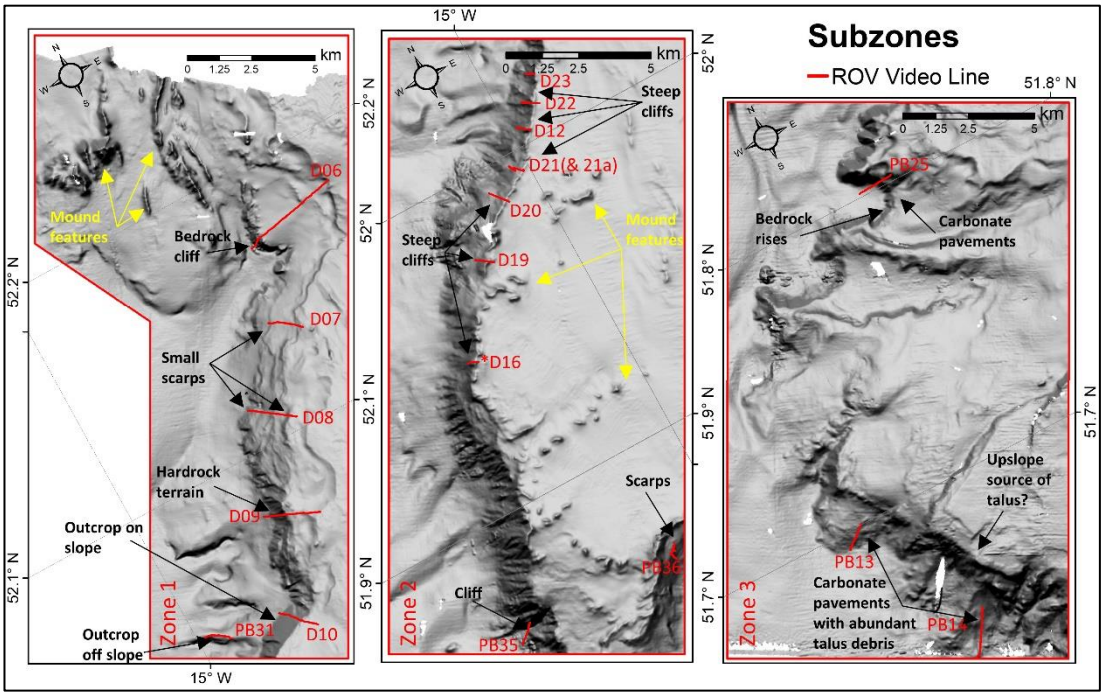


Figure 12: Slope gradient maps (shaded) used to visualise and describe features present across subzones in the study area (Zone 1 – left. Zone 2 – middle, Zone 3- right, as outlined in Figure 5).

Zone 1 comprises the canyon head and the north-eastern flank of the canyon (Figure 12). Linear aggregations of CWC mound structures (aligned N-S) are situated to the north on a moderately sloping seafloor. The upper canyon slope gradually deepens in Zone 1, and passes over small vertical rises and escarpments sections which steepen

sharply, expose broken hardgrounds, breaking a gradually sloping seafloor. These scarps trend NNE-SSW for approximately 10 km, terminating to the south where the canyon flank 'kinks', and the trend of the canyon's edge shifts to NE-SW. Smaller slope incising channels are located off the canyon flank to the west. Backscatter values are noticeably higher along the escarpment features in Zone 1, distinguishing them from the surrounding seafloor which has lower reflectance (Figure 6).

Zone 2 is concentrated along the eastern canyon flank, where beyond the canyon edge, the seabed is significantly steeper in comparison to the previously described north-eastern flank (Figure 12). At the canyon edge, small mound features are apparent (aligned E-W), and the slope steepens abruptly beyond a narrow 'lip' or ridge, which extends the length of this subzone. East of Zone 2, similarly NNE-SSW trending escarpment features are present. Incising channels are present at the base of the slope, however, these are smaller than in the north. High backscatter values persist across the steeply sloping terrain in Zone 2 (Figure 6), which is distinguishable from the shallower flat-lying upper canyon area.

South of Zone 2, to the east, coral mound features are evident (Figure 12), which have previously been recognised by Lim et al. (2020) and Mazzini et al. (2012). A large escarpment, that trends N-S and is broken in parts, is situated east of these mounds (Figure 6).

Zone 3 is situated in the south of the study area (Figure 12). Overall, greater relative depths prevail in this part of the canyon. A number of smaller canyons branch out into the main channel of the PBC. At this transition, a 'step-like' terraced seafloor is

present with steeply sloping terrains that appear normal to one another. Backscatter is generally higher along these high-relief features (Figure 6).

3.2. ROV video

From the ROV dive footage, seven different in-situ bedrock lithologies have been identified in the study area, with some igneous intrusions in parts. The following were observed:

- *Rock type A* - This lithology is generally observed with a very dark black surface (Figure 13(1)). One of the rockdrill plugs has been sampled from this lithology and has been identified as metamorphosed dolerite (R2 - *metabasite*; see Section 3.6). At shallower parts of the slope, this rock is seen with perpendicular fracture sets (e.g. D09), but these are less evident in deeper areas of the canyon (e.g. PB35). It is also found in deeper transects to the south, with clean vertical fractures (e.g. PB25).
- *Rock type B* - This is the most abundant lithology recorded in the study area, primarily exposed along the steeply sloping centre margin (e.g. D12). This lithology is generally seen proximal to rock type A, with a similar surface texture and colour, although in contrast, foliations are clearly defined (e.g. D16). These range in thickness of a couple of cm. Occasionally, along cliff sections, this rock type has a striated surface, with faulting observed cross cutting the laminations (Figure 13(2)). This rock type has also been sampled by the rockdrill, and the plug has been identified as a metamorphosed gabbro (R1 - *metagabbro*; see Section 3.6).

- *Rock type C* - This lithology was observed exposed along moderate to steeply sloping seafloor, with talus occasionally accumulating in some areas (Figure 13(3)). The surface is dark black to grey throughout, and thin black bands separated by slightly thicker lighter coloured laminae are distinctive of this lithology. This could be described as gneissic in texture, although confirmation of this is restricted by the nature of the video observations. Sections of outcrop are predominately broken and fractured (e.g. D19).
- *Rock type D* - This lithology has been identified as conglomerate composed of rounded pebble to cobble sized clasts. Sections with larger clasts appear to be clast supported, whereas smaller pebbly sections appear to be matrix supported (Figure 13(4)). Although a direct contact is unclear, talus of rock type A and C have been observed in the vicinity of this rock type.
- *Rock type E* - This lithology was observed in the southernmost transect line. It is seen in contact with the surface of rock type F with yellow to reddish brown stains surrounding the contact area. The structureless outcrop is composed of broken sub-rounded clasts, black in colour, within a light beige matrix (Figure 13(5)). In some areas, dark yellow staining was recorded across the surface of the bedrock.
- *Rock type F* - This lithology is exposed in deeper areas of the slope. It differs to the previously described rock types in that it is light beige in colour, with extensive amounts of borings in some areas, and evidence of spalling surfaces (Figure 13(6)). This rock type has been identified as carbonate material, with very thin black weathered crusts on broken surfaces. Along PB13, this rock type is predominantly covered by more recent sediment, obscuring its exposure in comparison to sections

in PB25, PB13 and PB14, where bedded sequences have been identified in the video transects, which are seen to overlie rock type A.

- *Rock type G* - This lithology was only observed at the end of transect PB13, overlying the previously described carbonate rock type. It is grey in colour with fresh blue broken surfaces. This bedded sequence has been recorded over a small rise of ~2 m, beds varying from 10 to 50 cm in thickness (Figure 13(7)). The beds appear to be laterally continuous, shallowly dipping NE, striking approximately NW-SE, based on ROV position and trajectory.
- Intrusive material - In different parts of the canyon, intrusive material has been observed amongst the different rock types, which noticeably differ from the surrounding bulk lithology. A dyke has been recorded intruding into rock type B (Figure 13(8-9)) which has a more rounded appearance, trending approximately NE-SW based on ROV positioning and trajectory. Collapsed lava tubes have been observed proximal to rock type E (Figure 13(9)).

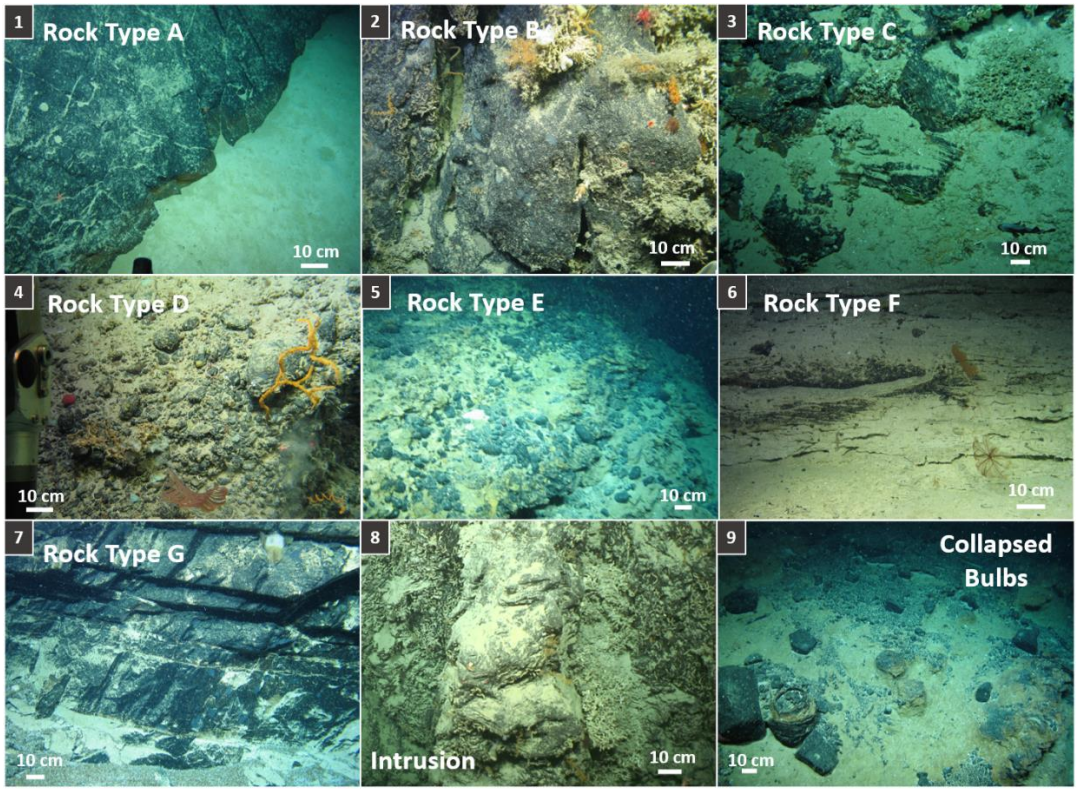


Figure 13: Rock types identified in the PBC based on ROV video footage.

Transects passing over shallower upslope area (east of the canyon edge) show an abundant amount of ice-rafted debris (IRD) scattered across the seafloor (Figure 14). Rippled sediment is occasionally observed close to large CWC structures (mounds and reefs), with coral rubble accumulating in the vicinity of these. Large scarps of carbonate material have also been observed (e.g. D08 and PB36), with surfaces having variable degrees of weathering. Deeper transects show evidence of large accumulations of broken rock, made up of dark pebble to cobble sized clasts, and slabs in parts (e.g. PB25, PB13 and PB14).

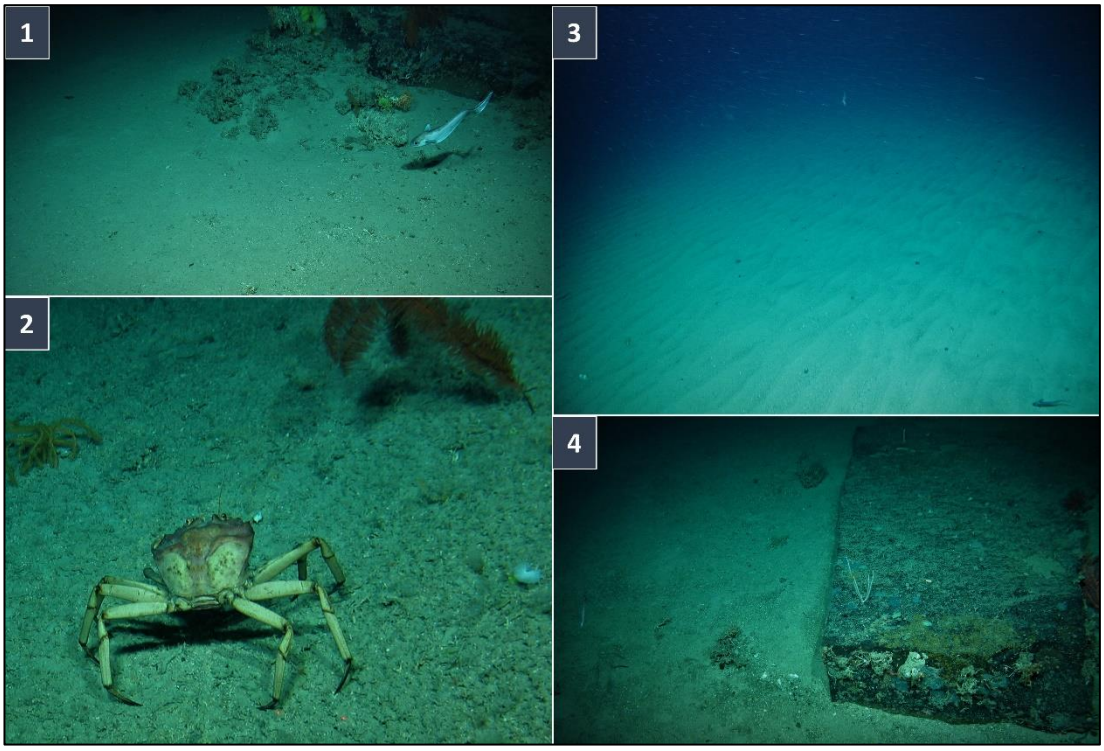


Figure 14: Footage from the shallower upslope area of the PBC, with IRD encountered on a predominantly sandy and gently sloping seabed (Wheeler and Shipboard Party, 2017).

3.3. Rock type distribution

The only video transect outside of the subzones previously described (Section 3.1) is D15 (Fig.1), which passes over carbonate mound structures and hardgrounds towards the end of the transect. The rest of the video data is spread out across each of the three subzones (Figure 6 and 12).

In *Zone 1*, a large, exposed section of rock type B is observed at the canyon head (D06, -1048 to 1029 m), with broken hardgrounds to the east. Smaller escarpment features are crossed south of this cliff (D07, -1020 m, -780 m and -745 m; D08, -1160 m, -893 m and -725 m), where the seafloor momentarily rises sharply along the moderately sloping seabed, exposing broken hardgrounds. South of these linear features, a large area of rock type A is encountered (D09, -810 m to -725 m). The outcropping terrain

here is not as steep as at the canyon head, and appears to be more broken and fractured. Sections of bedrock exposure outcrop sharply from the seabed here, and a small area of broken hardgrounds are also recorded in the east. Where the canyon kinks, rock type A is recorded along a moderately sloping seabed (D10, -1046 m to -740 m). Approaching the canyon flank (D10), a section of carbonate hardground separates the underlying bedrock from a lateral surface of broken and brecciated bedrock. Off the slope, rock type F is recorded (PB31, -1725 m to -1675 m).

In *Zone 2*, extensive cliff sections are more prevalent than in the north. Rock type A and rock type B are the dominant lithologies encountered along these steep rises. In parts, rock type A appears to have a significant crust on its surface (D23, -850 m to -757 m; D22, -879 m to 823 m), and appears to be significantly broken up towards the peaks of rising sections (D23, -780 m) close to the canyon break. Rock type B is similarly broken in the shallower parts of the canyon flank (D12, -779 m; D19, -833 m), as well as by large sub-vertical faults (D16). A possible sill is seen intruding through rock type A (D23, -987 m). In deeper parts of the slope (PB35, -1827 m to -1717 m), rock type A is recorded, with the degree to which the outcrop is deformed and broken up increases progressively upslope. Rock type C is generally seen across shorter sections (D19, -845 m; D16). Rock type D is recorded in a deeper area off the steeply sloping canyon flank (D03), and in shallower parts of the canyon flank, with a thin broken crust on its surface (D21 and D21a, -905 m to -849 m). In an isolated transect (PB36, -867 m), small linear scarps are recorded on a steeply sloping seabed, exposing broken hardgrounds (-846 m).

In *Zone 3*, the deepest coverage of the study area, a large section of rock type B is recorded along a small sloping section at the base of a feeder channel (PB25, -2391 m to -2227 m). Above this, the seafloor is composed of heavily broken material, possibly talus fallen down from a shallower area. Beyond this, a pavement section composed of rock type F is recorded (PB25, -2109 m and -2039 m). A significant amount of rock type F is also recorded further south (PB13, -2608 m to -2505 m; PB14). Above rock type F, rock type G is recorded, transitioning from a moderately sloping seafloor to a sharp rise of bedrock exposure, progressing onto shallowly dipping beds (PB13; -2659 m to -2521 m). Besides continuous sections of outcrop, large areas of the seafloor in this part of the canyon are densely covered in broken cobbles and blocks of two distinct lithologies (rock type F, and the other possibly being rock type A or B). Rock type E occurs in the southernmost transect line (PB14; -2658 m to -2521 m).

3.4. Suitability modelling

Each terrain variable yielded appropriate class ranges based on their IQRs in order to identify suitable terrain for bedrock exposure in the study area (Figure 15). Slope (31° median), roughness and rugosity (37 and 12 median, respectively) were amongst the most representative reclassified variables, whereas mean curvature (0.06 median) and BPI (5 broad scale median and 2 fine scale median) are slightly broader in terms of detail when classifying the study area for outcrop.

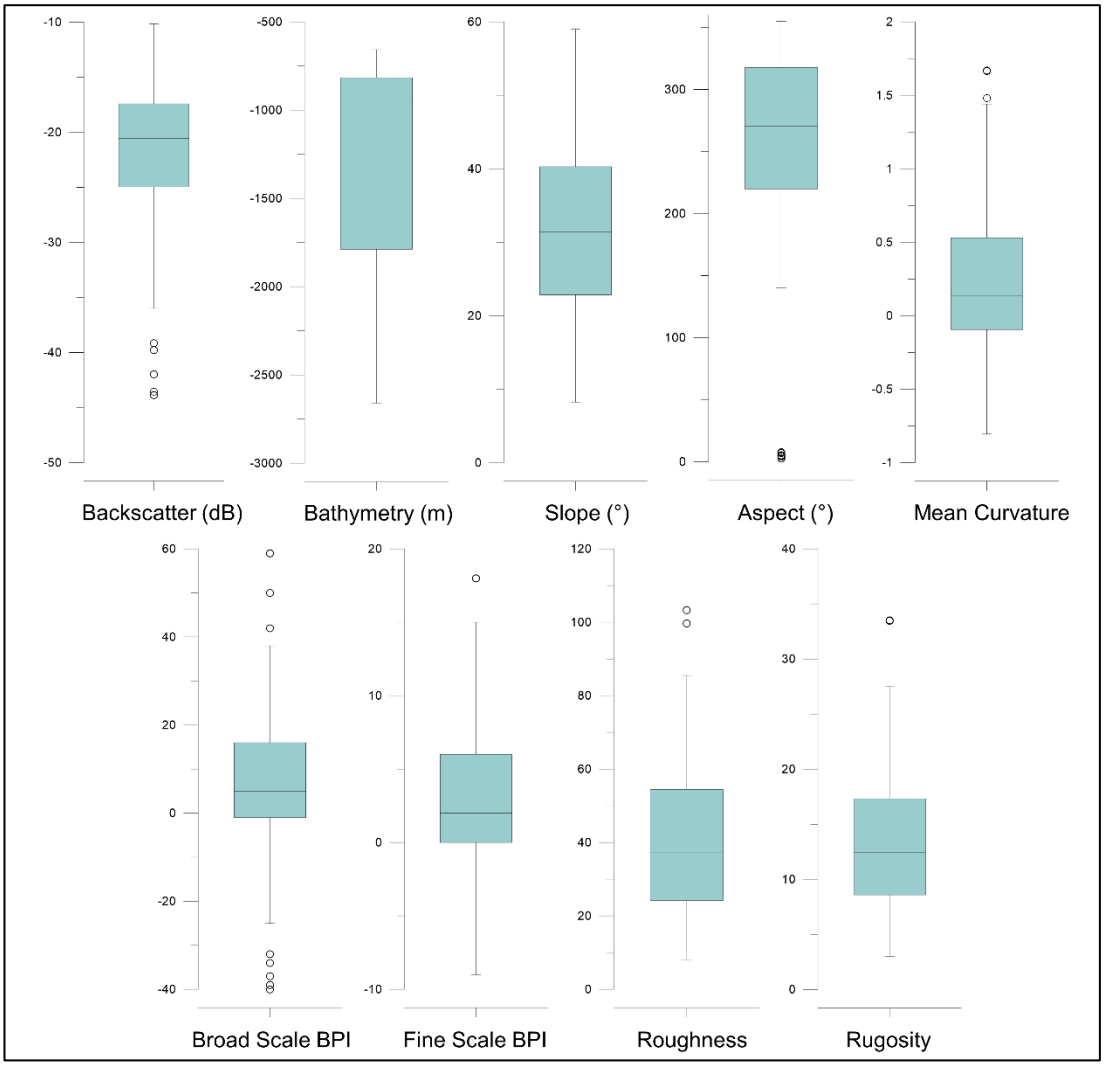


Figure 15: Box whisker plots showing the minimum, maximum, 1st quartile, 3rd quartile, median values and outliers (circles) for each of the quantitative terrain variables.

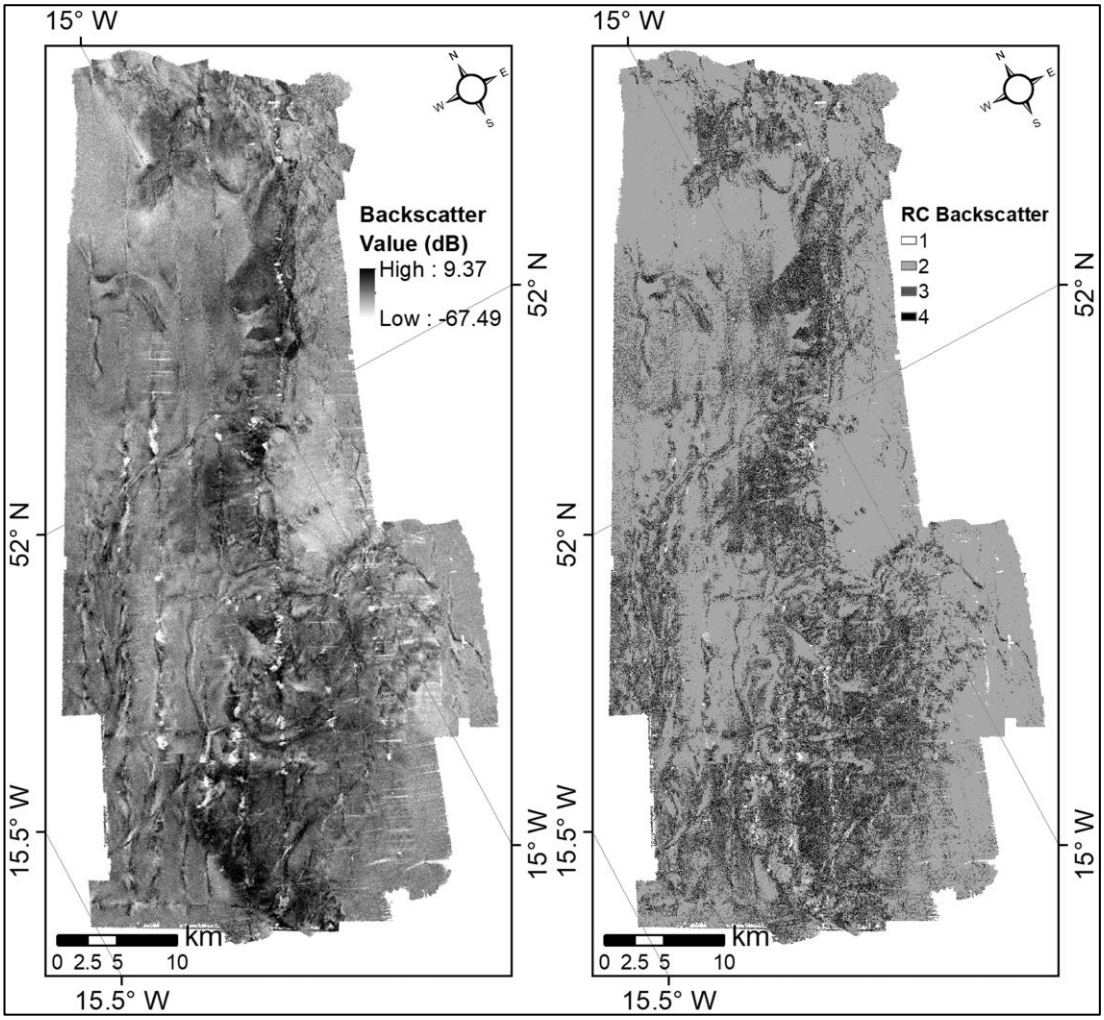


Figure 16: Backscatter data (left) with reclassified backscatter (right) based on IQRs for bedrock observations in the study area (Figure 15).

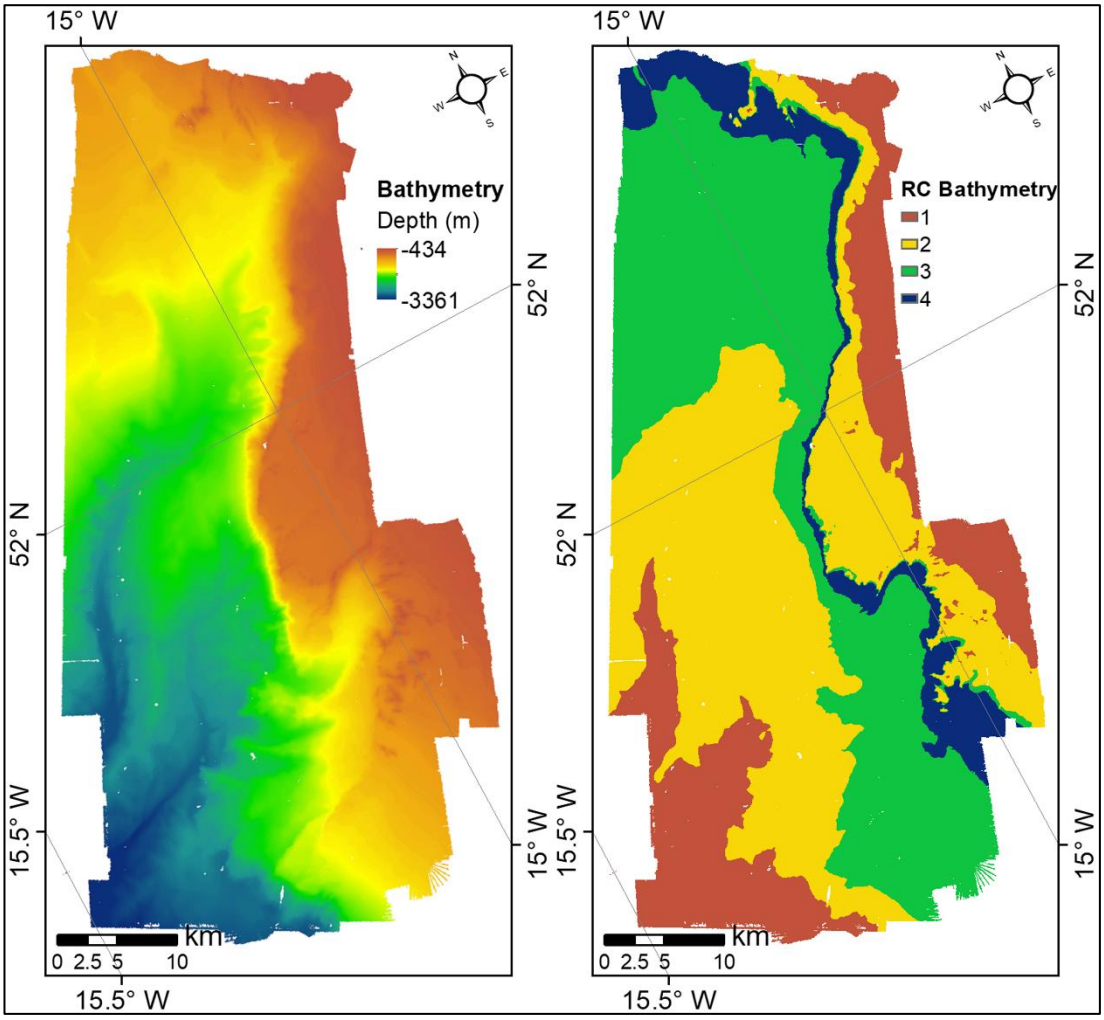


Figure 17: Bathymetry data (left) with reclassified bathymetry (right) based on IQRs for bedrock observations in the study area (Figure 15).

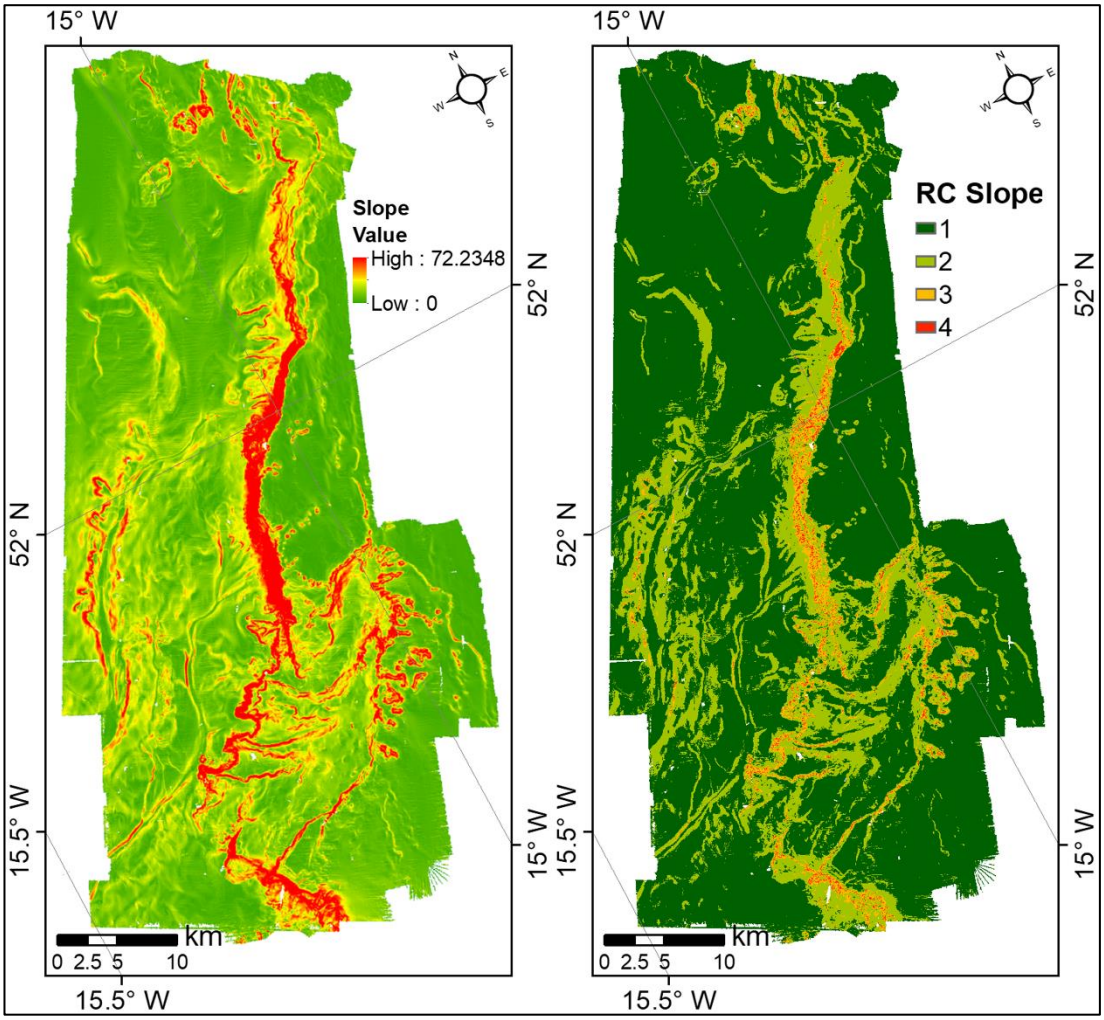


Figure 18: Derived slope layer (left) with reclassified slope (right) based on IQRs for bedrock observations in the study area (Figure 15).

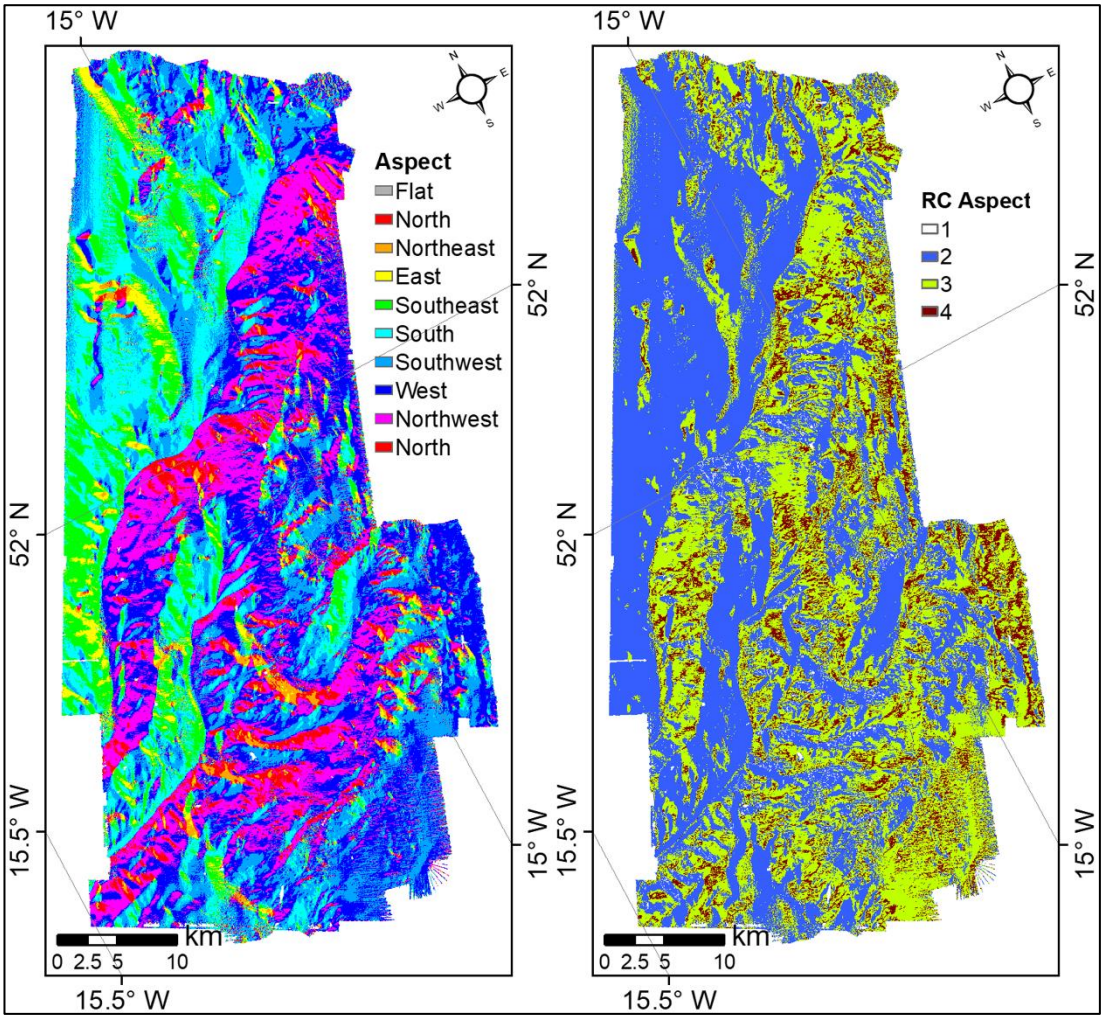


Figure 19: Derived aspect layer (left) with reclassified aspect (right) based on IQRs for bedrock observations in the study area (Figure 15).

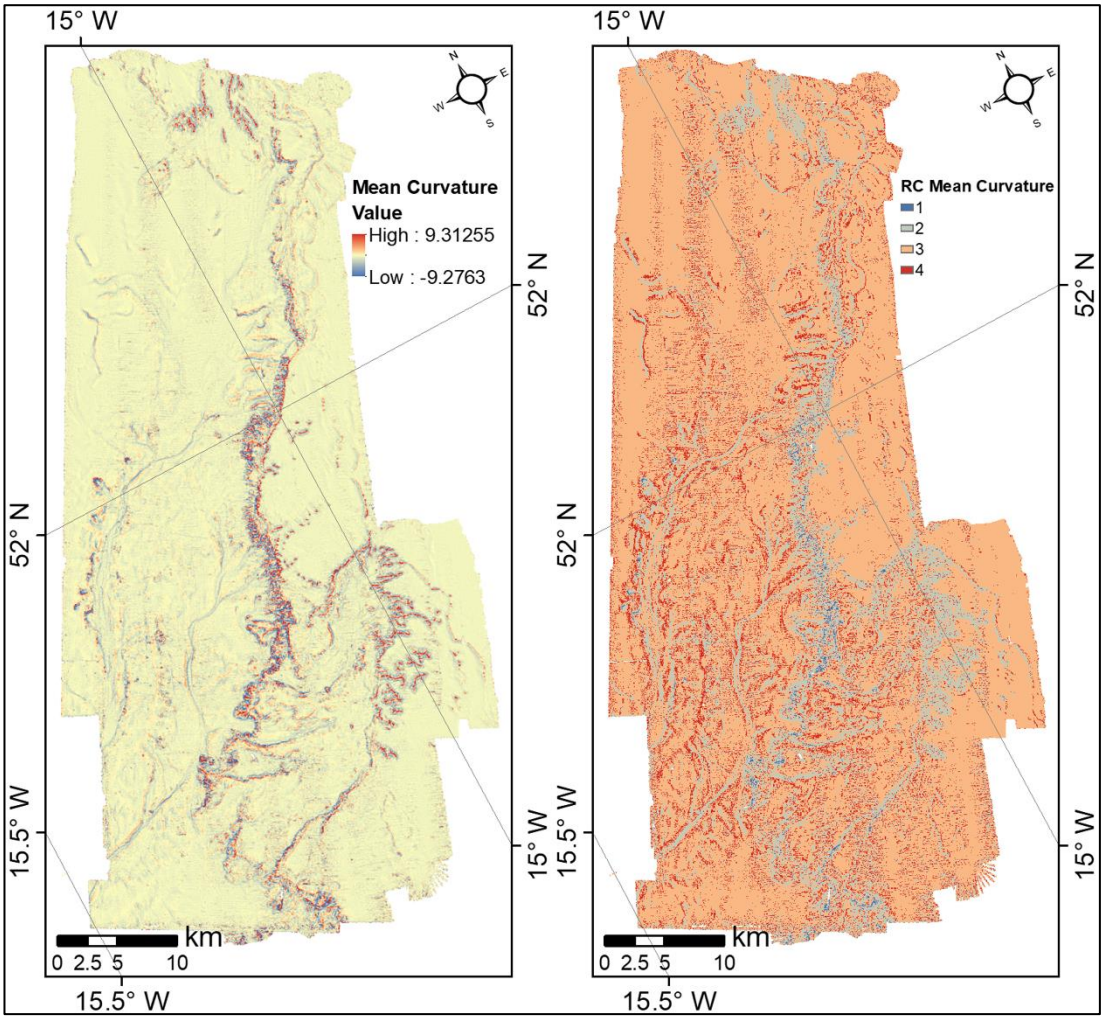


Figure 20: Derived curvature (mean) layer (left) with reclassified mean curvature (right) based on IQRs for bedrock observations in the study area (Figure 15).

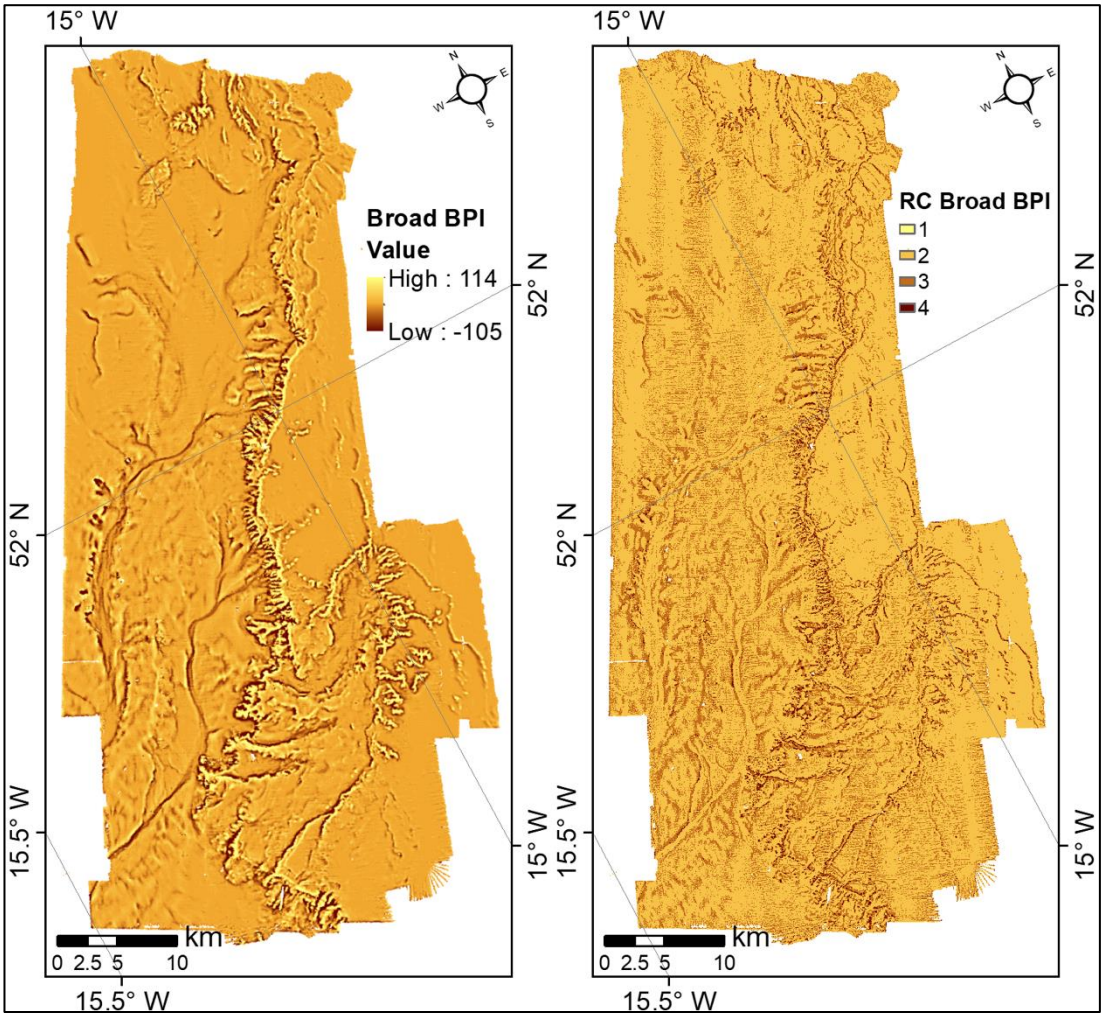


Figure 21: Derived broad scale BPI layer (left) with reclassified broad scale BPI (right) based on IQRs for bedrock observations in the study area (Figure 15).

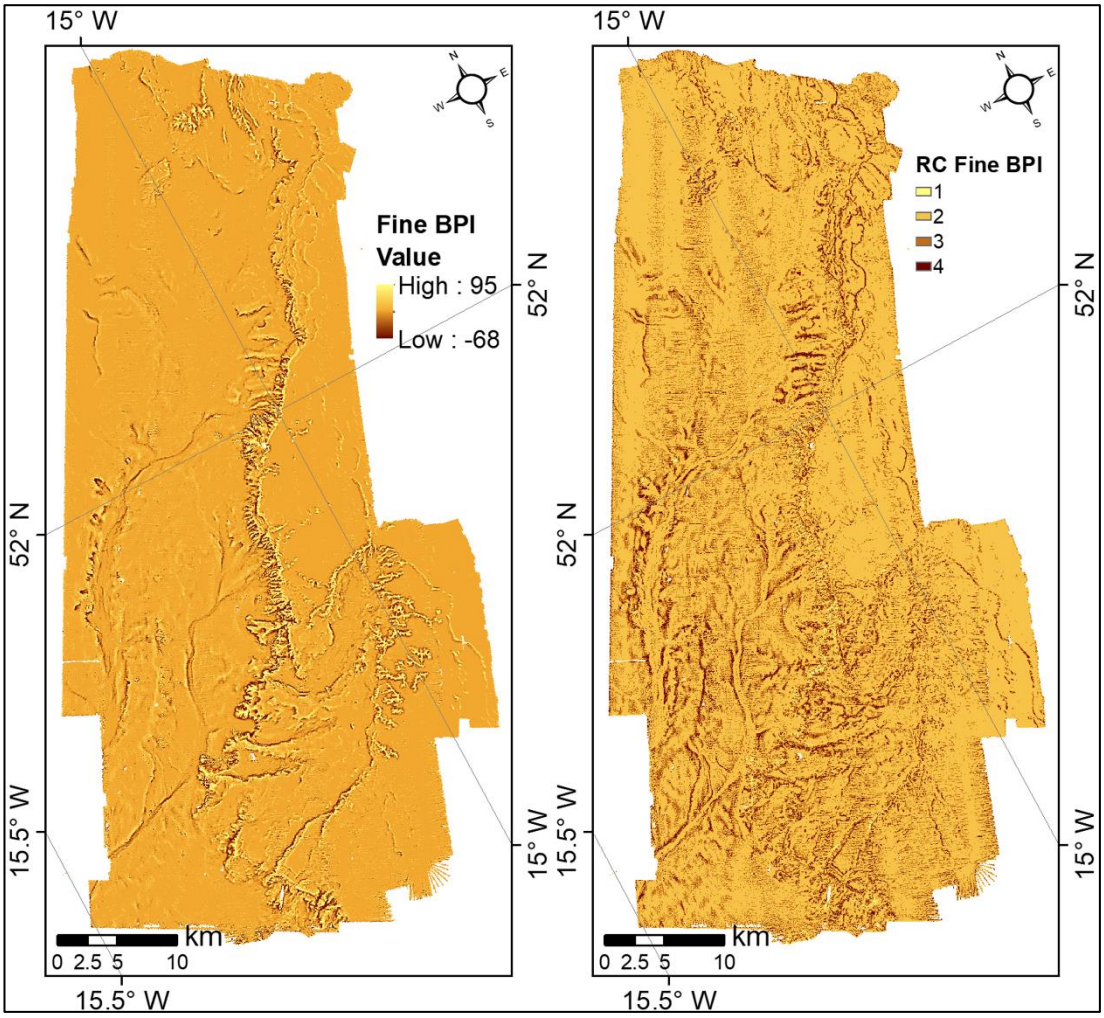


Figure 22: Derived fine scale BPI layer (left) with reclassified fine scale BPI (right) based on IQRs for bedrock observations in the study area (Figure 15).

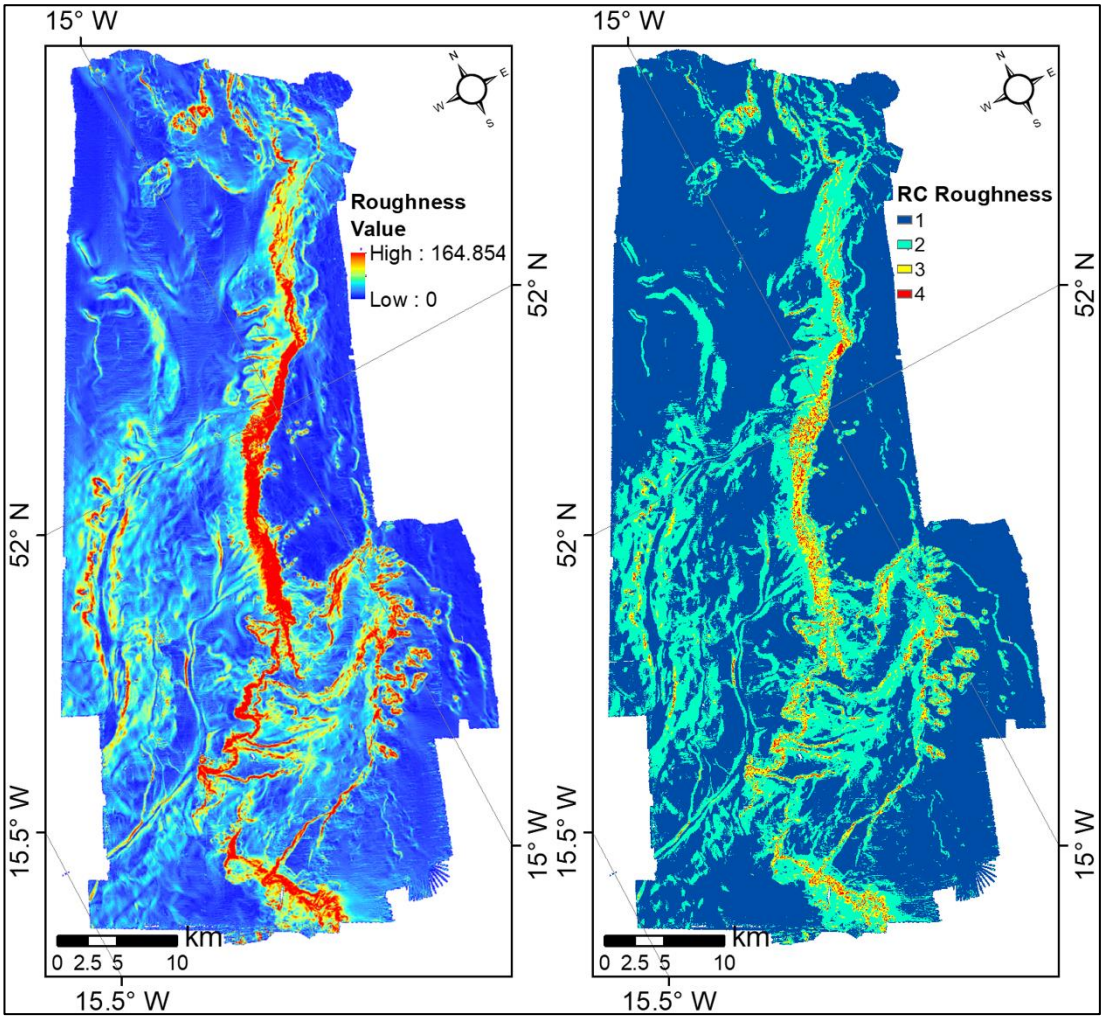


Figure 23: Derived roughness layer (left), determined by the difference between the maximum and the minimum cell height with a 3 x 3 neighbourhood. with reclassified roughness (right) based on IQRs for bedrock observations in the study area (Figure 15).

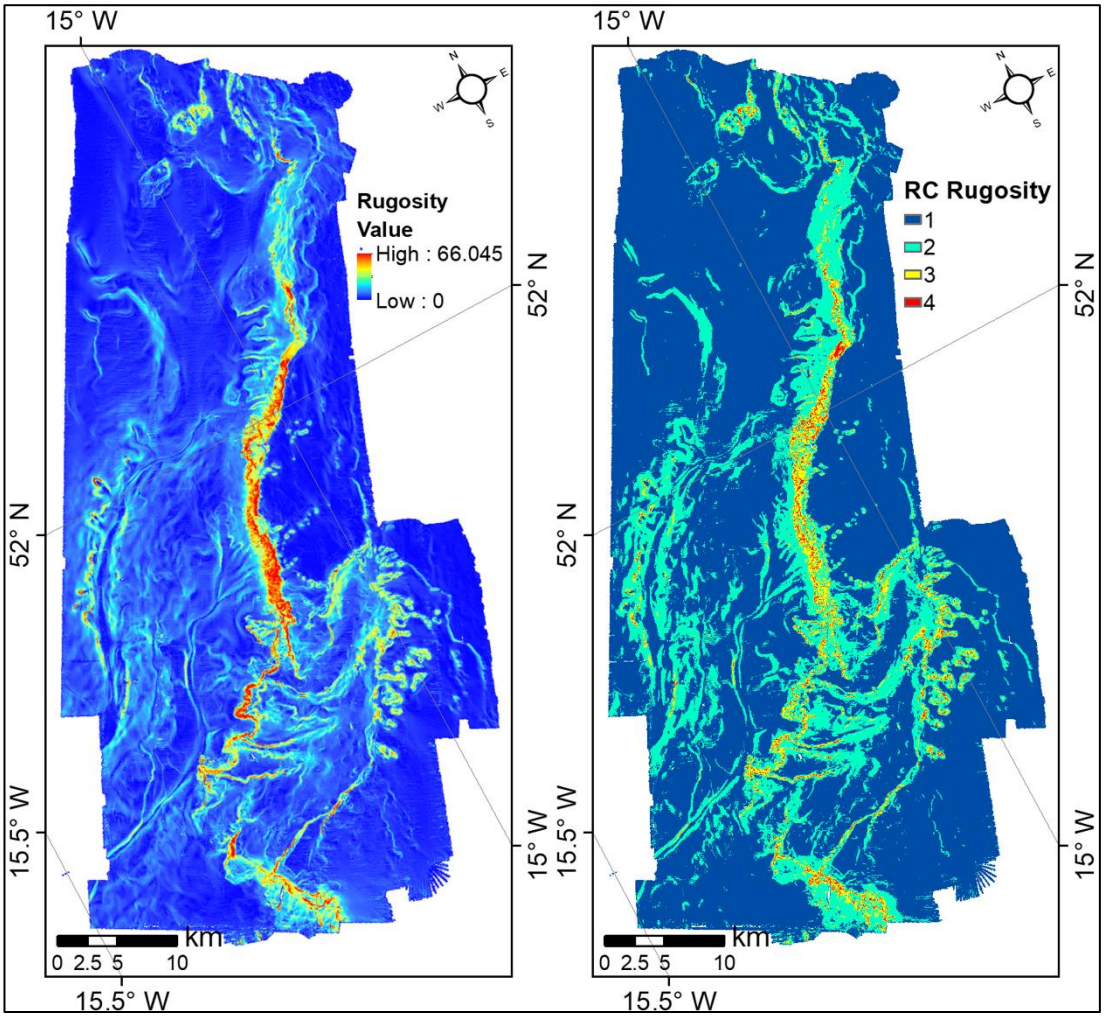


Figure 24: Derived rugosity layer (left) a separate measure of seafloor roughness based on the standard deviation of bathymetry, with reclassified rugosity (right) based on IQRs for bedrock observations in the study area (Figure 15).

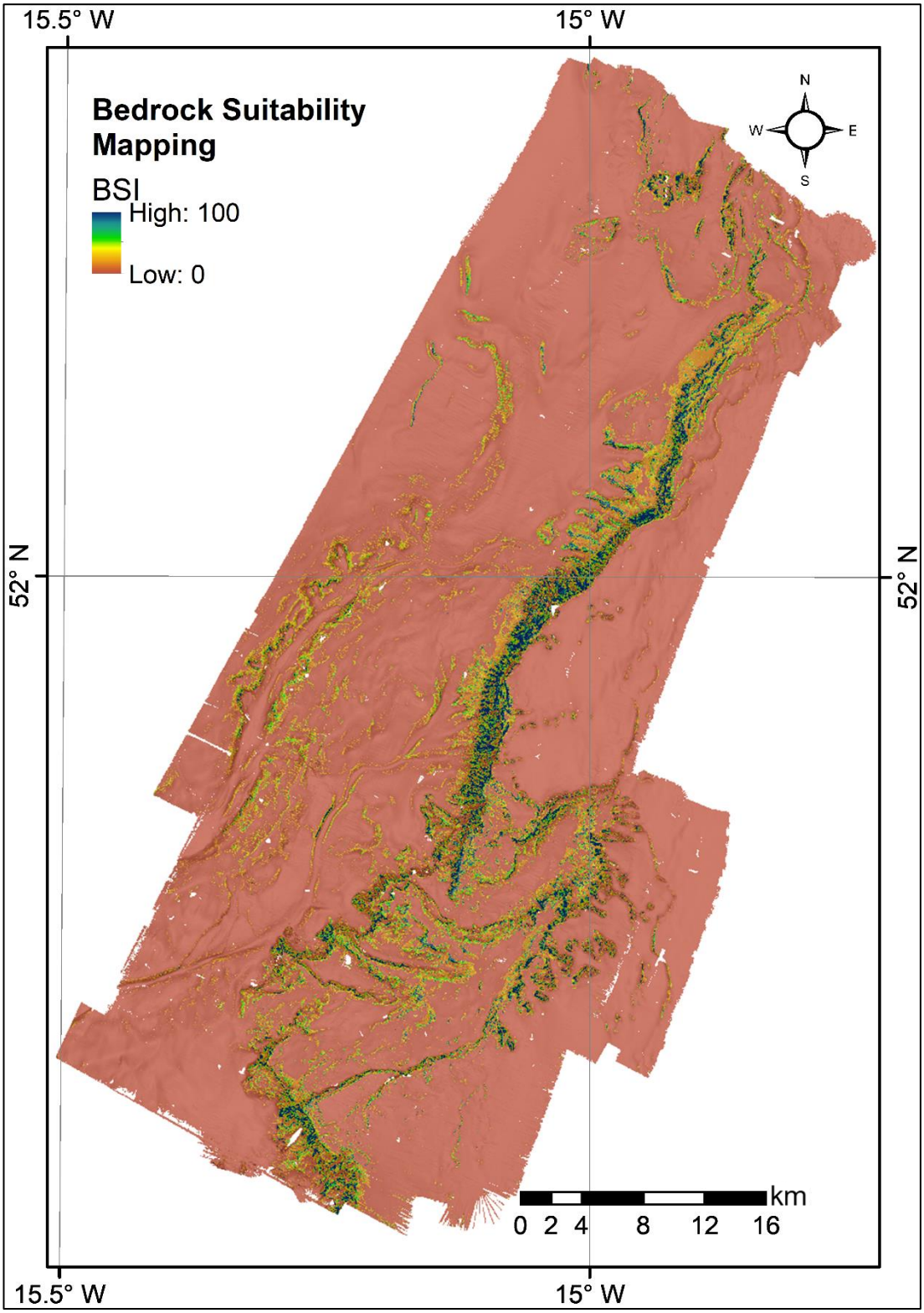


Figure 25: Map of PBC study area showing final output of normalised BSI results, where 0 (unlikely) and 100 (likely) represent terrain suitable for outcrop exposure to occur in.

A total of 60% of the bedrock observations which were randomly excluded for the accuracy assessment were correctly classified using the method outlined above.

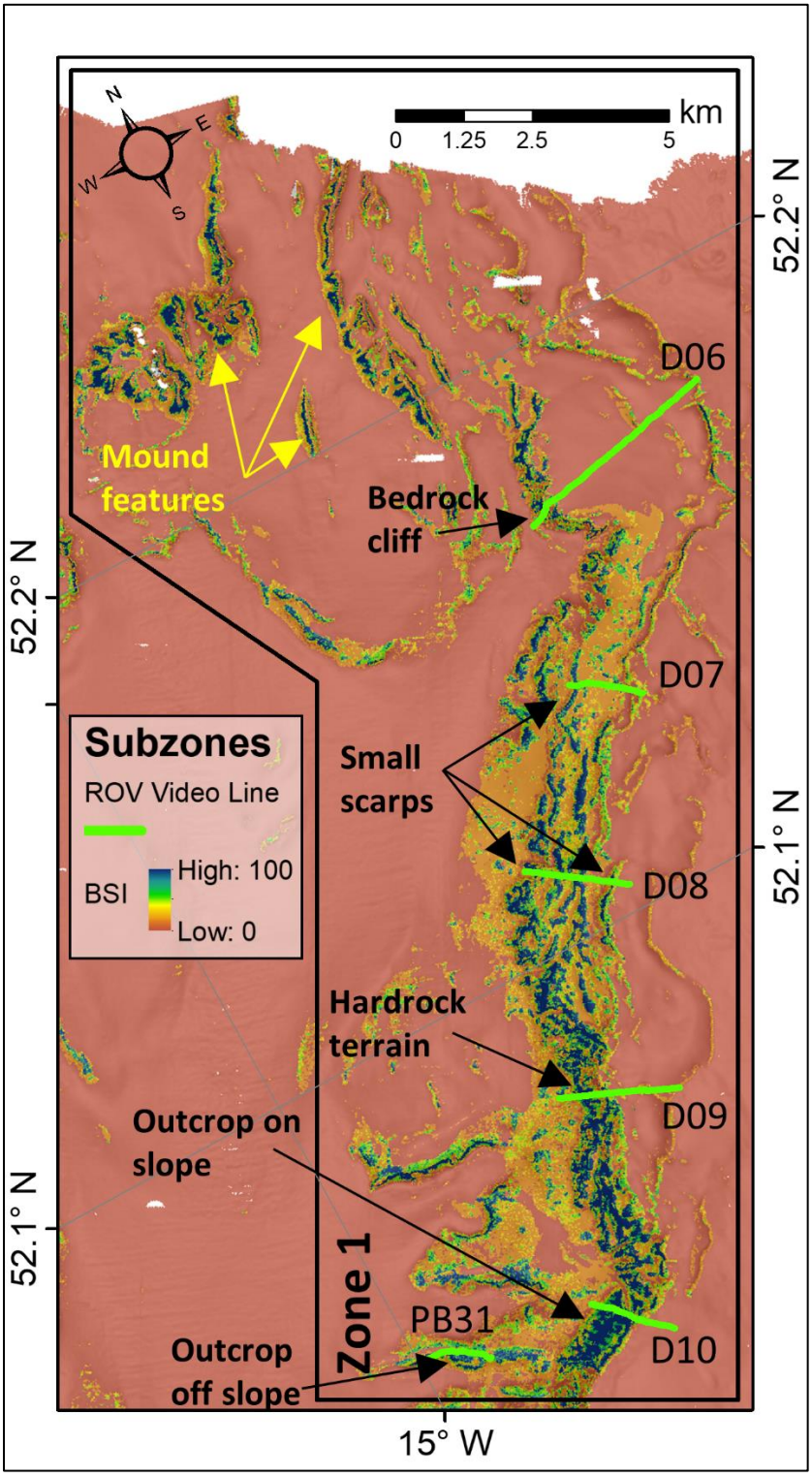


Figure 26: BSI results plotted over terrain in Zone 1, with features labelled.

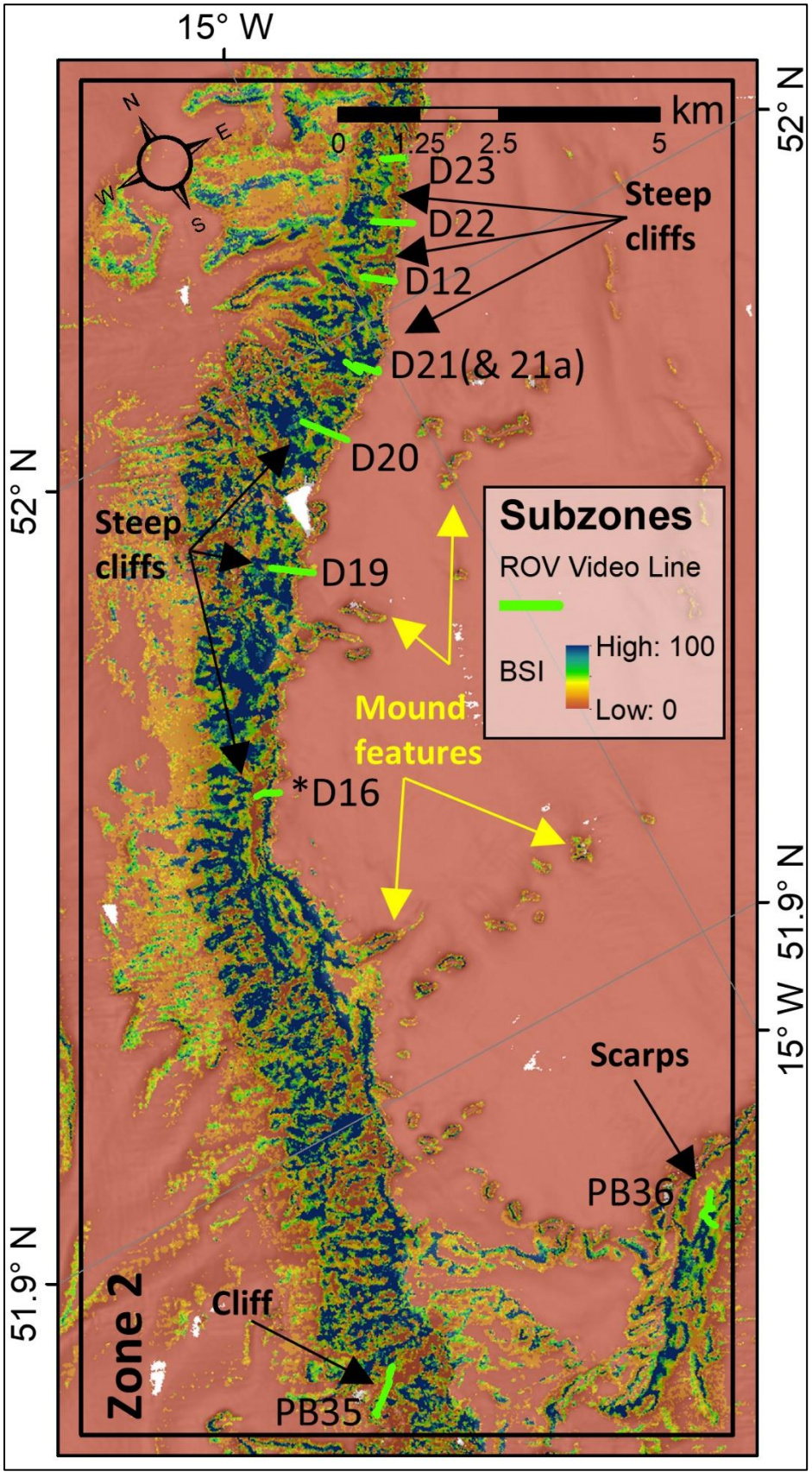


Figure 27: BSI results plotted over terrain in Zone 2, with features labelled.

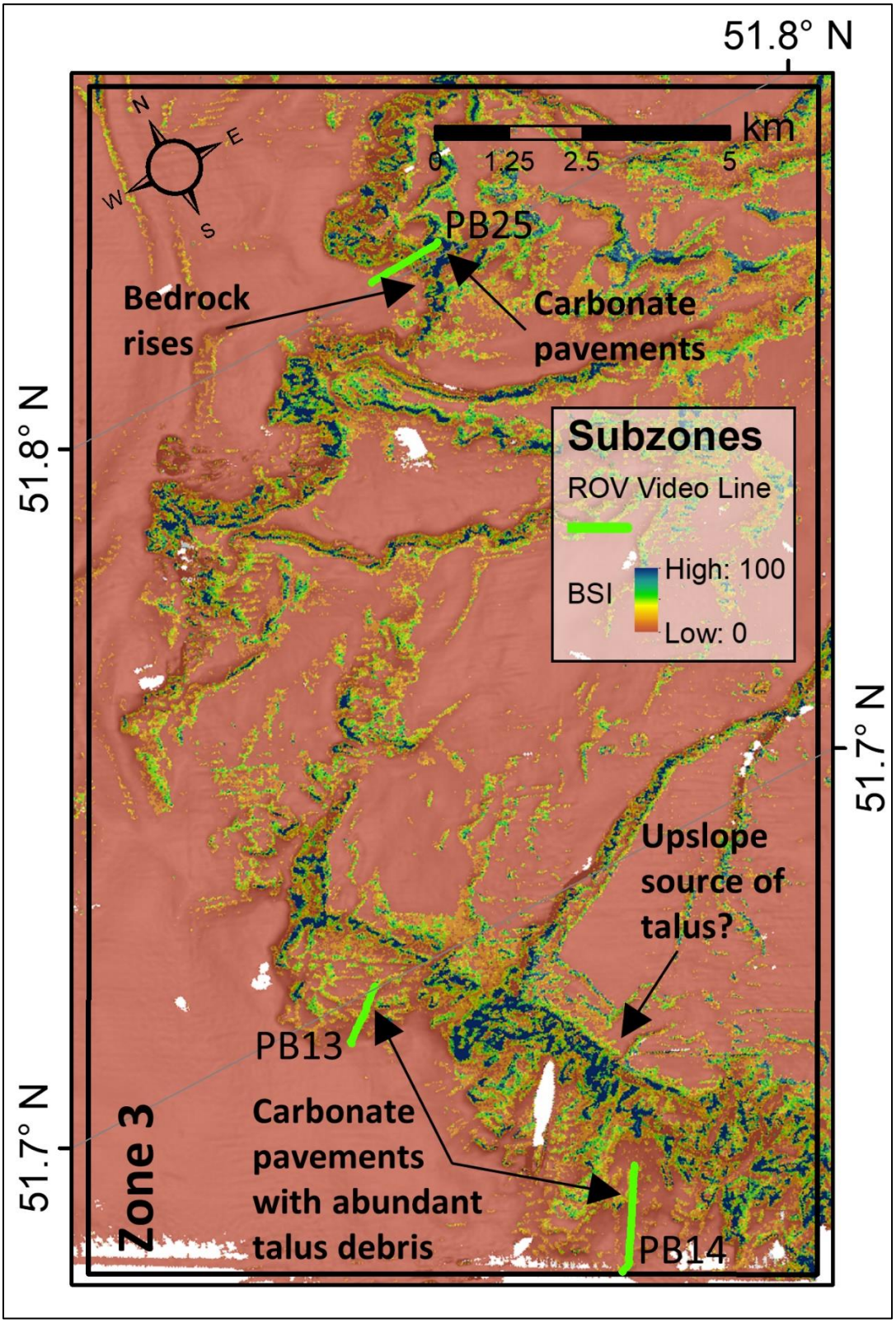


Figure 28: BSI results plotted over terrain in Zone 3, with features labelled.

3.5. DOMs

A total of 17 high-resolution 3D models have been created based on the available footage (Table 4). All data processing outputs were projected to UTM Zone 28N.

Model	Depth (m)	Location (E ; N)	Images	Length (m)	Description
1	-817	500460 ; 5761579	527	20	Exposed cliff face with perpendicular fracture sets and light benthic cover
2	-850	494788 ; 5755247	322	6	Faulted cliff section, sheet like outcrop, moderate sediment cover
3	-834	494788 ; 5755248	217	4	
4	-822	494786 ; 5755250	72	2	Faulted surface with benthic cover
5	-774	496942 ; 5758208	182	12	Small amounts of outcrop (broken in parts) exposed on a moderate slope
6	-825	496952 ; 5758197	282	13	
7	-822	498577 ; 5759826	207	13	Fractured outcrop exposed on a slope
8	-774	501689 ; 5763108	202	8	Small exposed cliff section, light sediment and benthic cover
9	-1134	505333 ; 5769481	217	3	Outcrop location for Sample R2
10	-868	500440 ; 5761619	215	7	Highly fractured cliff face, dense benthic coverage
11	-861	500442 ; 5761621	180	5	
12	-852	500447 ; 5761619	150	1	
13	-849	500449 ; 5761619	290	3	
14	-889	497369 ; 5759257	342	3	Conglomerate (small rounded clasts)
15	-2531	478874 ; 5727643	312	10	Carbonate pavement (with debris)
16	-2498	478976 ; 5727724	347	10	Exposed bedded sequence
17	-2528	481544 ; 5722605	302	12	Collapsed lava tubes on seafloor

Table 4: Summary of 3D models developed during the study (see Appendix C for further details).

3.6. Petrography

Sample R1 has been identified as a metagabbro comprising a lower greenschist facies (low-temperature and moderate-pressure) mineralogy (Figure 29). Labradorite and albite have been altered during sericitization to white mica. Chlorite patches, similarly, have formed from albite alteration. Needle like plagioclase feldspar enclosed in pyroxenes (ophitic) are also observed. Andradite that has been recorded possibly

remains from a calcic protolith, and the epidote recorded is typical of low-to-medium grade regional metamorphism. Accessory minerals in sample R1 include apatite and titanite.

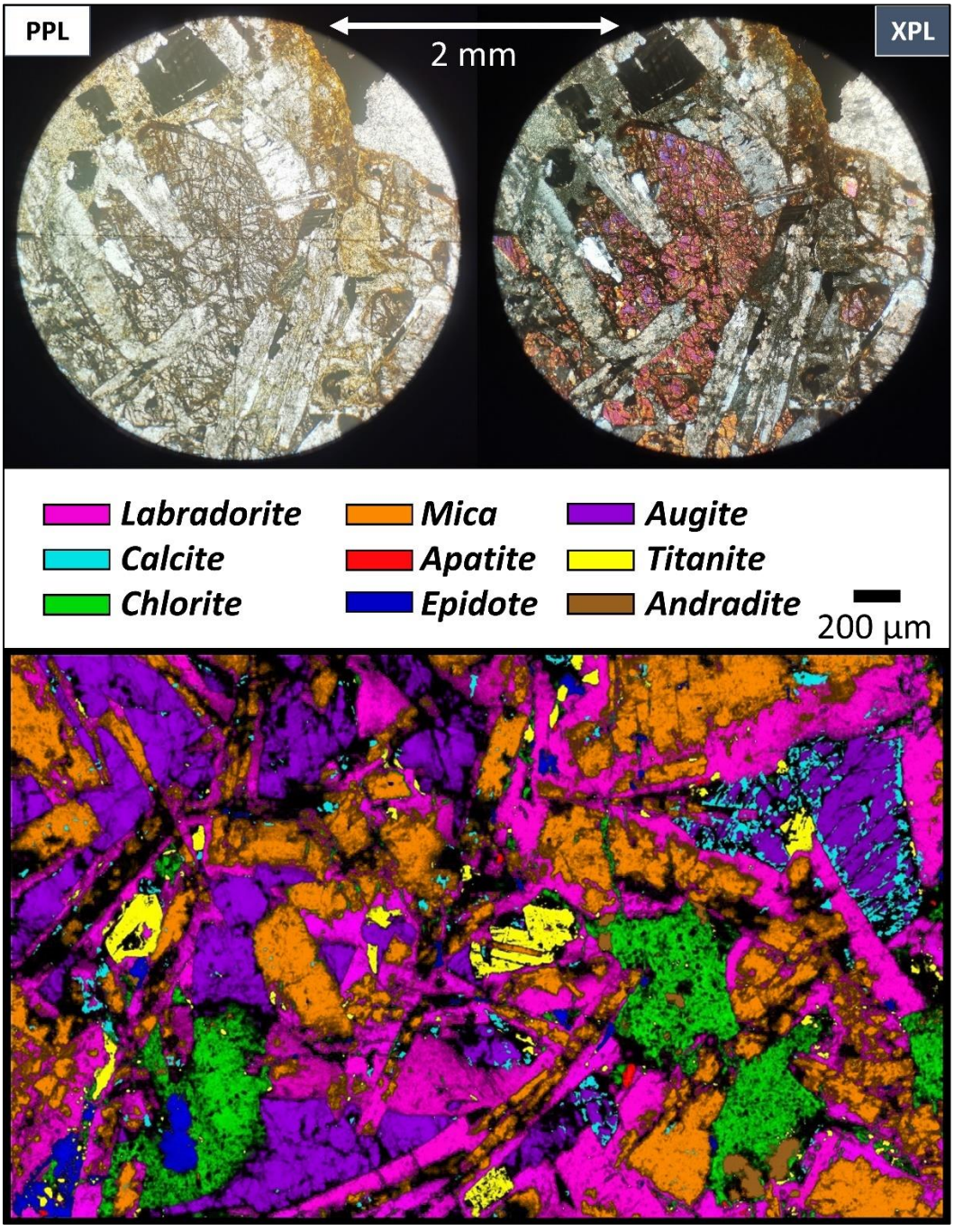


Figure 29: Ophitic texture within the metagabbro portrayed by the needle like plagioclase lathes being engulfed by ?orthopyroxene (top), and mineralogy detailed in Raman map (bottom, key).

Sample R2, similarly, has been identified as a metabasite, comprising a lower greenschist facies mineralogy (Figure 30). The two samples differ in that the metabasite (R2) appears to have undergone a higher degree of alteration to that of the metagabbro (R1). White mica is recorded, replacing plagioclase feldspar, as well as light rims of albite in parts of the analysed surface. Calcite and quartz could have formed similarly under metasomatic conditions. Actinolite is recorded and has replaced FeMg minerals. Accessory minerals in sample R2 include titanite.

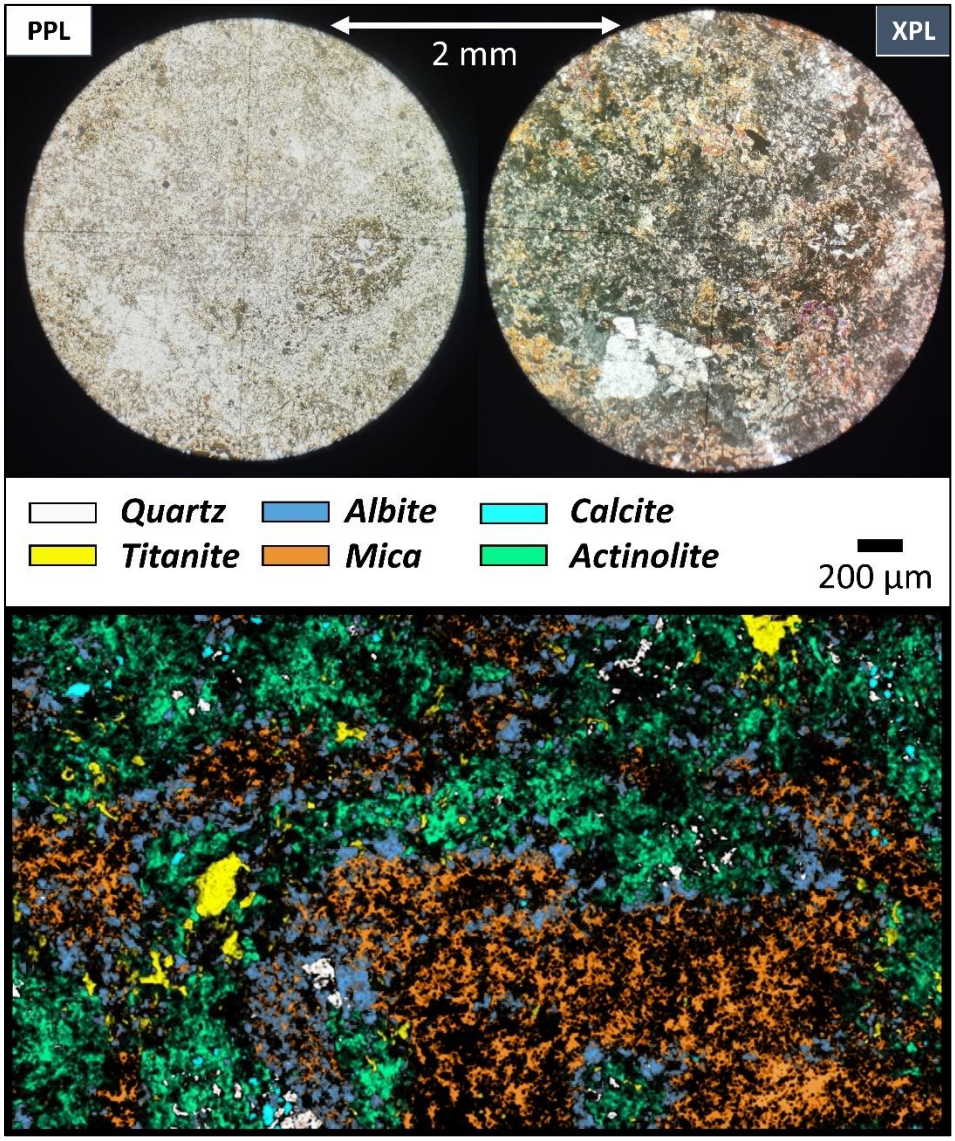


Figure 30: Angular quartz fragment surrounded by fine grained matrix (top), mineralogy detailed in Raman map (bottom, key).

4. Discussion

4.1. Bedrock mapping in the PBC

The results have demonstrated how terrain typical for outcrop occurrence can be delineated in a deep marine setting using IQRs identified for a 'conceptual' suite of surface derivatives (Guisan and Zimmermann, 2000) based on groundtruthed bedrock observations (Figure 15). Although the canyon topography is rather complex and variable, accuracy analysis of the final bedrock suitability map showed that 60% of the validation dataset was correctly predicted (Figure 25-28). This accuracy is in agreement to similar studies which have used terrain attributes to classify the seafloor based on presence only data (Copeland et al., 2013; Joo et al., 2020; Neves et al., 2014).

Outcrop is seen to occur on moderate to steeply sloping seafloor (Figure 18), with gradients generally between 23° and 40°. Higher slope values have been recorded across the study area (e.g. D06, D12 and PB25), which correspond to sharp outcrop rises and cliff sections (Figure 12). This kind of terrain has previously been suggested for the occurrence of rocky outcrop within the canyon and in neighbouring areas along the IAM (O'Reilly et al., 2001; O'Sullivan et al., 2020). Areas where outcrop is recorded appear to correlate with higher roughness and rugosity values (Figure 23 and 24), which are also a good indicator for hard seafloor substrate (D. Dunn and Halpin, 2009). Curvature tends to coincide with outcrop limits on moderately sloping seafloor (e.g. D09 and PB25; Figure 20), however, this is not as evident on the eastern canyon flank, as was the case for BPI reclassification (Figure 21 and 22). In this area, high relief of the flank terrain could make it difficult for features to be resolved (Wilson et

al., 2007). Aspect does not appear to delineate outcrop boundaries well across the study area (Figure 19), however, it provides a surface orientation for which bedrock is facing in the PBC based on the groundtruthed observations (predominantly westward; Figure 15). This in part also results from the eastern canyon flank being a regionally distinct feature along the IAM. The medium to high reflectance values recorded are consistent with similar studies attempting to delineate bedrock exposure in marine settings using backscatter data as a component (Bellec et al., 2017; Joo et al., 2020). The terrain for which bedrock occurrence has been observed and mapped in this study can be partially explained by local and regional factors. A combination of high relief, positive curvature and positive BPI often indicate terrain for which suspended sediment will unlikely be able to settle on a bedrock surface (Guinan et al., 2009; Lundblad et al., 2006; Walbridge et al., 2018). This can also be reflected in the backscatter data for the study area (Figure 16), where lower values are noticeable on flat lying areas with no outcrop observations, such as east of the canyon break (Figure 26). High roughness and rugosity values recorded for areas of bedrock exposure also indicate a complex but distinct terrain, which has previously been identified as important variable for bedrock mapping applications (Diesing et al., 2015; Downie et al., 2016; Brown et al., 2017).

Future applications of BSI mapping in complex marine settings can be more successful by using an increased bathymetric resolution and defining a smaller working (or mapping) area proximal to the observation data being used (Dolan et al., 2008). An increased resolution in MBES data will allow for features in steep terrain (such as in Zone 2 and Zone 3, Figure 27 and 28) to be appropriately resolved, as highlighted by

recent search efforts for Malaysia Airlines flight MH370 (Picard et al., 2017, 2018), which in turn will enhance bedrock mapping outputs.

4.2. Geology of the PBC

Geological interpretation for the PBC may potentially be influenced by the position of available transects on the eastern canyon flank (Figure 5), however, a spread in these dive positions and the inclusion of deeper video lines off the slope and in the southern parts of the canyon have allowed for a more regional interpretation of the canyon's geology.

The drilled bedrock samples presented in this thesis have identified a lower greenschist facies that appears to be present across the upper canyon break and slope based on available imagery (Figure 13(1) and 13(2)). With the proximity of rock type C, which has a gneissic texture and indicates a higher metamorphic grade, it is a possibility that rock types A, B and C could be affiliated with one another, representing components of the local basement high underlying the Porcupine Bank. Metamorphic basement rocks have previously been identified further south along the IAM (Auffret and Auzende, 1986), although a 'large degree of doubt' exists for whether the rock samples in question were of local origin (Masson et al., 1989). There is only thin cover of recent sediments above basement in the PBC (predominantly observed in Zone 2), and extension of the canyon through the IAM has been potentially limited by this erosionally-resistant basement rock, as is this case for other smaller canyons along the IAM (Elliott et al., 2006).

The rounded clasts identified in rock type D, encountered within Zone 2, indicate that the deposits have undergone transportation. These are encountered in deeper depths to

the meta-basement in parts (D21 and D21a), which is a potential result of slope failure along this part of the IAM that has resulted from localised uplift, promoting shelf edge sediment supply from the Porcupine Bank (Elliott et al., 2006). These failures may have been triggered during the Early Cenozoic, where coarse clastic deposition prevailed along the Atlantic margin due to sea level fall and resulting marine regression (Naylor and Shannon, 2011). The slope failures could have been influenced initially by underlying structural fabric, as indicated by the shallow scarp features trending approximately NNE-SSW across the upslope extent of the study area (Figure 25 and 26). These scarps are suggested to reflect an underlying Proterozoic structural fabric which may have been reactivated during Permo-Triassic times (Naylor and Shannon, 2005).

The lightly coloured rock type F encountered off slope and in deeper parts of the study area (PB31 and transects within Zone 3) appears to be chalky deposits. Similar sediments have been encountered further south (Auffret and Auzende, 1986), which have been described as Upper Creataceous deposits resulting from regional eustatic sea level rise combined with thermally-drive subsidence of Atlantic margin basin depocentres (Masson et al., 1989; Naylor and Shannon, 2011).

The southernmost observations in the study area (PB14) are marked by observations of lava flow interactions with the seabed. Well bedded chalk material is overlain by structureless brecciated material within a light matrix (rock type E), interpreted here as a hyaloclast deposit (White et al., 2015). This deposit results from a lava flow riding over the underlying chalk deposit, where a new matrix forms (with yellow hydrothermal staining) by the flow and breakup of the outcrop surface, and contains

clasts of recently cooled igneous fragments and chalk intraclasts (Figure 13(5)). Further evidence for seafloor igneous activity responsible for this is shown by the presence of igneous material amongst the surface of stained carbonate material (PB14), such as small pillows some of which have collapsed in on themselves through quenching (Figure 13(9)). The flows and intrusive materials observed may also relate to Early Cenozoic igneous activity that was widespread along the IAM (Naylor and Shannon, 2011, 2005), resulting from Late Cretaceous rifting (Stoker et al., 2017; Tate and Dobson, 1988).

Rock type G represents a very well bedded sequence of sediments (end of transect PB13) which is seen to overlie chalky outcrop. The submersible dives south of the PBC (Auffret and Auzende, 1986) have encountered well bedded Upper Palaeozoic siltstones and sandstones, which are also seen to overlie carbonate deposits. This is suggested to be a result of numerous normal faults present across the sequence (Masson et al., 1989), which could explain what is recorded here in the PBC (see Model 17, Appendix C).

4.3. Outcrop models

A robust approach to using ROV data and imagery for creating DOMs has been achieved during the study. The high resolution photogrammetric models that have been produced result from different offshore surveys, each bearing their own scientific objectives, and have demonstrated how video data can be repurposed. Regardless, in using the approach outlined here, that is, ensuring suitable transect sections are identified with adequate positioning information for modelling, SfM can be applied to

multipurpose video data, extracted at 5 fps, to produce useful outputs which to be used for further analysis.

The products created have the potential to greatly enhance geological interpretations in this study area and similar deep marine settings. For example, using a high-resolution DEM as a form of bathymetric data, although limited in extent, the structural detail at this resolution cannot be matched by standard MBES surveying in these deep environments (cm to mm resolution). Orthomosaics may also be useful in identifying rock type, based on lithological appearance, which can be enhanced through the likes of the Raster Transform tool in Agisoft Metashape, and the ability to create a continuous geological section to be used for interpretation, as demonstrated by (Kwasti, escartin, Meredyk, Escart). Also, these data outputs are a valuable tool in outreach activities.

4.4. Implications

The outcomes of this study aims to promote future offshore research efforts into the geology of continental margins, as well as push for exploration into the deep earth (Koppers and Coggon, 2020). Knowledge on where further outcrop occurs on the seabed will also promote the identification and mapping of sensitive marine habitats which are particularly diverse on bedrock hardgrounds (Harris and Baker, 2012), and studies on natural hazards which are preserved in the marine geological record (Morgan et al., 2009).

Multi-purpose dives can be planned for sampling of vertical outcrops based on BSI maps in future, along with the collection of video footage, as the two instruments can

often be deployed simultaneously. This will increase time efficiency, enhance sample quality and maximise offshore research opportunities, reducing lack of retrieval situations and limited sampling possibilities by means of bespoke ROV sampling strategies (Meredyk et al., 2020; Trotter et al., 2019). Manned and autonomous surveying systems will benefit these survey efforts both before and after rock sample acquisition, providing a broader dataset, such as regional or local MBES data, for geological interpretation, as demonstrated by Escartín et al. (2017), Joo et al., (2020) and Murton et al. (2019).

In the case of the IAM, data is readily available to extend this study beyond the PBC. The Irish offshore has been extensively mapped through multibeam echosounding over the last two decades by the INFOMAR programme, formerly the Irish National Seabed Survey (GOTECH, 2002; O'Toole et al., 2020). This data now has a groundtruthed context which can be reviewed (O'Sullivan and Shipboard Party, 2019, 2018, 2017), prompting a reappraisal of the bedrock geology for the entire IAM, whilst benefiting further detailed ecological studies in sensitive marine niches (Appah, 2020; O'Sullivan et al., 2020). These research efforts will directly feed into Goal 14 by the United Nations (United Nations, 2015), Life below water – *to conserve and sustainably use the oceans, seas and marine resources for sustainable development*.

5. Conclusions

The deep sea is a challenging environment to conduct sampling strategies in, let alone getting to it. A paucity in our understanding for deep marine geological structure in such settings has resulted from a lack of available information and a need to go and find it. Through the use of sophisticated marine robotics, coupled with high resolution imagery of the seafloor (both its terrain and what lays upon it), advances in deep sea scientific efforts is becoming more possible, in line with a growing need to discover and understand what lies beneath.

This study has demonstrated how combining terrain attributes based on multibeam bathymetry with accurately groundtruthed bedrock observations, the seafloor can be delineated for areas of 'interest', and in this case, hard rock geology. Bedrock suitability mapping can aid in future planning efforts for scientific expeditions, identify targets of interest both for resource management and ecological protection purposes, as well as 'filling the gaps' that exist for deep marine investigation. Terrain characteristics which correlate well to hard and rough bedrock exposure (such as elevated slope, rugosity, and backscatter reflectance values) are seen to be refined through the use of not so distinctive descriptors (such as curvature and BPI).

The quality of the video transects used for this study, their spread, and how they have been applied to a spatial analysis of the surrounding terrain has greatly increased any previous geological studies for the PBC. The results presented here show exposure of basement rock in the canyon flank, situated midway along the IAM. Younger deposits also encountered show evidence for complex formation histories, relating to the development of the Atlantic conjugate margin (and its basins).

ROV technology has successfully demonstrated how we now can have ‘hands’ and ‘eyes’ at the seafloor, enabling geological fieldwork to be conducted at a resolution and confidence that previously was lacking. Future geological, or multidisciplinary, studies in the Irish offshore can elaborate on these findings, making use of the methods presented to make for more efficient surveying, whilst also closing the many data gaps which exist not only around the world, but in our own offshore territory as well.

In the absence of evidence, we cannot rule out the presence of rock type in non-groundtruthed areas. These questions remain open until physically checked, however, BSI mapping provides a quantitative means for acting with caution in such areas. Interpretations based on imagery and geomorphometric analyses are also greatly complimented by the first bedrock samples to be drilled from the seafloor in the PBC, and further bedrock sampling in the offshore will aid in definining what has been found in recent offshore video surveys.

References

Appah, J.K.M., 2020. Are Non-reef Habitats as Important to Benthic Diversity and Composition as Coral Reef and Rubble Habitats in Submarine Canyons? Analysis of Controls on Benthic Megafauna Distribution in the Porcupine Bank Canyon, NE Atlantic. Frontiers in Marine Science 7, 16.

Arndt, J.E., Schenke, H.W., Jakobsson, M., Nitsche, F.O., Buys, G., Goleby, B., Rebesco, M., Bohoyo, F., Hong, J., Black, J., Greku, R., Udintsev, G., Barrios, F., Reynoso-Peralta, W., Taisei, M., Wigley, R., 2013. The International Bathymetric Chart of the Southern Ocean (IBCSO) Version 1.0—A new bathymetric compilation covering circum-Antarctic waters. Geophysical Research Letters 40, 3111–3117. https://doi.org/10.1002/grl.50413

Auffret, G., 1971. GEOMANCHE cruise, RV Jean Carcot. https://doi.org/10.18142/112

Auffret, G., 1975. GEOMANCHE 75/1 cruise, RV Le Suroît.

Auffret, G., Auzende, J.-M., 1986. CYAPORC cruise, RV Le Suroit. https://doi.org/10.17600/86003211

Auffret, G., Auzende, J.-M., Cousin, M., Coutelle, A., Dobson, M., Geoghegan, M., Masson, D., Rolet, J., Vaillant, P., 1987. Géologie des Escarpements de Porcupine et de Goban (N.E. Atlantique). Résultats de la campagne de plongée CYAPORC. Comptes Rendus de l'Academie des Sciences Serie II 304, 1003–1008.

Auzende, J., Cousin, M., Coutelle, A., Dobson, M., Geoghegan, M., Masson, D., Rolet, J., Vaillant, P., 1989. Stratigraphie des escarpements encadrant la baie de Porcupine : résultats préliminaires de la campagne Cyaporc (juillet-août 1986). Oceanologica Acta 12, 117–131.

Backus, S.B., Onishi, R., Bocklund, A., Berg, A., Contreras, E.D., Parness, A., 2020. Design and testing of the JPL-Nautilus Gripper for deep-ocean geological sampling. Journal of Field Robotics 37, 972–986. https://doi.org/10.1002/rob.21934

Bayley, D.T.I., Mogg, A.O.M., 2020. A protocol for the large-scale analysis of reefs using Structure from Motion photogrammetry. Methods in Ecology and Evolution 11, 1410–1420. https://doi.org/10.1111/2041-210X.13476

Becker, K., J.A. Austin Jr., N. Exon, S. Humphris, M. Kastner, J.A. McKenzie, K.G. Miller, K. Suyehiro, and A. Taira, 2019. Fifty years of scientific ocean drilling. Oceanography 32, 17–21, https://doi.org/10.5670/oceanog.2019.110.

Bellec, V.K., Bøe, R., Rise, L., Lepland, A., Thorsnes, T., Bjarnadóttir, L.R., 2017. Seabed sediments (grain size) of Nordland VI, offshore north Norway. Journal of Maps 13, 608–620. https://doi.org/10.1080/17445647.2017.1348307

Bøe, R., Bjarnadóttir, L.R., Elvenes, S., Dolan, M., Bellec, V., Thorsnes, T., Lepland, A., Longva, O., 2020. Revealing the secrets of Norway's seafloor – geological mapping within the MAREANO programme and in coastal areas. Geological Society, London, Special Publications 505. https://doi.org/10.1144/SP505-2019-82

Bogue, R., 2015. Underwater robots: a review of technologies and applications. Industrial Robot: An International Journal 42, 186–191. https://doi.org/10.1108/IR-01-2015-0010

Brown, C.J., Beaudoin, J., Brissette, M., Gazzola, V., 2019. Multispectral Multibeam Echo Sounder Backscatter as a Tool for Improved Seafloor Characterization. Geosciences 9, 126. https://doi.org/10.3390/geosciences9030126

Brown, L.S., S. L. Green, Stewart, H.A., Diesing, M., Anna-Leena Downie, Cooper, R., Lillis, H., 2017. Semi-automated mapping of rock in the Irish Sea, Minches, western Scotland and Scottish continental shelf. https://doi.org/10.13140/RG.2.2.28746.47044

Buckley, S.J., Ringdal, K., Naumann, N., Dolva, B., Kurz, T.H., Howell, J.A., Dewez, T.J.B., 2019. LIME: Software for 3-D visualization, interpretation, and communication of virtual geoscience models. Geosphere 15, 222–235. https://doi.org/10.1130/GES02002.1

Capocci, R., Dooly, G., Omerdić, E., Coleman, J., Newe, T., Toal, D., 2017. Inspection-Class Remotely Operated Vehicles—A Review. Journal of Marine Science and Engineering 5, 13. https://doi.org/10.3390/jmse5010013

Caravaca, G., Le Mouélic, S., Mangold, N., L'Haridon, J., Le Deit, L., Massé, M., 2020. 3D digital outcrop model reconstruction of the Kimberley outcrop (Gale crater, Mars) and its integration into Virtual Reality for simulated geological analysis. Planetary and Space Science 182, 104808. https://doi.org/10.1016/j.pss.2019.104808

Carrivick, J.L., Smith, M.W. and Quincey, D.J., 2016. Current Applications of Structure from Motion in the Geosciences. In Structure from Motion in the Geosciences (eds J.L. Carrivick, M.W. Smith and D.J. Quincey). https://doi.org/10.1002/9781118895818.ch6

Christ, R.D., Wernli, R.L., 2014. Chapter 1 - The ROV Business, in: Christ, R.D., Wernli, R.L. (Eds.), The ROV Manual (Second Edition). Butterworth-Heinemann, Oxford, pp. 3–20. https://doi.org/10.1016/B978-0-08-098288-5.00001-4

CloudCompare (version 2.12) [GPL software], 2012. Retrieved from http://www.cloudcompare.org/

Copeland, A., Edinger, E., Devillers, R., Bell, T., LeBlanc, P., Wroblewski, J., 2013. Marine habitat mapping in support of Marine Protected Area management in a subarctic fjord: Gilbert Bay, Labrador, Canada. J Coast Conserv 17, 225–237. https://doi.org/10.1007/s11852-011-0172-1

De Moustier, C., Matsumoto, H., 1993. Seafloor acoustic remote sensing with multibeam echo-sounders and bathymetric sidescan sonar systems. Mar Geophys Res 15, 27–42. https://doi.org/10.1007/BF01204150

Dewez, T.J.B., Girardeau-Montaut, D., Allanic, C., Rohmer, J., 2016. FACETS : A CloudCompare Plugin to extract geological planes fromunstructured 3d point clouds, in: The International Archives of the Photogrammetry, Remote Sensing and Spatial Information Sciences. Presented at the XXIII ISPRS Congress, Commission V (Volume XLI-B5) - 12–19 July 2016, Prague, Czech Republic, Copernicus GmbH, pp. 799–804. https://doi.org/10.5194/isprs-archives-XLI-B5-799-2016

Diesing, M. Green, S.L., Stephens, D., Cooper, R., Mellett, C.L. 2015. Semi-automated mapping of rock in the English Channel and Celtic Sea. JNCC Report, No. 569. JNCC, Peterborough.

Dolan, M., Grehan, A., Guinan, J., Brown, C., 2008. Modelling the local distribution of cold-water corals in relation to bathymetric variables: Adding spatial context to deep-sea video data. Deep Sea Research Part I: Oceanographic Research Papers 55, 1564–1579. https://doi.org/10.1016/j.dsr.2008.06.010

Dolan, M.F.J., Lucieer, V.L., 2014. Variation and Uncertainty in Bathymetric Slope Calculations Using Geographic Information Systems. Marine Geodesy 37, 187–219. https://doi.org/10.1080/01490419.2014.902888

Doré, A.G., Lundin, E.R., Jensen, L.N., Birkeland, Ø., Eliassen, P.E., Fichler, C., 1999. Principal tectonic events in the evolution of the northwest European Atlantic margin. Petroleum Geology Conference series 5, 41–61. https://doi.org/10.1144/0050041

Dorschel, B., Wheeler, A.J., Huvenne, V.A.I., de Haas, H., 2009. Cold-water coral mounds in an erosive environmental setting: TOBI side-scan sonar data and ROV video footage from the northwest Porcupine Bank, NE Atlantic. Marine Geology 264, 218–229. https://doi.org/10.1016/j.margeo.2009.06.005

Dorschel, B., Wheeler, A.J., Monteys, X., Verbruggen, K., 2010. Atlas of the Deep-Water Seabed: Ireland. Springer Netherlands. https://doi.org/10.1007/978-90-481-9376-9

Dove, D., Bradwell, T., Carter, G., Cotterill, C., Gafeira Goncalves, J., Green, S., Krabbendam, M., Mellett, C., Stevenson, A., Stewart, H., Westhead, K., Scott, G., Guinan, J., Judge, M., Monteys, X., Elvenes, S., Baeten, N., Dolan, M., Thorsnes, T., Bjarnadóttir, L., Ottesen, D., 2016. Seabed geomorphology: a two-part classification system. http://nora.nerc.ac.uk/id/eprint/514946/ (accessed 3.26.21).

Dowdeswell, J., Shears, J., Batchelor, C., Christie, F., Rack, W., Montelli, A., Evans, J., Dowdeswell, E., Ottesen, D., Fawcett, S., Bornman, T., Hutchinson, K., Audh, R., Burger, J., Flynn, R., Henry, T., Luyt, H., Smith, S., Spence, K., Woodall, L., Taylor, M., Frinault, B., Bekker, A., Zu, L., van Zilj, C., Matthee, J., Makgabutlane, M., 2019. The Weddell Sea Expedition 2019: Cruise Scientific Report (Report). https://doi.org/10.17863/CAM.58103

Dowdeswell, J.A., Batchelor, C.L., Dorschel, B., Benham, T.J., Christie, F.D.W., Dowdeswell, E.K., Montelli, A., Arndt, J.E., Gebhardt, C., 2020. Sea-floor and sea-ice conditions in the western Weddell Sea, Antarctica, around the wreck of Sir Ernest Shackleton's Endurance. Antarctic Science 32, 301–313. https://doi.org/10.1017/S0954102020000103

Downie, A.L., Dove, D., Westhead, R.K., Diesing, M., Green, S., Cooper, R. 2016. Semiautomated mapping of rock in the North Sea. JNCC Report No. 592. JNCC, Peterborough.

Dunn, D., Halpin, P., 2009. Rugosity-based regional modeling of hard-bottom habitat. Mar. Ecol. Prog. Ser. 377, 1–11. https://doi.org/10.3354/meps07839

Elliott, G.M., Shannon, P.M., Haughton, P.D.W., Praeg, D., O'Reilly, B., 2006. Mid- to Late Cenozoic canyon development on the eastern margin of the Rockall Trough, offshore Ireland. Marine Geology 229, 113–132. https://doi.org/10.1016/j.margeo.2006.03.008

Eltner, A., Sofia, G., 2020. Chapter 1 - Structure from motion photogrammetric technique, in: Tarolli, P., Mudd, S.M. (Eds.), Developments in Earth Surface

Processes, Remote Sensing of Geomorphology. Elsevier, pp. 1–24. https://doi.org/10.1016/B978-0-444-64177-9.00001-1

Elvenes, S., Bøe, R., Lepland, A., Dolan, M., 2019. Seabed sediments of Søre Sunnmøre, Norway. Journal of Maps 15, 686–696. https://doi.org/10.1080/17445647.2019.1659865

Escartín, J., Mével, C., Petersen, S., Bonnemains, D., Cannat, M., Andreani, M., Augustin, N., Bezos, A., Chavagnac, V., Choi, Y., Godard, M., Haaga, K., Hamelin, C., Ildefonse, B., Jamieson, J., John, B., Leleu, T., MacLeod, C.J., Massot-Campos, M., Nomikou, P., Olive, J.A., Paquet, M., Rommevaux, C., Rothenbeck, M., Steinfuhrer, A., Tominaga, M., Triebe, L., Campos, R., Gracias, N., Garcia, R., 2017. Tectonic structure, evolution, and the nature of oceanic core complexes and their detachment fault zones (13°20′N and 13°30′N, Mid Atlantic Ridge). Geochemistry, Geophysics, Geosystems 18, 1451–1482. https://doi.org/10.1002/2016GC006775

Fonseca, L., Mayer, L., 2007. Remote estimation of surficial seafloor properties through the application Angular Range Analysis to multibeam sonar data. Mar Geophys Res 28, 119–126. https://doi.org/10.1007/s11001-007-9019-4

Gagnevin, D., Haughton, P.D.W., Whiting, L., Saqab, M.M., 2018. Geological and geophysical evidence for a mafic igneous origin of the Porcupine Arch, offshore Ireland. Journal of the Geological Society 175, 210–228. https://doi.org/10.1144/jgs2017-041

Georgiopoulou, A., Huvenne, V., Wynn, R., Iacona, C.L., Braiden, A., Robert, K., Reale., C., De Clipelle, L., Salmanidou, D., Gonzalez, L.V., Tsiantis, I., Chaumillon, L., Hamilton, I., 2014. Slope Collapse on Rockall Bank and Escarpment Habitats (SORBEH): Cruise Report for CE14011 aboard RV Celtic Explorer, UCD, 1-23.

Gonzaga, L., Veronez, M.R., Kannenberg, G.L., Alves, D.N., Santana, L.G., Fraga, J.L. de, Inocencio, L.C., Souza, L.V. de, Marson, F., Bordin, F., Tognoli, F.M.W., Senger, K., Cazarin, C.L., 2018. A Multioutcrop Sharing and Interpretation System: Exploring 3-D Surface and Subsurface Data. IEEE Geoscience and Remote Sensing Magazine 6, 8–16. https://doi.org/10.1109/MGRS.2018.2825990

GOTECH, 2002. Report of the survey in Zone 3 of the Irish National Seabed Survey: Volume 1 describing the results and the methods used. Geological Survey of Ireland, Dublin

Grohmann, C.H., Smith, M.J., Riccomini, C., 2011. Multiscale Analysis of Topographic Surface Roughness in the Midland Valley, Scotland. IEEE Transactions on Geoscience and Remote Sensing 49, 1200–1213. https://doi.org/10.1109/TGRS.2010.2053546

Guinan, J., Grehan, A., Dolan, M., Brown, C., 2009. Quantifying relationships between video observations of cold-water coral cover and seafloor features in Rockall Trough, west of Ireland. Mar. Ecol. Prog. Ser. 375, 125–138. https://doi.org/10.3354/meps07739

Guisan, A., Zimmermann, N., 2000. Predictive habitat distribution models in ecology, Ecological Modelling 135 (2–3), 147-186, https://doi.org/10.1016/S0304-3800(00)00354-9

Harris, P.T., Baker, E.K., 2012. 1 - Why Map Benthic Habitats?, in: Harris, P.T., Baker, E.K. (Eds.), Seafloor Geomorphology as Benthic Habitat. Elsevier, London, pp. 3–22. https://doi.org/10.1016/B978-0-12-385140-6.00001-3

Hudson, I.R., Jones, D.O.B., Wigham, B.D., 2005. A review of the uses of work-class ROVs for the benefits of science: lessons learned from the SERPENT project. Underwater Technology 26, 83–88.

Huggett, Q.J., Kidd, R.B., 1983. Identification of ice-rafted and other exotic material in deep-sea dredge hauls. Geo-Marine Letters 3, 23–29. https://doi.org/10.1007/BF02463438

Huvenne, V.A.I., Tyler, P.A., Masson, D.G., Fisher, E.H., Hauton, C., Hühnerbach, V., Bas, T.P.L., Wolff, G.A., 2011. A Picture on the Wall: Innovative Mapping Reveals Cold-Water Coral Refuge in Submarine Canyon. PLOS ONE 6, e28755. https://doi.org/10.1371/journal.pone.0028755

Ivanov, M., Kenyon, N., Kuijpers, A., Laberg, J., Monteys, X., Nielsen, T., Poulsen, N., 2004. TTR-13 cruise to the North Atlantic: review of the results.

Jakobsson, M., Mayer, L.A., Bringensparr, C., Castro, C.F., Mohammad, R., Johnson, P., Ketter, T., Accettella, D., Amblas, D., An, L., Arndt, J.E., Canals, M., Casamor, J.L., Chauché, N., Coakley, B., Danielson, S., Demarte, M., Dickson, M.-L., Dorschel, B., Dowdeswell, J.A., Dreutter, S., Fremand, A.C., Gallant, D., Hall, J.K., Hehemann, L., Hodnesdal, H., Hong, J., Ivaldi, R., Kane, E., Klaucke, I., Krawczyk, D.W., Kristoffersen, Y., Kuipers, B.R., Millan, R., Masetti, G., Morlighem, M., Noormets, R., Prescott, M.M., Rebesco, M., Rignot, E., Semiletov, I., Tate, A.J., Travaglini, P., Velicogna, I., Weatherall, P., Weinrebe, W., Willis, J.K., Wood, M., Zarayskaya, Y., Zhang, T., Zimmermann, M., Zinglersen, K.B., 2020. The International Bathymetric Chart of the Arctic Ocean Version 4.0. Sci Data 7, 176. https://doi.org/10.1038/s41597-020-0520-9

Jeon, I., Lee, I., 2020. 3D RECONSTRUCTION OF UNSTABLE UNDERWATER ENVIRONMENT WITH SFM USING SLAM, in: The International Archives of the Photogrammetry, Remote Sensing and Spatial Information Sciences. Presented at the XXIV ISPRS Congress, Commission II (Volume XLIII-B2-2020) - 2020 edition, Copernicus GmbH, pp. 957–962. https://doi.org/10.5194/isprs-archives-XLIII-B2-2020-957-2020

Joo, J., Kim, S.-S., Choi, J.W., Pak, S.-J., Ko, Y., Son, S.-K., Moon, J., Kim, J., 2020. Seabed Mapping Using Shipboard Multibeam Acoustic Data for Assessing the Spatial Distribution of Ferromanganese Crusts on Seamounts in the Western Pacific 20.

Kaskela, A.M., Kotilainen, A.T., Alanen, U., Cooper, R., Green, S., Guinan, J., van Heteren, S., Kihlman, S., Van Lancker, V., Stevenson, A., the EMODnet Geology Partners, 2019. Picking Up the Pieces—Harmonising and Collating Seabed Substrate Data for European Maritime Areas. Geosciences 9, 84. https://doi.org/10.3390/geosciences9020084

Kidd, R.B., Huggett, Q.J., Ramsay, A.T.S., 1990. The status of geological dredging techniques. Marine Geophysical Researches 12, 131–143. https://doi.org/10.1007/BF00310568

Kocak, D.M., Dalgleish, F., Caimi, F., Schechner, Y., 2008. A Focus on Recent Developments and Trends in Underwater Imaging. https://doi.org/10.4031/002533208786861209

Koppers, A.A.P., Coggon, R., 2020. Exploring Earth by Scientific Ocean Drilling: 2050 Science Framework. https://doi.org/10.6075/J0W66J9H

Lamarche, G., Lurton, X., 2018. Recommendations for improved and coherent acquisition and processing of backscatter data from seafloor-mapping sonars. Mar Geophys Res 39, 5–22. https://doi.org/10.1007/s11001-017-9315-6

Lecours, V., 2017. Towards a framework for terrain attribute selection in environmental studies. Environmental Modelling 12.

Lecours, V., Dolan, M.F.J., Micallef, A., Lucieer, V.L., 2016. A review of marine geomorphometry, the quantitative study of the seafloor. Hydrology and Earth System Sciences 20, 3207–3244. https://doi.org/10.5194/hess-20-3207-2016

Levin, L.A., Bett, B.J., Gates, A.R., Heimbach, P., Howe, B.M., Janssen, F., McCurdy, A., Ruhl, H.A., Snelgrove, P., Stocks, K.I., Bailey, D., Baumann-Pickering, S., Beaverson, C., Benfield, M.C., Booth, D.J., Carreiro-Silva, M., Colaço, A., Eblé, M.C., Fowler, A.M., Gjerde, K.M., Jones, D.O.B., Katsumata, K., Kelley, D., Le Bris, N., Leonardi, A.P., Lejzerowicz, F., Macreadie, P.I., McLean, D., Meitz, F., Morato, T., Netburn, A., Pawlowski, J., Smith, C.R., Sun, S., Uchida, H., Vardaro, M.F., Venkatesan, R., Weller, R.A., 2019. Global Observing Needs in the Deep Ocean. Front. Mar. Sci. 6. https://doi.org/10.3389/fmars.2019.00241

Lim, A., Huvenne, V.A.I., Vertino, A., Spezzaferri, S., Wheeler, A.J., 2018. New insights on coral mound development from groundtruthed high-resolution ROV-mounted multibeam imaging. Marine Geology 403, 225–237. https://doi.org/10.1016/j.margeo.2018.06.006

Lim , A., O' Reilly, L., Burke, S., Wheeler, A., Appah, J., Summers, G., Harris, K., Shine, A., Boolukos, C., McAleer, A., Conti, L., Blunck, M., Holland 1 ROV technical team, Officers and Crew of the RV Celtic Explorer, 2019. Controls of Cold-Water Coral Habitats in Submarine Canyons (CoCoHaCa II). http://marin egeol ogy.ucc.ie/cruise-repor ts/cruis e-repor t-cocoh aca-ii/

Lim, A., O'Reilly, L.O., Summers, G., Harris, K., Shine, A., Harman, L., Appah, J., Macedo, L., Boyd, J., Anders, B., Killeen, O., Conti, L., Brien, M.O., 2019. Monitoring Changes in Submarine Canyon Coral Habitats - Leg 1 (MoCha_SCan I) Cruise Report, University College Cork, Ireland

Lim, A., Wheeler, A.J., Price, D.M., O'Reilly, L., Harris, K., Conti, L., 2020. Influence of benthic currents on cold-water coral habitats: a combined benthic monitoring and 3D photogrammetric investigation. Sci Rep 10, 19433. https://doi.org/10.1038/s41598-020-76446-y

Lowe, D.G., 2004. Distinctive Image Features from Scale-Invariant Keypoints. International Journal of Computer Vision 60, 91–110. https://doi.org/10.1023/B:VISI.0000029664.99615.94

Lucieer, V., Lecours, V., Dolan, M.F.J., 2018. Charting the Course for Future Developments in Marine Geomorphometry: An Introduction to the Special Issue. Geosciences 8, 477. https://doi.org/10.3390/geosciences8120477

Lundblad, E.R., Wright, D.J., Miller, J., Larkin, E.M., Rinehart, R., Naar, D.F., Donahue, B.T., Anderson, S.M., Battista, T., 2006. A Benthic Terrain

Classification Scheme for American Samoa. Marine Geodesy 29, 89–111. https://doi.org/10.1080/01490410600738021

Macreadie, P., McLean, D., Thomson, P., Partridge, J., Jones, D., Gates, A., Benfield, M., Collin, S., Booth, D., Smith, L., Techera, E., Skropeta, D., Horton, T., Pattiaratchi, C., Bond, T., Fowler, A., 2018. Eyes in the sea: Unlocking the mysteries of the ocean using industrial, remotely operated vehicles (ROVs). Faculty of Science, Medicine and Health - Papers: part A 1077–1091. https://doi.org/10.1016/j.scitotenv.2018.04.049

Marques, A., Horota, R.K., de Souza, E.M., Kupssinskü, L., Rossa, P., Aires, A.S., Bachi, L., Veronez, M.R., Gonzaga, L., Cazarin, C.L., 2020. Virtual and digital outcrops in the petroleum industry: A systematic review. Earth-Science Reviews 208, 103260. https://doi.org/10.1016/j.earscirev.2020.103260

Martín Míguez, B., Novellino, A., Vinci, M., Claus, S., Calewaert, J.-B., Vallius, H., Schmitt, T., Pititto, A., Giorgetti, A., Askew, N., Iona, S., Schaap, D., Pinardi, N., Harpham, Q., Kater, B.J., Populus, J., She, J., Palazov, A.V., McMeel, O., Oset, P., Lear, D., Manzella, G.M.R., Gorringe, P., Simoncelli, S., Larkin, K., Holdsworth, N., Arvanitidis, C.D., Molina Jack, M.E., Chaves Montero, M. del M., Herman, P.M.J., Hernandez, F., 2019. The European Marine Observation and Data Network (EMODnet): Visions and Roles of the Gateway to Marine Data in Europe. Front. Mar. Sci. 6. https://doi.org/10.3389/fmars.2019.00313

Massiot, C., Nicol, A., Townend, J., McNamara, D.D., Garcia-Sellés, D., Conway, C.E., Archibald, G., 2017. Quantitative geometric description of fracture systems in an andesite lava flow using terrestrial laser scanner data. Journal of Volcanology and Geothermal Research 341, 315–331. https://doi.org/10.1016/j.jvolgeores.2017.05.036

Masson, D. G, Dobson, M.R., Auzende, J.-M., Cousin, M., Coutelle, A., Rolet, J., Vaillant, P., 1989. Geology of Porcupine Bank and Goban Spur, Northeastern Atlantic — Preliminary results of the Cyaporc submersible cruise. Marine Geology 87, 105–119. https://doi.org/10.1016/0025-3227(89)90056-X

Mayer, L., Jakobsson, M., Allen, G., Dorschel, B., Falconer, R., Ferrini, V., Lamarche, G., Snaith, H., Weatherall, P., 2018. The Nippon Foundation—GEBCO Seabed 2030 Project: The Quest to See the World's Oceans Completely Mapped by 2030. Geosciences 8, 63. https://doi.org/10.3390/geosciences8020063

Mazzini, A., Akhmetzhanov, A., Monteys, X., Ivanov, M., 2012. The Porcupine Bank Canyon coral mounds: oceanographic and topographic steering of deep-water carbonate mound development and associated phosphatic deposition. Geo-Mar Lett 32, 205–225. https://doi.org/10.1007/s00367-011-0257-8

McCaffrey, K.J.W., Hodgetts, D., Howell, J., Hunt, D., Imber, J., Jones, R.R., Tomasso, M., Thurmond, J., Viseur, S., 2010. Virtual fieldtrips for petroleum geoscientists. Geological Society, London, Petroleum Geology Conference series 7, 19–26. https://doi.org/10.1144/0070019

McCaffrey, K.J.W., Jones, R.R., Holdsworth, R.E., Wilson, R.W., Clegg, P., Imber, J., Holliman, N., Trinks, I., 2005. Unlocking the spatial dimension: digital technologies and the future of geoscience fieldwork. Journal of the Geological Society 162, 927–938. https://doi.org/10.1144/0016-764905-017

McCarthy, J., Benjamin, J., 2014. Multi-image Photogrammetry for Underwater Archaeological Site Recording: An Accessible, Diver-Based Approach. J Mari Arch 9, 95–114. https://doi.org/10.1007/s11457-014-9127-7

McGinnis, T., 2009. Seafloor Drilling, in: Drilling in Extreme Environments. John Wiley & Sons, Ltd, pp. 309–345. https://doi.org/10.1002/9783527626625.ch5

McLean, D., Macreadie, P., White, D., Thomson, P., Fowler, A., Gates, A., Benfield, M., Horton, T., Skropeta, D., Bond, T., Booth, D., Techera, E., Pattiaratchi, C., Collins, S., Jones, D., Smith, L., Partridge, J., 2018. Understanding the Global Scientific Value of Industry ROV Data to Quantify Marine Ecology and Guide Offshore Decommissioning Strategies. Faculty of Science, Medicine and Health - Papers: part A 1–10. https://doi.org/10.4043/28312-MS

McLean, D.L., Parsons, M.J.G., Gates, A.R., Benfield, M.C., Bond, T., Booth, D.J., Bunce, M., Fowler, A.M., Harvey, E.S., Macreadie, P.I., Pattiaratchi, C.B., Rouse, S., Partridge, J.C., Thomson, P.G., Todd, V.L.G., Jones, D.O.B., 2020. Enhancing the Scientific Value of Industry Remotely Operated Vehicles (ROVs) in Our Oceans. Front. Mar. Sci. 7. https://doi.org/10.3389/fmars.2020.00220

Meredyk, S.P., Edinger, E., Piper, D.J.W., Huvenne, V.A.I., Hoy, S., Ruffman, A., 2020. Enigmatic Deep-Water Mounds on the Orphan Knoll, Labrador Sea. Front. Mar. Sci. 6. https://doi.org/10.3389/fmars.2019.00744

Micheletti, N., Chandler, J., Lane, S.N., 2015. Structure from motion (SFM) photogrammetry.

Misiuk, B., Lecours, V., Bell, T., 2018. A multiscale approach to mapping seabed sediments. PLoS ONE 13, e0193647. https://doi.org/10.1371/journal.pone.0193647

Monteys, X., McKeown, C., Conneally, J., O'Rourke, H., Owen, N., Szpak, M., O'Reilly, S., Doyle, J., Forde, J., Ruigork, P., Sandron, P., Murphy, B., 2011. INFOMAR Groundtruthing Program on the Porcupine Bank and Dunmanus Bay, Ireland: Cruise report for CE14011 survey aboard RV Celtic Explorer, Geological Survey of Ireland, Beggars Bush, Dublin 4, 1-51.

Morgan, J.K., Silver, E., Camerlenghi, A., Dugan, B., Kirby, S., Shipp, C., Suyehiro, K., 2009. Addressing Geohazards Through Ocean Drilling. Scientific Drilling 7, 15–30. https://doi.org/10.2204/iodp.sd.7.01.2009

Murton, B.J., Lehrmann, B., Dutrieux, A.M., Martins, S., de la Iglesia, A.G., Stobbs, I.J., Barriga, F.J.A.S., Bialas, J., Dannowski, A., Vardy, M.E., North, L.J., Yeo, I.A.L.M., Lusty, P.A.J., Petersen, S., 2019. Geological fate of seafloor massive sulphides at the TAG hydrothermal field (Mid-Atlantic Ridge). Ore Geology Reviews 107, 903–925. https://doi.org/10.1016/j.oregeorev.2019.03.005

Nagendran, S.K., Ismail, M.A.M., Tung., W.Y., 2019. Photogrammetry Approach On Geological Plane Extraction Using CloudCompare FACET Plugin And Scanline Survey. Bulletin of the Geological Society of Malaysia 68, 151 – 158, https://doi.org/10.7186/bgsm68201916

Nakajoh, H., Miyazaki, T., Sawa, T., Sugimoto, F., Murashima, T., 2016. Development of 7000m work class ROV “KAIKO Mk-IV.” OCEANS 2016 MTS/IEEE Monterey. https://doi.org/10.1109/OCEANS.2016.7761063

Naylor, D., Shannon, P., 2011. Petroleum geology of Ireland. Dunedin Academic Press Ltd, Edinburgh.

Naylor, D., Shannon, P.M., 2005. The structural framework of the Irish Atlantic Margin. Geological Society, London, Petroleum Geology Conference series 6, 1009–1021. https://doi.org/10.1144/0061009

Naylor D., Shannon P., Murphy N. 1999. Irish Rockall Basin region – a standard structural nomenclature system. Petroleum Affairs Division, Dublin, Special Publication 1/99.

Naylor D., Shannon P., Murphy N. 2002. Porcupine–Goban region – a standard structural nomenclature system. Petroleum Affairs Division, Dublin, Special Publication 1/02.

Nesbit, P.R., Durkin, P.R., Hugenholtz, C.H., Hubbard, S.M., Kucharczyk, M., 2018. 3-D stratigraphic mapping using a digital outcrop model derived from UAV images and structure-from-motion photogrammetry. Geosphere 14, 2469–2486. https://doi.org/10.1130/GES01688.1

Neves, B.M., Du Preez, C., Edinger, E., 2014. Mapping coral and sponge habitats on a shelf-depth environment using multibeam sonar and ROV video observations: Learmonth Bank, northern British Columbia, Canada. Deep Sea Research Part II: Topical Studies in Oceanography, Biology and Geology of Deep-Sea Coral Ecosystems: Proceedings of the Fifth International Symposium on Deep Sea Corals 99, 169–183. https://doi.org/10.1016/j.dsr2.2013.05.026

O'Reilly, B.M., Hauser, F., Ravaut, C., Shannon, P.M., Readman, P.W., 2006. Crustal thinning, mantle exhumation and serpentinization in the Porcupine Basin, offshore Ireland: evidence from wide-angle seismic data. Journal of the Geological Society 163, 775–787. https://doi.org/10.1144/0016-76492005-079

O'Reilly, B.M., Readman, P.W., Shannon, P.M., 2001. TOBI Rockall Irish Margins (TRIM): Final Report (Project 97/14a). Report prepared for the Rockall Studies Group, Petroleum Infrastructure Programme, Dundrum, Dublin 14.

O'Sullivan, D., Leahy, Y., Guinan, J., Ross, R., Sacchetti, F., Howell, K., Lyons, D., O'Dowd, L., 2020. The geomorphology and biology of a submarine canyon system incising Ireland's shelf edge in the Northeast Atlantic Ocean, Chapter 47, in Seafloor Geomorphology as Benthic Habitat (Second Edition), 783-792 (Elsevier), https://doi.org/10.1016/B978-0-12-814960-7.00047-6.

O'Sullivan D., Leahy Y., Healy L., 2017. EMFF Offshore Reef Survey, Sensitive Ecosystem Assessment and ROV Exploration of Reef - SeaRover 2018 Cruise Report. Cruise Report prepared by INFOMAR, the Marine Institute, Galway, Ireland and the National Parks and Wildlife Service for the Department of Agriculture, Food and the Marine, the European Maritime and Fisheries Fund and the Department of Culture, Heritage and the Gaeltacht

O'Sullivan D., Leahy Y., Healy L., 2018. EMFF Offshore Reef Survey, Sensitive Ecosystem Assessment and ROV Exploration of Reef - SeaRover 2018 Cruise Report. Cruise Report prepared by INFOMAR, the Marine Institute, Galway, Ireland and the National Parks and Wildlife Service for the Department of Agriculture, Food and the Marine, the European Maritime and Fisheries Fund and the Department of Culture, Heritage and the Gaeltacht

O'Sullivan D., Leahy Y., Healy L., 2019. EMFF Offshore Reef Survey, Sensitive Ecosystem Assessment and ROV Exploration of Reef - SeaRover 2019 Cruise Report. Cruise Report prepared by INFOMAR, the Marine Institute, Galway, Ireland and the National Parks and Wildlife Service for the Department of Agriculture, Food and the Marine, the European Maritime and Fisheries Fund and the Department of Culture, Heritage and the Gaeltacht

O'Toole, R., Judge, M., Sacchetti, F., Furey, T., Craith, E.M., Sheehan, K., Kelly, S., Cullen, S., McGrath, F., Monteys, X., 2020a. Mapping Ireland's coastal, shelf and deep-water environments using illustrative case studies to highlight the impact of seabed mapping on the generation of blue knowledge. Geological Society, London, Special Publications 505. https://doi.org/10.1144/SP505-2019-207

Pastouret, L., 1981. CYMOR 2 cruise, RV Le Suroit. https://doi.org/10.17600/81002111

Pautot, G., 1976. GEOMANCHE 76/2 - CH67 cruise, RV Jean Charcot, https://doi.org/10.17600/76001211

Picard, K., B. Brooke, and M. F. Coffin (2017), Geological insights from Malaysia Airlines flight MH370 search, Eos, 98, https://doi.org/10.1029/2017EO069015.

Picard, K., Brooke, B.P., Harris, P.T., Siwabessy, P.J.W., Coffin, M.F., Tran, M., Spinoccia, M., Weales, J., Macmillan-Lawler, M., Sullivan, J., 2018. Malaysia Airlines flight MH370 search data reveal geomorphology and seafloor processes in the remote southeast Indian Ocean. Marine Geology 395, 301–319. https://doi.org/10.1016/j.margeo.2017.10.014

Pike, R.J., 2000. Geomorphometry -diversity in quantitative surface analysis. Progress in Physical Geography: Earth and Environment 24, 1–20. https://doi.org/10.1177/030913330002400101

Remondino, F., Pizzo, S.D., Kersten, T., Troisi, S., 2012. Low-Cost and Open-Source Solutions for Automated Image Orientation - A Critical Overview, in: EuroMed. https://doi.org/10.1007/978-3-642-34234-9_5

Robert, K., Huvenne, V.A.I., Georgiopoulou, A., Jones, D.O.B., Marsh, L., D. O. Carter, G., Chaumillon, L., 2017. New approaches to high-resolution mapping of marine vertical structures. Scientific Reports 7, 9005. https://doi.org/10.1038/s41598-017-09382-z

Sayab, M., Aerden, D., Paananen, M., Saarela, P., 2018. Virtual Structural Analysis of Jokisivu Open Pit Using 'Structure-from-Motion' Unmanned Aerial Vehicles (UAV) Photogrammetry: Implications for Structurally-Controlled Gold Deposits in Southwest Finland. Remote Sensing 10, 1296. https://doi.org/10.3390/rs10081296

Schimel, A.C.G., Beaudoin, J., Parnum, I.M., Le Bas, T., Schmidt, V., Keith, G., Ierodiaconou, D., 2018. Multibeam sonar backscatter data processing. Mar Geophys Res 39, 121–137. https://doi.org/10.1007/s11001-018-9341-z

Shan, J., Hu, Z., Tao, P., Wang, L., Zhang, S., Ji, S., 2020. Toward a unified theoretical framework for photogrammetry. Geo-spatial Information Science 23, 75–86. https://doi.org/10.1080/10095020.2020.1730712

Sivčev, S., Coleman, J., Omerdić, E., Dooly, G., Toal, D., 2018. Underwater manipulators: A review. Ocean Engineering 163, 431–450. https://doi.org/10.1016/j.oceaneng.2018.06.018

Smith, M.W., Carrivick, J.L., Quincey, D.J., 2016. Structure from motion photogrammetry in physical geography. Progress in Physical Geography: Earth and Environment 40, 247–275. https://doi.org/10.1177/0309133315615805

Stewart, H.A., Jamieson, A.J., 2019. The five deeps: The location and depth of the deepest place in each of the world's oceans. Earth-Science Reviews 197, 102896. https://doi.org/10.1016/j.earscirev.2019.102896

Stoker, M.S., Stewart, M.A., Shannon, P.M., Bjerager, M., Nielsen, T., Blischke, A., Hjelstuen, B.O., Gaina, C., McDermott, K., Ólavsdóttir, J., 2017. An overview of the Upper Palaeozoic–Mesozoic stratigraphy of the NE Atlantic region. Geological Society, London, Special Publications 447, 11–68. https://doi.org/10.1144/SP447.2

Storlazzi, C.D., Dartnell, P., Hatcher, G.A., Gibbs, A.E., 2016. End of the chain? Rugosity and fine-scale bathymetry from existing underwater digital imagery using structure-from-motion (SfM) technology. Coral Reefs 35, 889–894. https://doi.org/10.1007/s00338-016-1462-8

Tate, M.P., Dobson, M.R., 1988. Syn- and post-rift igneous activity in the Porcupine Seabight Basin and adjacent continental margin W of Ireland. Geological Society, London, Special Publications 39, 309–334. https://doi.org/10.1144/GSL.SP.1988.039.01.28

Thiele, S.T., Grose, L., Cui, T., Cruden, A.R., Micklethwaite, S., 2019. Extraction of high-resolution structural orientations from digital data: A Bayesian approach. Journal of Structural Geology 122, 106–115. https://doi.org/10.1016/j.jsg.2019.03.001

Thiele, S.T., Grose, L., Samsu, A., Micklethwaite, S., Vollgger, S.A., Cruden, A.R., 2017. Rapid, semi-automatic fracture and contact mapping for point clouds, images and geophysical data. Solid Earth 8, 1241–1253. https://doi.org/10.5194/se-8-1241-2017

Thorsnes, T., Bellec, V.K., Dolan, M.F.J., 2016. Cold-water coral reefs and glacial landforms from Sula Reef, mid-Norwegian shelf. Geological Society, London, Memoirs 46, 307–308. https://doi.org/10.1144/M46.74

Trotter, J.A., Pattiaratchi, C., Montagna, P., Taviani, M., Falter, J., Thresher, R., Hosie, A., Haig, D., Foglini, F., Hua, Q., McCulloch, M.T., 2019. First ROV Exploration of the Perth Canyon: Canyon Setting, Faunal Observations, and Anthropogenic Impacts. Front. Mar. Sci. 6. https://doi.org/10.3389/fmars.2019.00173

Tyrrel, S., 2013. Geochemical constraints on the age, affinity and history of the Porcupine High - Final Report, Project No., INF-11-02-TYR, Earth and Ocean Sciences, NUI Galway (Galway), 1-26.

Tung, W.Y., Nagendran, S.K., Mohamad Ismail, M.A., 2018. 3D rock slope data acquisition by photogrammetry approach and extraction of geological planes using FACET plugin in CloudCompare. IOP Conf. Ser.: Earth Environ. Sci. 169, 012051. https://doi.org/10.1088/1755-1315/169/1/012051

Umino, S., Nealson, K., Wood, B., 2013. Drilling to Earth's mantle. Physics Today 66, 36. https://doi.org/10.1063/PT.3.2082

United Nations, 2015). Transforming Our World: the 2030 Agenda for Sustainable Development. Available at: https://sustainabledevelopment.un.org/post2015/transformingourworld/publication (accessed March 31, 2021).

Walbridge, S., Slocum, N., Pobuda, M., Wright, D.J., 2018. Unified Geomorphological Analysis Workflows with Benthic Terrain Modeler. Geosciences 8, 94. https://doi.org/10.3390/geosciences8030094

Watremez, L., Prada, M., Minshull, T., O 'reilly, B., Chen, C., Reston, T., Shannon, P., Wagner, G., Gaw, V., Klaeschen, D., Edwards, R., Lebedev, S., 2016. Deep structure of the Porcupine Basin from wide-angle seismic data. Geological Society, London, Petroleum Geology Conference series 1–30. https://doi.org/10.1144/PGC8.26

Weatherall, P., Marks, K.M., Jakobsson, M., Schmitt, T., Tani, S., Arndt, J.E., Rovere, M., Chayes, D., Ferrini, V., Wigley, R., 2015. A new digital bathymetric model of the world's oceans. Earth and Space Science 2, 331–345. https://doi.org/10.1002/2015EA000107

Westoby, M.J., Brasington, J., Glasser, N.F., Hambrey, M.J., Reynolds, J.M., 2012. 'Structure-from-Motion' photogrammetry: A low-cost, effective tool for geoscience applications. Geomorphology 179, 300–314. https://doi.org/10.1016/j.geomorph.2012.08.021

Wheeler, A.J., Beck, T., Thiede, J., Klages, M., Grehan, A., Monteys, F.X., 2005. Deep-water coral mounds on the Porcupine Bank, Irish Margin: preliminary results from the Polarstern ARK-XIX/3a ROV cruise, in: Freiwald, A., Roberts, J.M. (Eds.), Cold-Water Corals and Ecosystems, Erlangen Earth Conference Series. Springer, Berlin, Heidelberg, pp. 393–402. https://doi.org/10.1007/3-540-27673-4_19

Wheeler, A.J., Burke, S., Griffin, B., Lim, A., Ní Fhaolain, F., O'Reilly, L., Summers, G., Holland 1 ROV Technical Team, Officers and Crew of the ILV Granuaile, 2017. Controls of Cold-Water Coral Habitats in Submarine Canyons (CoCoHaCa I). University College Cork, Ireland.

Wheeler, A.J., Capocci, R., Crippa, L., Connolly, N., Hogan, R., Lim, A., McCarthy, E., McGonigle, C., O'Donnell, E., O'Sullivan, K., Power, K., Ryan, G., Vertino, A., Holland 1 ROV Technical Team, Officers and Crew of the RV Celtic Explorer, 2015. Cruise Report: Quantifying Environmental Controls on Cold-water Coral Reef Growth (QuERCi I). University College Cork, Ireland.

Wheeler, A.J., Connolly, N., Conti, L.A., Hogan, R., Lim, A., Massironi, C., Mullins, M., Murphy, P., Pinfield, R., Power, K., Toth, Z., Holland 1 ROV Technical Team, Officers and Crew of the RV Celtic Explorer, 2016. Cruise Report: Quantifying Environmental Controls on Cold-water Coral Reef Growth (QuERCi II). University College Cork, Ireland.

White, J.D.L., McPhie, J., Soule, S.A., 2015. Chapter 19 - Submarine Lavas and Hyaloclastite, in: Sigurdsson, H. (Ed.), The Encyclopedia of Volcanoes (Second Edition). Academic Press, Amsterdam, pp. 363–375. https://doi.org/10.1016/B978-0-12-385938-9.00019-5

Wilson, M.F.J., O'Connell, B., Brown, C., Guinan, J.C., Grehan, A.J., 2007. Multiscale Terrain Analysis of Multibeam Bathymetry Data for Habitat Mapping on the Continental Slope. Marine Geodesy 30, 3–35. https://doi.org/10.1080/01490410701295962

Wölfl, A.-C., Snaith, H., Amirebrahimi, S., Devey, C.W., Dorschel, B., Ferrini, V., Huvenne, V.A.I., Jakobsson, M., Jencks, J., Johnston, G., Lamarche, G., Mayer, L., Millar, D., Pedersen, T.H., Picard, K., Reitz, A., Schmitt, T., Visbeck, M., Weatherall, P., Wigley, R., 2019. Seafloor Mapping – The Challenge of a Truly Global Ocean Bathymetry. Front. Mar. Sci. 6. https://doi.org/10.3389/fmars.2019.00283

Wright, D. J., Lundblad, E. R., Larkin, E. M., Rinehart, R. W., 2005. Benthic Terrain Modeller Toolbar. Oregon State University Davey Jones Locker Seafloor Mapping/Marine GIS Lab.

Wynn, R.B., Huvenne, V.A.I., Le Bas, T.P., Murton, B.J., Connelly, D.P., Bett, B.J., Ruhl, H.A., Morris, K.J., Peakall, J., Parsons, D.R., Sumner, E.J., Darby, S.E., Dorrell, R.M., Hunt, J.E., 2014. Autonomous Underwater Vehicles (AUVs): Their past, present and future contributions to the advancement of marine geoscience. Marine Geology, 50th Anniversary Special Issue 352, 451–468. https://doi.org/10.1016/j.margeo.2014.03.012

Zhang, T., Tang, J., Qin, S., Wang, X., 2019. Review of Navigation and Positioning of Deep-sea Manned Submersibles. The Journal of Navigation 72, 1021–1034. https://doi.org/10.1017/S0373463319000080

Appendices

Appendix A – Datamining results

Appendix B – Bedrock observations

Appendix C – Outcrop models

Appendix A – Datamining results

Any previous bedrock exposure encountered through research surveys in the Irish offshore has been collated in order to create a geodatabase of existing groundtruthed geological data (Figure 31). The following sections provide an overview of the results from these surveys, with a description of the sample material acquired (where possible).

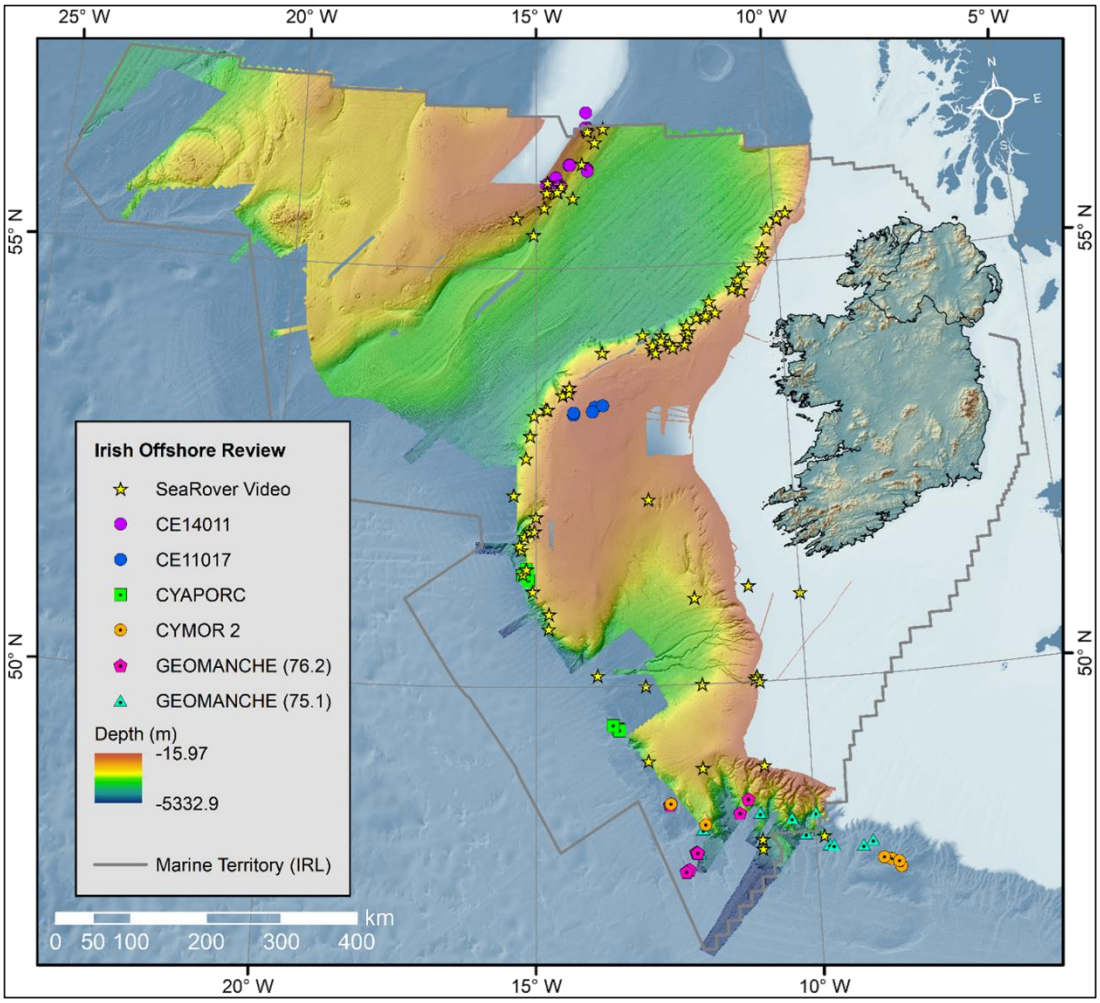


Figure 31: Overview of key datamining findings. INSS (Zone 3) bathymetry (25 m resolution; courtesy of the GSI) overlays bathymetry gathered from EMODnet Bathymetry Consortium 2020 (102 m resolution) (Projection is UTM Zone 28N).

The Irish offshore has been extensively mapped through multibeam echosounding over the last two decades by the INFOMAR programme, formerly the Irish National Seabed Survey (GOTECH, 2002).

Main findings:

- ***SeaRover*** **–** SeaRover is a recent 3-year ROV survey (O'Sullivan and Shipboard Party, 2017, 2018, 2019). The Holland 1 ROV was used to assess biodiversity across biogenic and geogenic reefs in the Irish offshore. It is important to note that the SeaRover video data could not be fully accessed, however, some data were acquired and used for this study (Section 2.2.). For datamining purposes, detailed cruise reports were reviewed, as well as extensive communications with researchers involved with these surveys in order to determine transects of interest for bedrock to have been encountered (Table 5-7). Although 'outcrop' was generally mentioned or described in survey notes and dive summaries, some transects in shallower shelf areas are more ambiguous, but have been included for review purposes as a possibility.

Transect	Lat (SOL)	Long (SOL)	Depth (m)	Lat (EOL)	Long (EOL)	Depth (m)	Notes
1	53.4852	-14.4650	-1088	53.5044	-14.4693	-902	Steep cliffs with outcrop at top of canyon
2	53.5118	-14.3433	-783	53.5200	-14.3275	-694	Hard ground at base of mound
3	53.5795	-14.3294	-739	53.5697	-14.3432	-760	Carbonate sediment, terraces and cliffs
6	53.9876	-13.6577	-1849	53.9743	-13.6676	-1493	Occasional bedrock exposure on steep flank
8	54.1894	-12.8345	-2377	54.1842	-12.8524	-2107	Carbonate cliff and ledges (thin sediment cover)
10	54.0121	-12.6441	-1380	54.0228	-12.6655	-1330	Rocky cliffs and overhangs (thin sediment cover)
11	54.1768	-12.4420	-2357	54.1872	-12.4502	-2140	Carbonate cliff (~50 m in size)
12	54.0751	-12.2873	-1652	54.1203	-12.2616	-1370	Cliffs and vertical walls (southern slope)
13	54.1710	-11.9430	-1442	54.1803	-11.9571	-1307	Areas of outcrop along bottom of canyon

14	54.2127	-11.8935	-1770	54.2253	-11.8842	-1461	Terraced wall
15	54.2847	-11.9330	-2043	54.2949	-11.9423	-1893	Occasional rock
16	54.3721	-11.7208	-2184	54.3905	-11.7115	-1859	Terraces, cliff and pavements (carbonate)
17	54.3799	-11.5692	-1802	54.3923	-11.5619	-1508	Terraces along slope
18	54.3960	-11.5258	-1281	54.4081	-11.5108	-900	Bedrock exposed at base of mound
20	54.6675	-10.7783	-1328	54.6489	-10.7995	-975	Carbonate pinnacle (~30 m in size)
21	54.7040	-10.9530	-739	54.7114	-10.9472	-664	Exposed bedrock with terraces and overhangs
22	54.8041	-10.8339	-2287	54.7855	-10.8550	-2090	Steep and terraced carbonate material
23	54.9327	-10.7013	-2070	54.9498	-10.6922	-1818	Small ledges (<2 m in height, carbonate)
25	55.0304	-10.3063	-1520	55.0421	-10.2930	-1250	Spectacular geological features
27	55.3875	-10.1685	-1976	55.3962	-10.1660	-1873	Rock face (carbonate)
29	55.4925	-9.9514	-1509	55.4844	-9.9391	-1176	Large rock-like cliff with boulders at base of mound
30	55.4984	-9.9392	-1562	55.6521	-9.9409	-1376	Gullies and outcrop at base (towers and spires)
31	55.5633	-9.7538	-967	55.5447	-9.7388	-962	Rock on far side of feature
36	55.1547	-10.2868	-1609	55.1764	-10.2935	-1492	Patches of carbonate outcrop (slope and crest)
39	54.5621	-11.4542	-2460	54.5719	-11.4487	-2232	Cliffs and terraces (thin sediment cover)
40	54.4268	-11.3332	-748	54.4191	-11.3395	-643	Carbonate cliffs, ledges and overhangs
41	54.0627	-12.6356	-1905	54.0728	-12.6525	-1446	Steep bedrock rises and cliffs
42	53.9710	-12.5780	-625	53.9648	-12.5730	-681	Cliffs, overhangs, and ledges (carbonate)
43	54.1137	-12.4610	-1973	54.1253	-12.4790	-1667	Steep bedrock terraces and cliffs on side of canyon
50	54.0282	-12.2253	-650	54.0154	-12.2241	-483	Vertical cliff, with series of ridges
51	54.0627	-11.9840	-527	54.0663	-12.6525	-516	Cliff wall (possibly sandstone)

Table 5: Potential outcrop exposure encountered during SeaRover 1 (2017).

Transect	Lat (SOL)	Long (SOL)	Depth (m)	Lat (EOL)	Long (EOL)	Depth (m)	Notes
RB02	56.6575	-13.9235	-660	56.6735	-13.8755	-489	Some escarpments and vertical walls
RB03	56.6346	-13.8875	-805	56.6498	-13.8952	-830	Vertically exposed bedrock and escarpments
RB26	56.6646	-13.5563	-1604	56.6767	-13.6301	-1589	Carbonate terraces
RB27	56.5038	-13.7388	-1525	56.5090	-13.7378	-1498	Large cliff
RB28	56.2482	-14.0208	-1775	56.2417	-14.0232	-1762	Occasional outcrop and carbonate ledge
RB13	55.8388	-14.2188	-2236	55.8456	-14.2168	-2175	Vertical chalk-like wall overlaid by mud
RB11	55.9813	-14.4685	-1556	55.9913	-14.4669	-1115	Cliff.
RB09	55.9180	-14.5345	-1677	55.9136	-14.5496	-1527	Rocky hard bottom and steep vertical cliff
RB08	55.9136	-14.5496	-1700	55.9156	-14.5590	-1442	Broken hard ground.

RB12	56.0251	-14.7550	-574	56.0382	-14.7495	-508	Ledges and terraces with exposed bedrock
RB24	55.9055	-14.7720	-707	55.8964	-14.7738	-660	Some rock outcrops
RB15	55.7253	-14.8276	-1248	55.7424	-14.8374	-890	Exposed bedrock in parts
RB18	55.5997	-15.4079	-877	55.5910	-15.4195	-879	Frequent bedrock exposure
RB23	55.4009	-15.0515	-2308	55.4258	-15.0563	-2252	Occasional rocks and outcrop exposure
PB01	53.3208	-14.8021	-1852	53.3297	-14.7869	-1687	Small carbonate outcrops
PB02	53.3181	-14.7703	-1548	53.3189	-14.7458	-1262	Vertical cliffs, outcrop and ledges
PB03	53.2425	-15.0420	-2367	53.2448	-15.0207	-2105	Vertical carbonate cliff
PB05	53.0037	-15.1142	-2270	53.0132	-15.0916	-1982	Large wall
PB08	52.7359	-15.1964	-2122	52.7443	-15.1709	-1857	Rock outcrops observed.
PB09	52.2946	-15.4335	-2674	52.3032	-15.4383	-2456	Outcrop and a large carbonate wall
PB25	51.8014	-15.2187	-2533	51.8023	-15.1985	-2010	Steep black cliff
PB14	51.6408	-15.2812	-2839	51.6554	-15.2656	-2490	Steep rocky incline
PB17	51.3487	-15.2520	-2739	51.3517	-15.2423	-2336	Large cliff (possibly basalt)
PB27	51.1432	-15.0624	-2114	51.1378	-15.0460	-1789	Possible pillow lava encountered
PB19	50.6974	-14.7622	-2591	50.7004	-14.7527	-2067	Cliff face
PB20	50.8714	-14.7561	-1946	50.8763	-14.7489	-1719	Large carbonate wall
PB16	51.4104	-15.1843	-2717	51.4174	-15.1718	-1898	Very steep cliff with exposed bedrock in parts
PB13	51.6949	-15.3159	-2786	51.7004	-15.3034	-2476	Occasional bedrock and carbonate exposure
PB35	51.8614	-15.1204	-2000	51.8665	-15.1118	-1678	Vertical and sloping carbonate and bedrock
PB36	51.8621	-15.0303	-952	51.8667	-15.0276	-799	Vertical wall with bedrock crust
PB31	52.0333	-15.0000	-1722	52.0419	-14.9807	-1497	Carbonate wall
PB23	52.2255	-12.8153	-737	52.2271	-12.8233	-596	Areas of bedrock exposed (with crevices)

Table 6: Potential outcrop exposure encountered during SeaRover 2 (2018).

Transect	Lat (SOL)	Long (SOL)	Depth (m)	Lat (EOL)	Long (EOL)	Depth (m)	Notes
37	50.0683	-10.8979	-2884	48.0669	-9.9998	-2657	Occasional terraces and cliffs
39	48.1187	-9.8481	-1184	48.1178	-9.8496	-1026	Carbonate pillars, igneous rocks, escarpments
41	48.1181	-10.9479	-1074	48.1167	-10.9976	-941	Occasional rock outcrops
43	48.0027	-10.9499	-1328	49.0008	-10.9325	-1003	Vertical carbonate cliff
45	49.0004	-10.8485	-1393	49.0012	-10.8475	-1244	Basalt rocks and carbonate terraces
36	49.0002	-11.9656	-1793	49.0013	-11.9662	-1671	Rocky outcrops (upslope)
34	49.1002	-12.9491	-2990	49.1004	-12.9488	-2868	Rocky ridge
30	50.0002	-12.9641	-2892	50.0007	-12.965	-2771	Exposed bedrock slope and cliff section
15	51.1509	-10.9665	-901	51.1526	-10.9647	-888	Soft sediment interspersed with rocks
22	51.0348	-9.9981	-147	51.0356	-9.9992	-145	Rocky outcrops (sparse) on muddy seafloor
27	50.0683	-10.8979	-1097	50.0687	-10.8993	-806	Steep cliff with relict coral
26	50.0334	-10.9311	-1587	50.0524	-10.9481	-1177	Steep canyon wall
25	50.0008	-10.8484	-1940	50.0015	-10.8484	-1916	Canyon wall
53	50.0002	-11.9167	-2511	50.0013	-11.9163	-2487	Canyon escarpment

4	50.1348	-13.8498	-2970	50.1359	-13.8498	-2650	Vertical steep walls with an areas of bedrock
12	51.0353	-11.9985	-1617	51.0346	-11.9995	-1484	Occasional rock outcrop
13	51.0352	-11.9976	-1333	51.0336	-11.999	-1228	Rocks encountered

Table 7: Potential outcrop exposure encountered during SeaRover 3 (2019).

- ***CE14011*** **–** During CE14011 (Table 8), rock samples were picked using the Holland 1 ROV manipulator arm from steep escarpment features on the Eastern Rockall Bank (personal communications with Dr. Aggeliki Georgiopoulou, chief scientist of CE14011; Georgiopoulou and Shipboard Party, 2014).

Dive	Sample #	Lat	Long	Depth (m)	Event Notes
2	5A	54.8575	-13.9143	-604	BBX06
	9	56.6546	-13.9143	-574	GEO01
3	4A	56.6746	-13.9023	-636	BBX02
	4B	54.1836	-13.9031	-608	BBX03
	4C	56.6783	-13.903	-574	BBX04
	4D	56.6788	-13.9028	-517	BBX05
	6D	54.1678	-13.9028	-509	BBX06
	11C	54.1621	-13.9027	-496	BBX07
4	1	56.6769	-13.9199	-596	BBX01
	2	56.6772	-13.9227	-557	BBX02
	3E	56.6789	-13.9227	-557	BBX03
	4D	56.6789	-13.9228	-546	BBX04
	5	56.6789	-13.9230	-526	BBX05
	6	56.6794	-13.9235	-510	BBX06
	7	56.6797	-13.9237	-502	BBX07
	8	56.6803	-13.9244	-458	BBX08
7	5	56.2383	-14.2792	-1056	BBX04
	10	56.2362	-14.2865	-909	BBX06
	12	56.2359	-14.2867	-899	BBX07
	13	56.2359	-14.2867	-899	BBX08
8	3	56.2337	-14.2935	-926	BBX02
	6	56.2338	-14.2934	-922	BBX04
	7	56.2338	-14.2934	-922	BBX05
	11	56.2320	-14.2742	-1066	BBX06
9	3	56.0696	-14.5719	-888	BBX02
	7	56.0783	-14.5826	-831	BBX04
	11	56.0841	-14.5782	-762	BBX07
10	3	55.9776	-14.4804	-1565	BBX01
	4	55.9776	-14.4804	-1565	BBX02

	8	55.9887	-14.4680	-1296	BBX05
	9	55.9887	-14.4680	-1296	BBX06
	10	55.9809	-14.4914	-1550	TBE03
	15	55.9748	-14.4946	-1389	BBX08
13	2	56.0042	-14.7722	-586	BBX01

Table 8: Summary of samples collected during CE14011 (SORBEH) by ROV manipulator arm.

- ***CE11017*** **–** During CE11017 (Monteys and Shipboard Party, 2011), a rock dredge was used to acquire samples from outcrop on the Porcupine High (Table 9).

Sample	Lat	Long	Depth (m)	Notes
CE11_031	53.2717	-14.2500	-215	Small recovery of biogenic content
CE11_032	53.2755	-14.2498	-215	
CE11_033	53.2692	-14.2419	-212	2 large clasts recovered
CE11_034	53.2522	-14.2556	-209	
CE11_049	53.2881	-13.8748	-159	Boulders and cobbles of predominantly sandstone with minor mudstone, and gravels
CE11_050	53.2845	-13.8716	-160	
CE11_051	53.3219	-13.8730	-151	Boulders, cobbles and pebbles of quartz arenite and sandstone
CE11_052	53.3415	-13.8242	-152	
CE11_053	53.3700	-13.7940	-149	Boulders and cobbles of quartz arenite and sandstone. Mostly pebbles of various lithologies
CE11_054	53.3572	-13.6678	-154	

Table 9: Summary of dredge sample material recovered during CE11017.

Summary of CE11017 findings (from Tyrrel, 2013):

- Approximately 80% of the dredged sample material was of a similar lithology, described onboard as green-reddish-brown sandstones. This provides strong confidence that the material represents the bedrock geology of the high, and had not been transported from elsewhere.
- The metasedimentary rocks can be classified as quartzo-feldspathic psammites (metamorphosed sandstone). These comprise in excess of 15% K-feldspar, dominated by quartz, and there has been significant quartz recrystallisation (likely during metamorphism) such that primary sedimentary grain boundaries can only rarely be seen. Heavy mineral bands are frequently observed in many of the

samples, comprising of a diverse range of accessory phases (zircon, apatite, epidote, titanite and ilmenite).

- The petrography of these samples suggests that these metasediments are sourced from granites and gneisses. The oldest possible age for these Porcupine High Metasedimentary Sequence (PHMS) samples is suggested to 872 Ma, based on zircon geochronological analysis. This age suggests that deposition occurred subsequently to the Grenville Orogeny, and metamorphism has likely taken place during Grampian Orogeny (~470 Ma).

➢ ***IFREMER –*** Multiple surveys have been undertaken by IFREMER in the Irish offshore (CYAPORC, CYMOR 2, and GEOMANCHE). These have acquired bedrock samples by means of submersible manipulator arm and rock dredges (Table 10).

Survey	Operation	Lat	Long
CYAPORC	CY86-D-32	51.4095	-15.1842
	CY86-D-33	51.2712	-15.1412
	CY86-D-34	51.3383	-15.2520
	CY86-D-37	49.4985	-13.4940
	CY86-D-39	49.4882	-13.4902
	CPO-DR01	51.3583	-15.1497
	CPO-DR03	49.4745	-13.4639
	CPO-DR04	49.5335	-13.5782
CYMOR 2	CY81-DR21	47.6897	-8.5217
	CY81-DR22	47.6913	-8.5213
	CY81-DR23	47.7833	-8.6850
	CY81-DR24	47.8112	-8.8145
	CY81-DR25	47.7508	-8.5508
	CY81-DR26	48.5823	-12.5600
	CY81-DR27	48.5825	-12.5667
	CY81-DR28	48.3187	-11.9563
	CY81-DR29	48.3200	-11.9550
GEOMANCHE 76/2	CH67-DR07	47.9967	-12.1400
	CH67-DR08	47.9967	-12.1283
	CH67-DR09	47.9817	-12.1133
	CH67-DR10	47.9867	-12.1183

	CH67-DR11	47.7917	-12.2700
	CH67-DR12	47.7817	-12.3067
	CH67-DR13	47.7667	-12.3267
	CH67-DR16	48.5700	-12.5850
	CH67-DR18	48.5800	-12.5717
	CH67-DR20	48.4433	-11.3317
	CH67-DR21	48.6050	-11.1683
GEOMANCHE 75/1	DR01	48.0283	-8.9883
	DR02	47.9768	-9.1583
	DR03	48.0083	-9.7633
	DR04	48.0000	-9.6867
	DR05	48.1950	-9.9167
	DR06	48.4000	-9.9750
	DR07	48.3567	-10.4033
	DR08	48.3510	-10.4067
	DR09	48.1567	-10.1667
	DR10	48.4333	-10.9700
	DR11	48.2667	-12.0000
	DR12	47.9850	-12.0817

Table 10: Summary of geological samples acquired by IFREMER through submersible dives and rock dredging.

- ***CYAPORC* –** In 1986, the CYAPORC survey was conducted using the French submersible CYANA (IFREMER) aboard RV *Le Suroit*, to collect rock samples and video footage along the margin of the southern Porcupine Bank and Goban Spur (Aufret and Auzende, 1986).
- ***CYMOR 2* –** In 1981, the CYMOR 2 survey was conducted using the French submersible CYANA (IFREMER) aboard RV *Le Suroit*, to collect rock samples and video footage along the southern end of the IAM, south of the Goban Spur (Pastouret, 1981).
- ***GEOMANCHE (76/2)* –** In 1976, GEOMANCHE concluded with 76/2 (CH67), conducting rock dredge sampling aboard RV *Jean Charcot* along the southern end of the IAM, south of the Goban Spur (Pautot, 1976).
- ***GEOMANCHE (75/1)* –** In 1975, GEOMANCHE began in Irish waters, conducting rock dredge sampling aboard RV *Jean Charcot*

along the southern end of the IAM, south of the Goban Spur (Auffret, 1975).

- **TTR13 –** During TTR13, a rock dredge was used in an attempt to target bedrock exposed along the escarpment features to the SW of the study area (Ivanov, Mazzini).
    - The results of these rock dredges were located and collected in Dublin as part of this study (GSI, Beggars Bush; Figure 32).
    - Based on extensive discussions with people involved with TTR13, and upon reviewing more recently collected video data along these escarpments, the rock samples collected by means of dredge could not confidently be ascribed to local in situ bedrock exposure.
    - It is likely the samples in question represent some of the abundant IRD which is seen to occur along these escarpments**.**

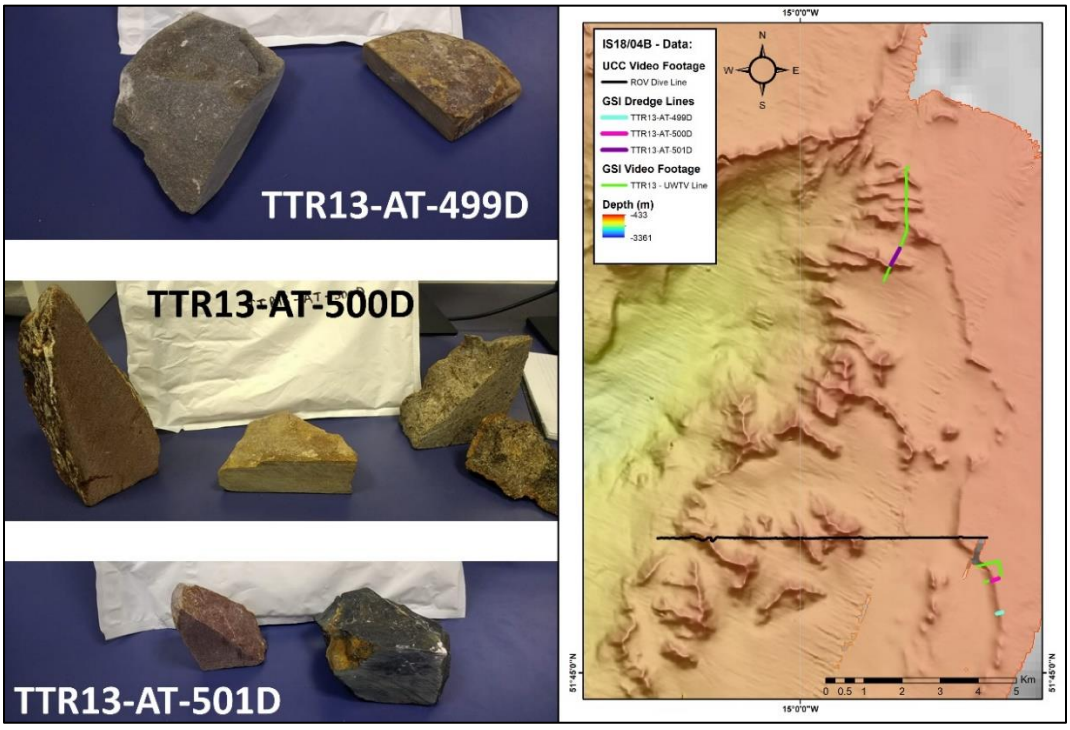


Figure 32: Findings from TTR13 (courtesy of GSI).

Appendix B – Bedrock observations

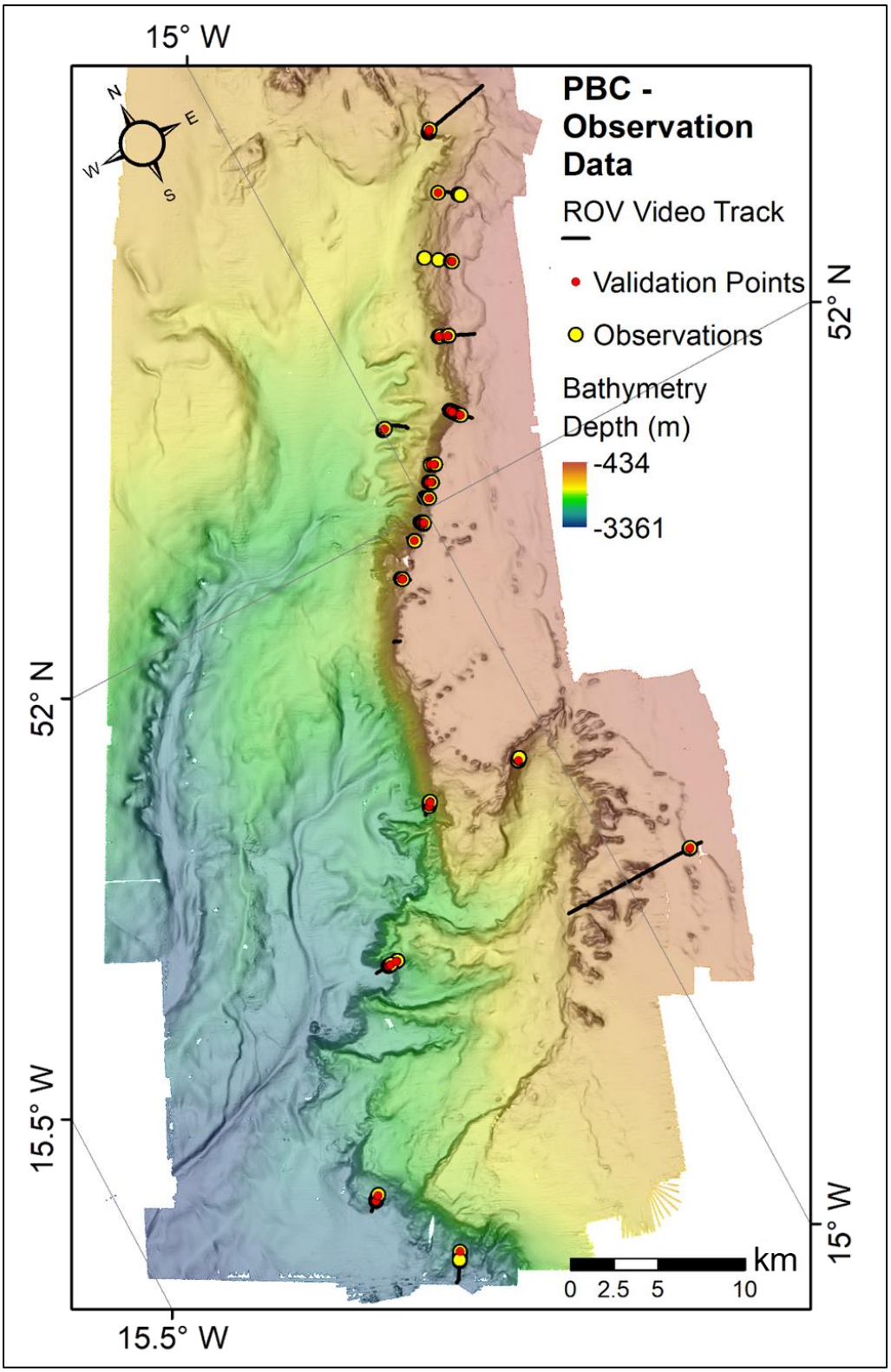


Figure 33: Overview map of PBC, showing where bedrock observations have been encountered across the study site, and the validation data used to test the accuracy of the BSI mapping,

Appendix C – Outcrop models

A total of 17 high-resolution 3D models were developed during the study. For each model, a DEM and orthomosaic (*.tif), a 3D model (*.obj) and 3D *.pdf was created.

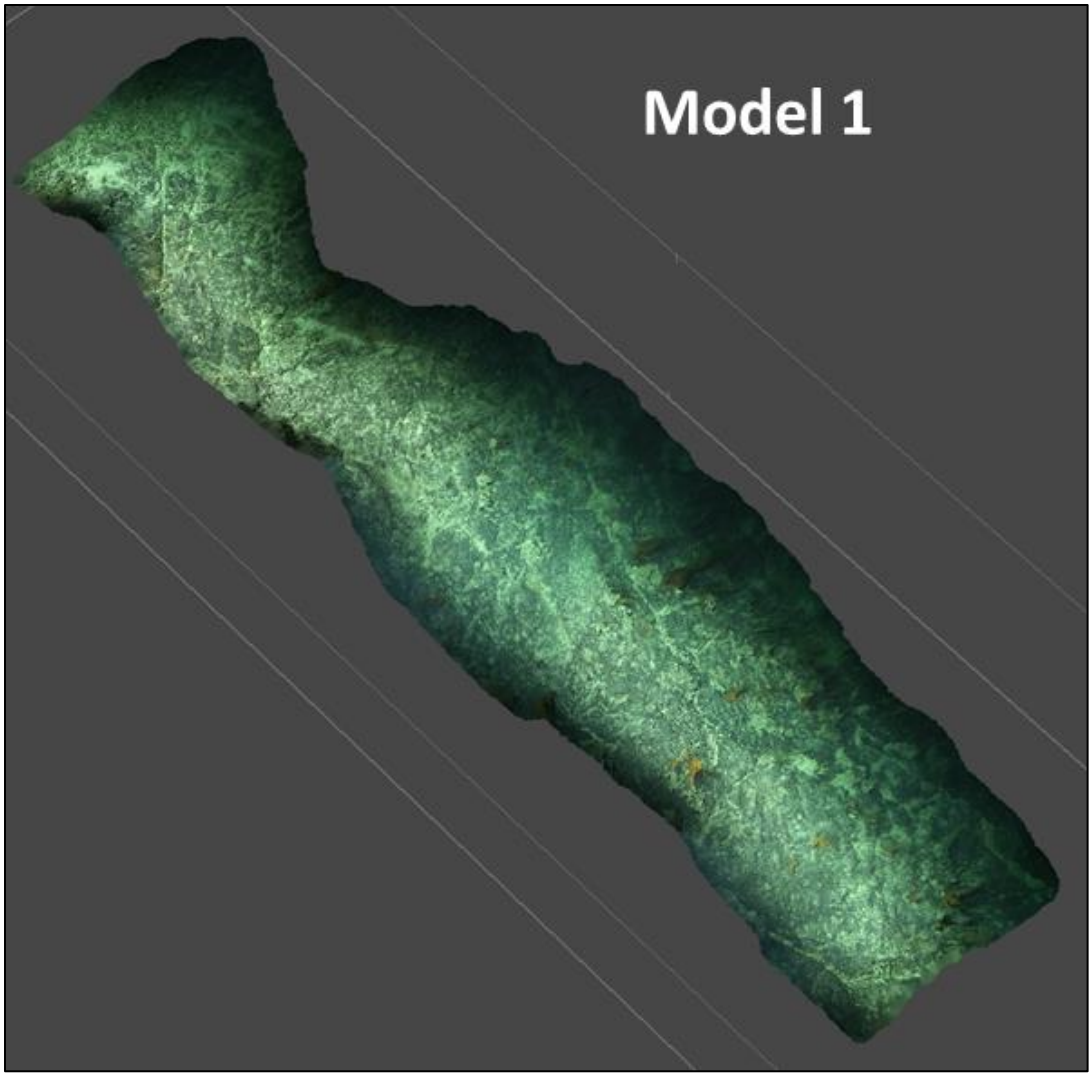


Figure 34: Model 1 from the PBC (approx.. 20 m in length).

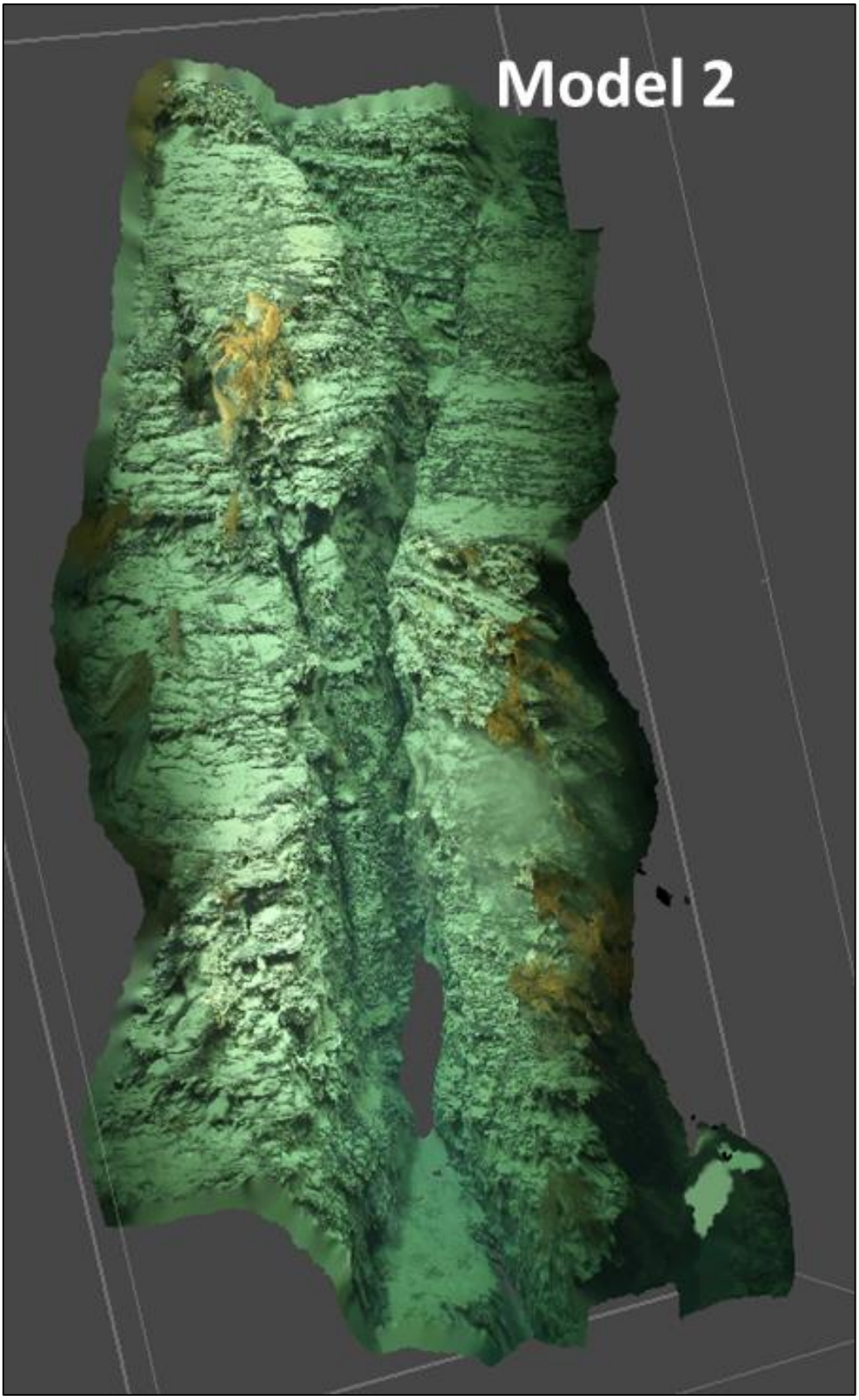


Figure 35: Model 2 from the PBC (approx.. 5 m in length).

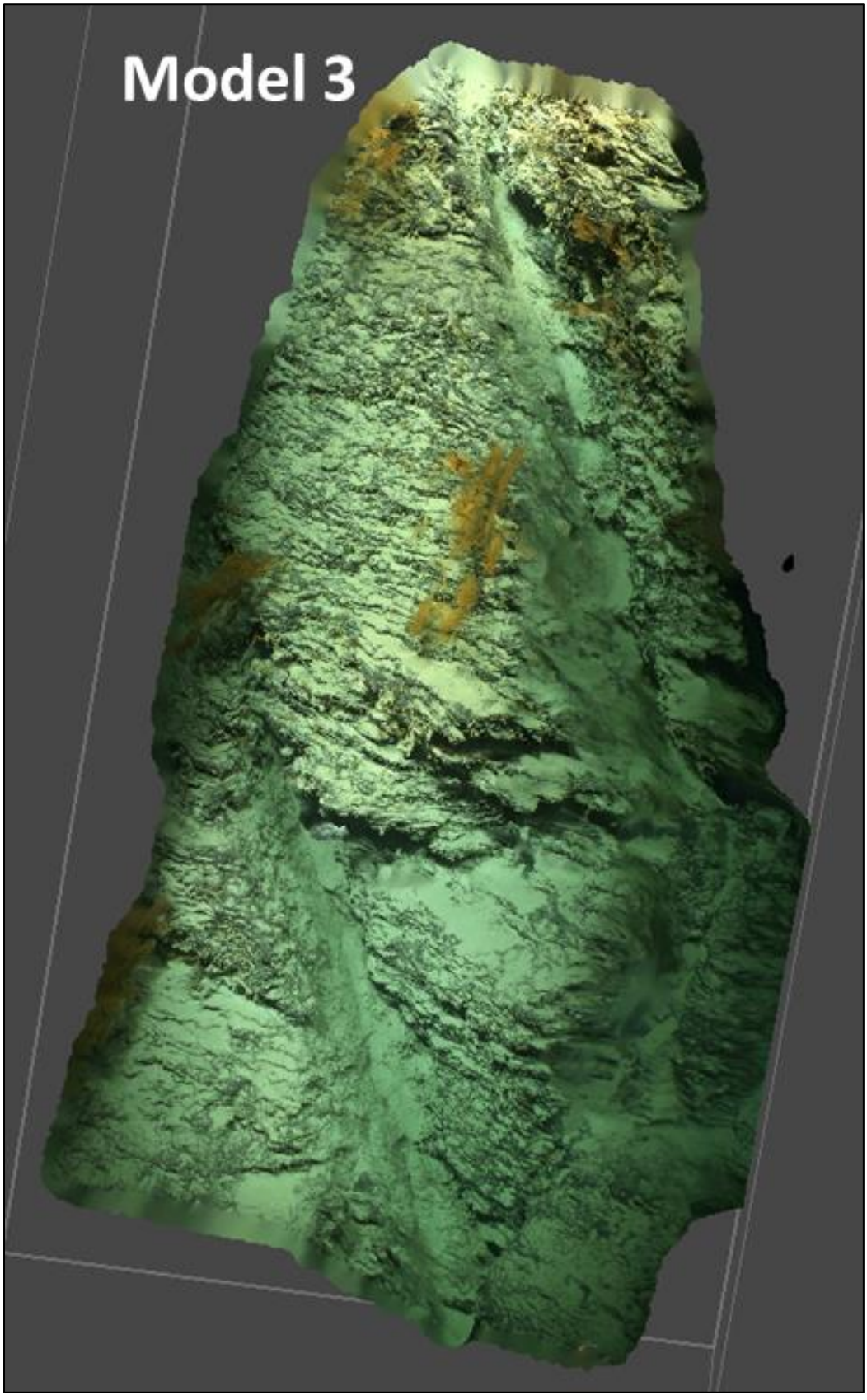


Figure 36: Model 3 from the PBC (approx.. 4 m in length).

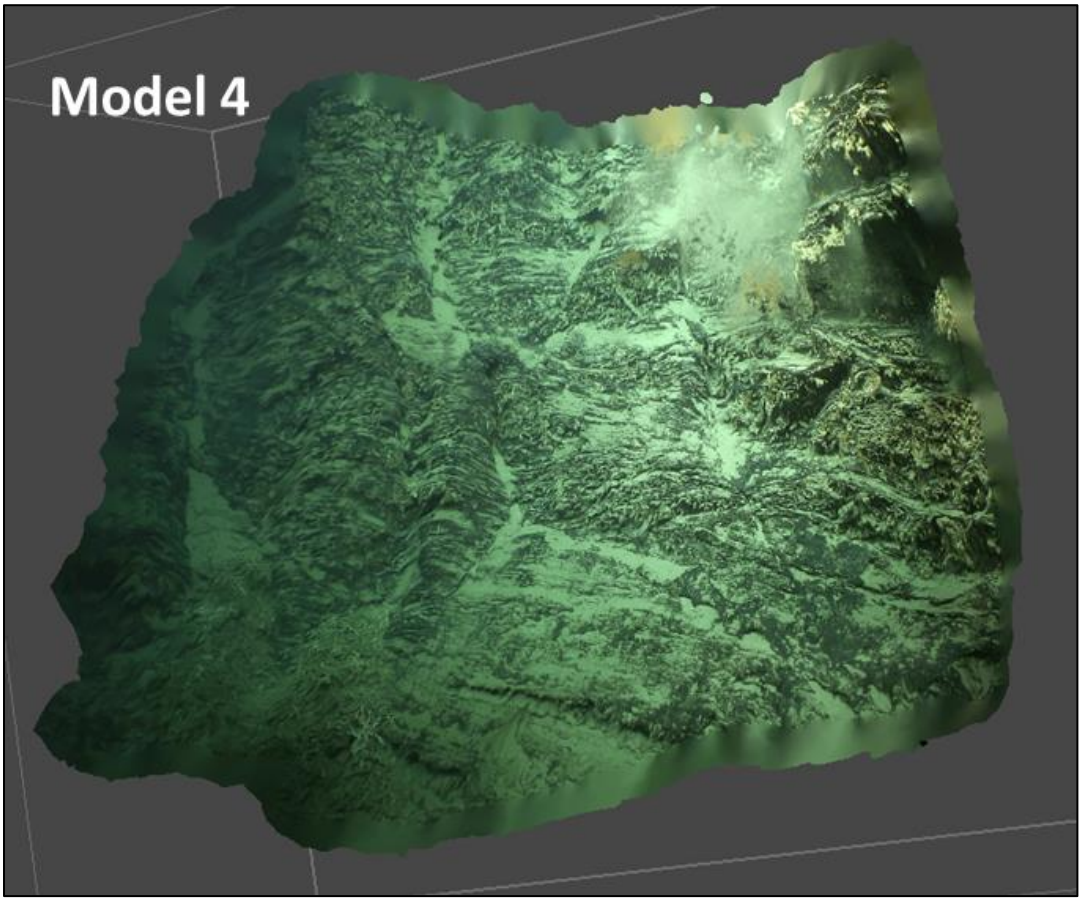


Figure 37: Model 4 from the PBC (approx.. 3 m in length).



Figure 38: Model 5 from the PBC (approx.. 12 m in length).

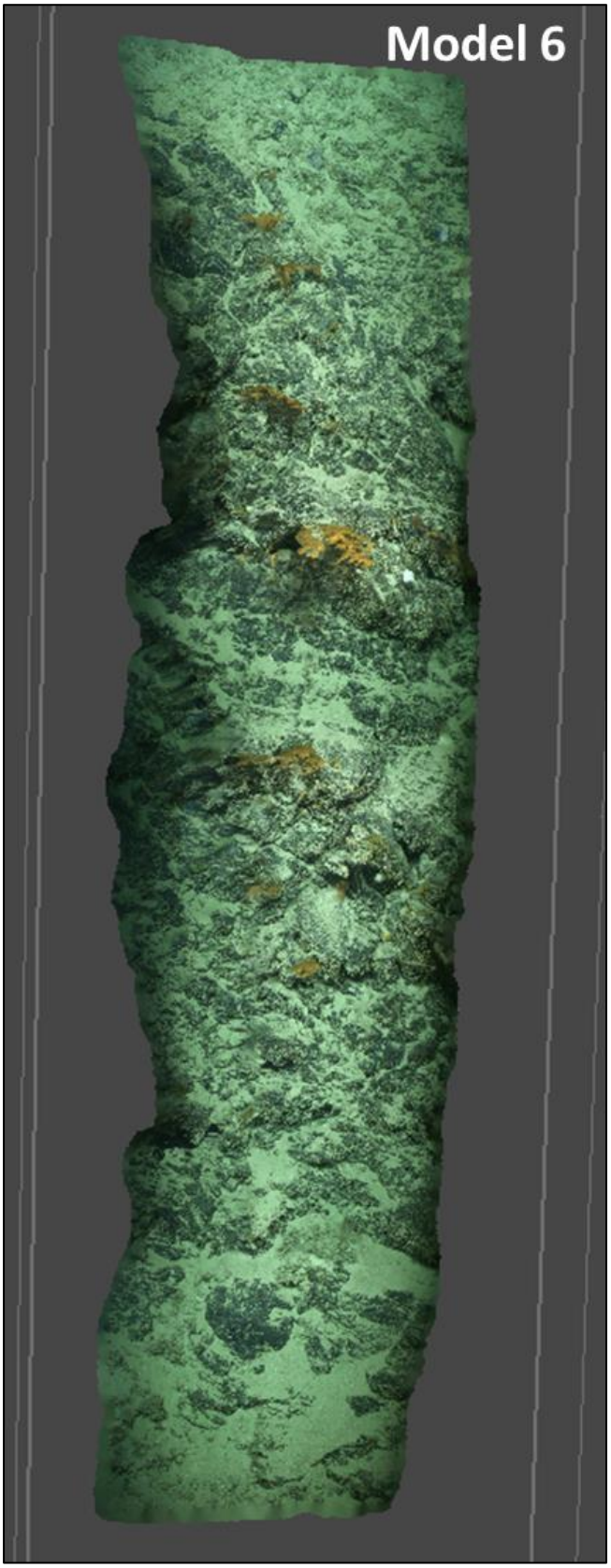


Figure 39: Model 6 from the PBC (approx.. 13 m in length).

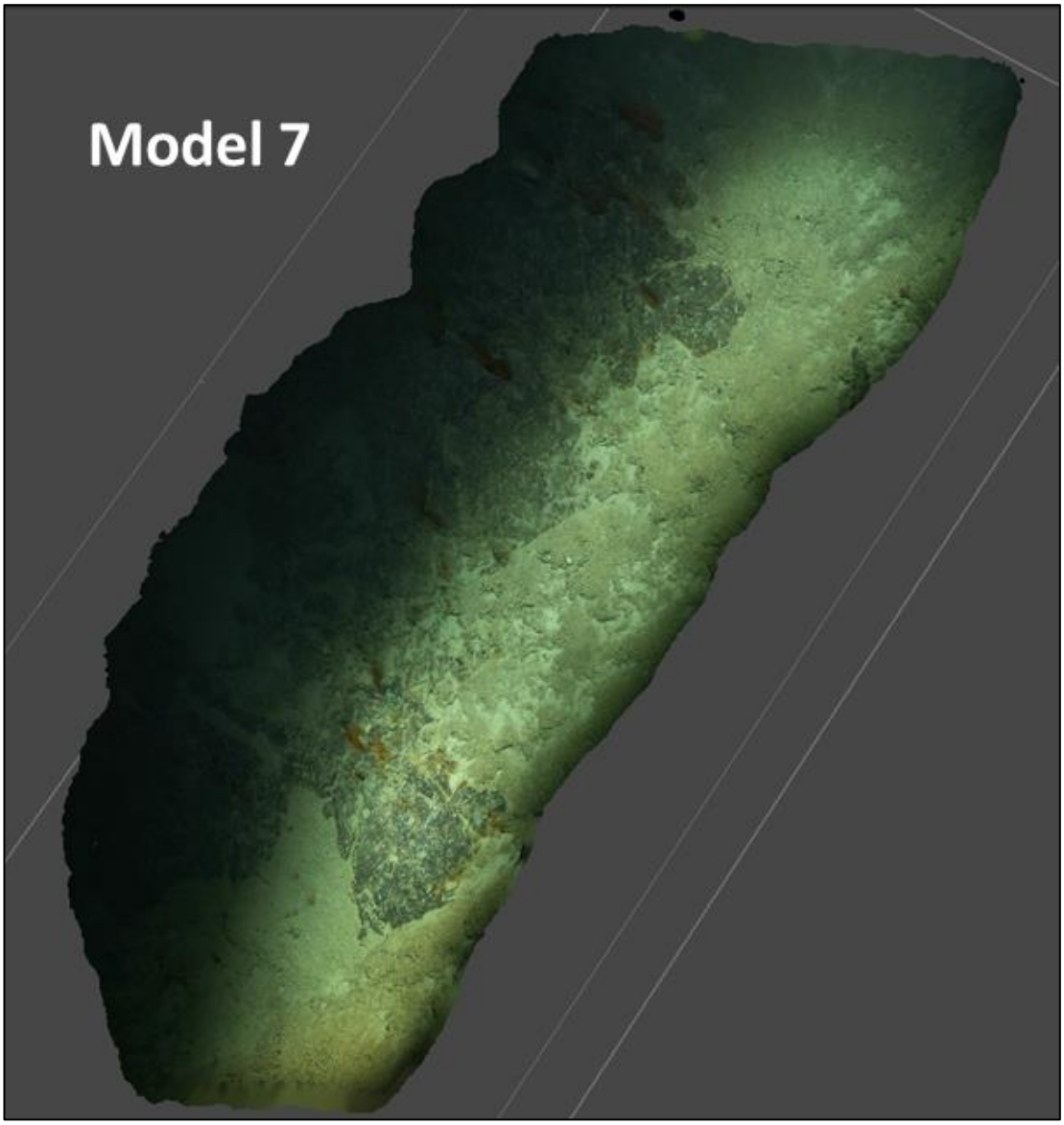


Figure 40: Model 7 from the PBC (approx.. 12 m in length).



Figure 41: Model 8 from the PBC (approx.. 9 m in length).

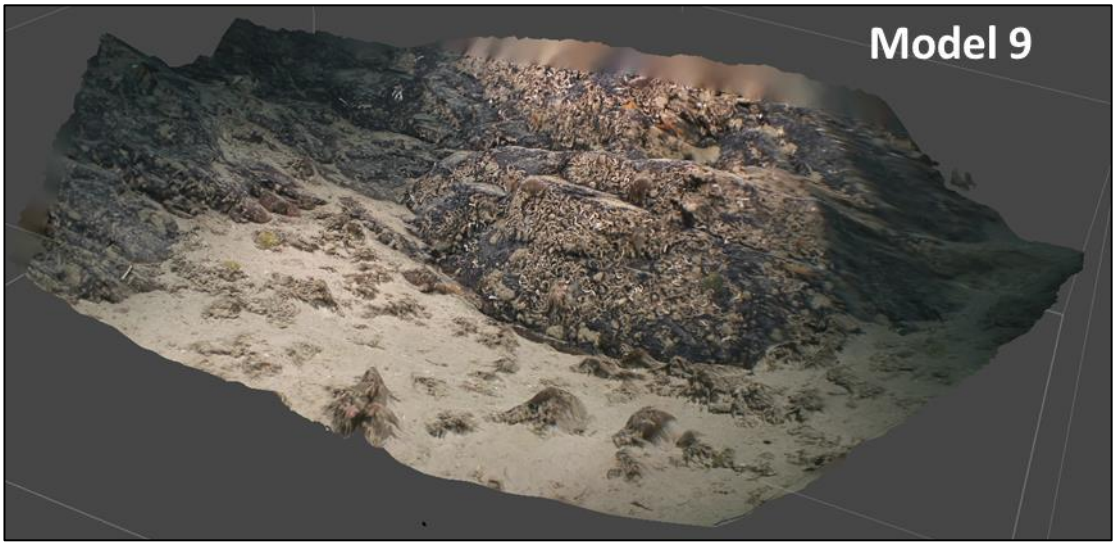


Figure 42: Model 9 from the PBC (approx.. 2 m in length).

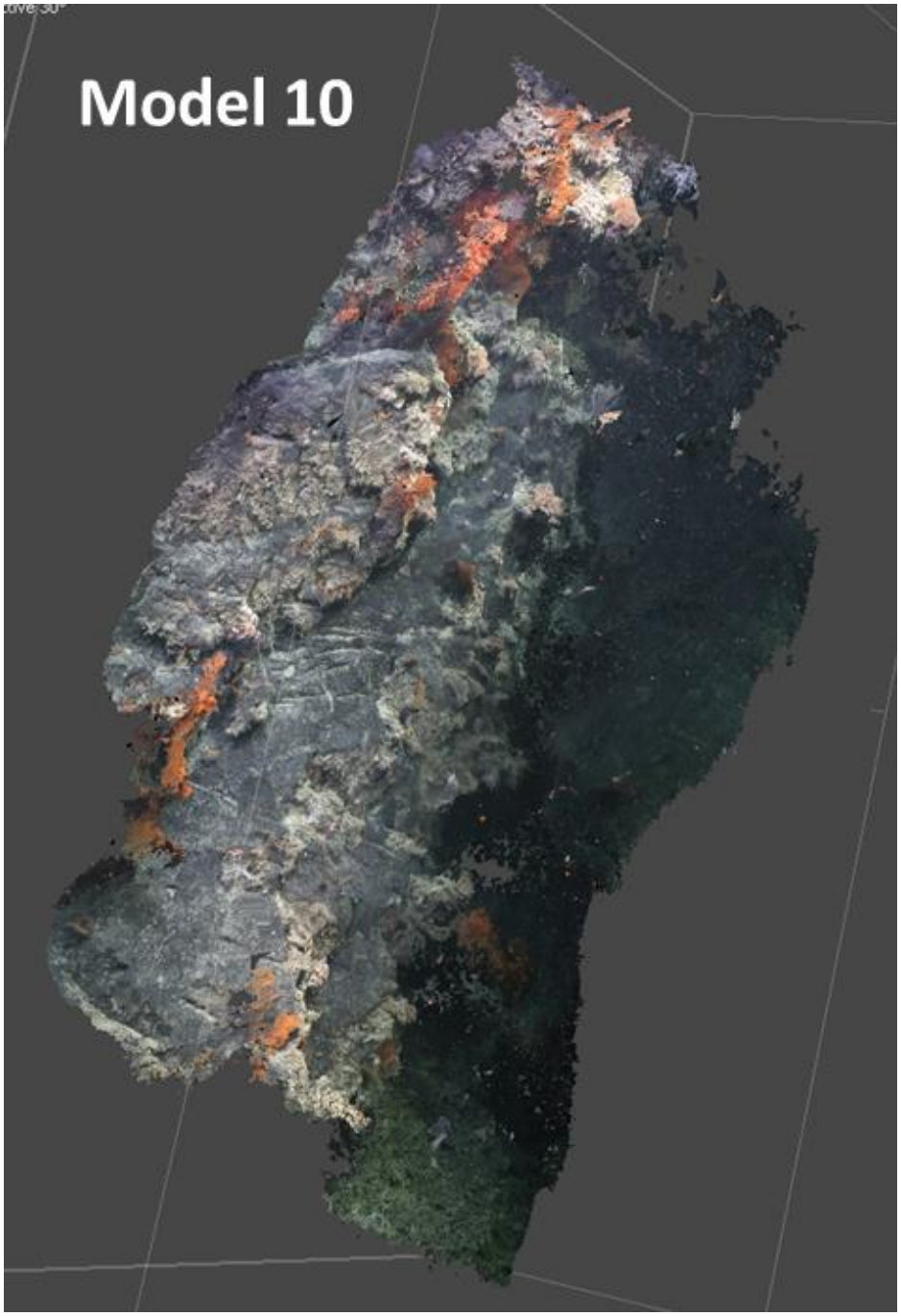


Figure 43: Model 10 from the PBC (approx.. 7 m in length).

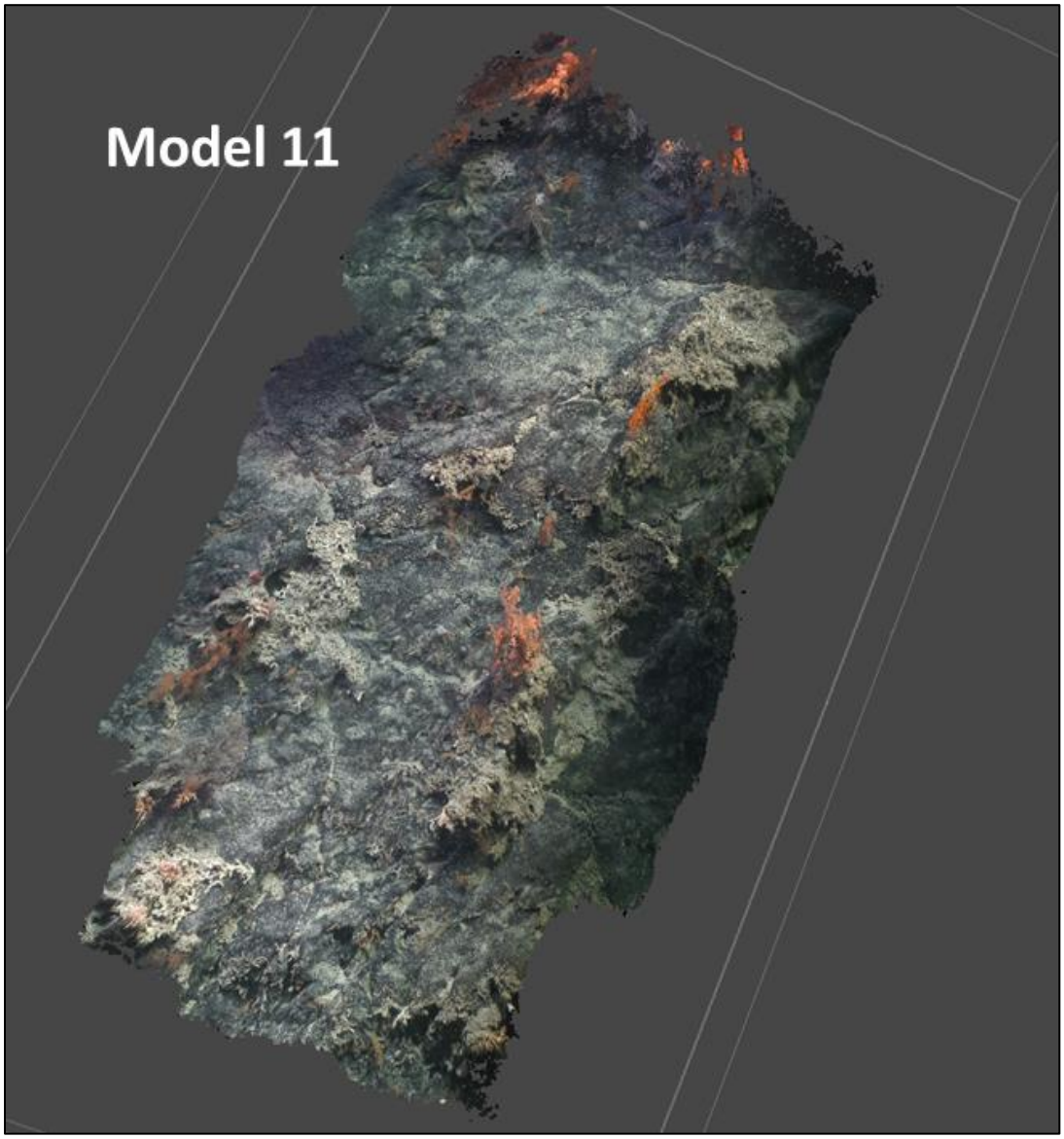


Figure 44: Model 11 from the PBC (approx.. 5 m in length).



Figure 45: Model 12 from the PBC (approx.. 1.5 m in length).

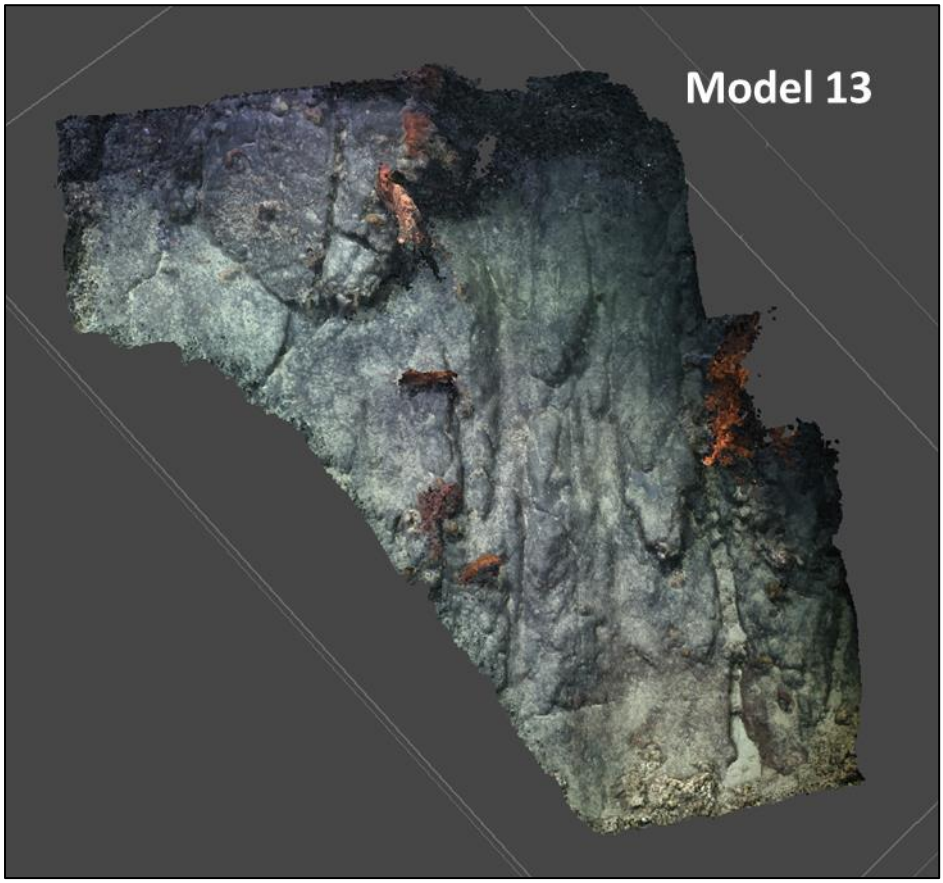


Figure 46: Model 13 from the PBC (approx.. 3 m in length).

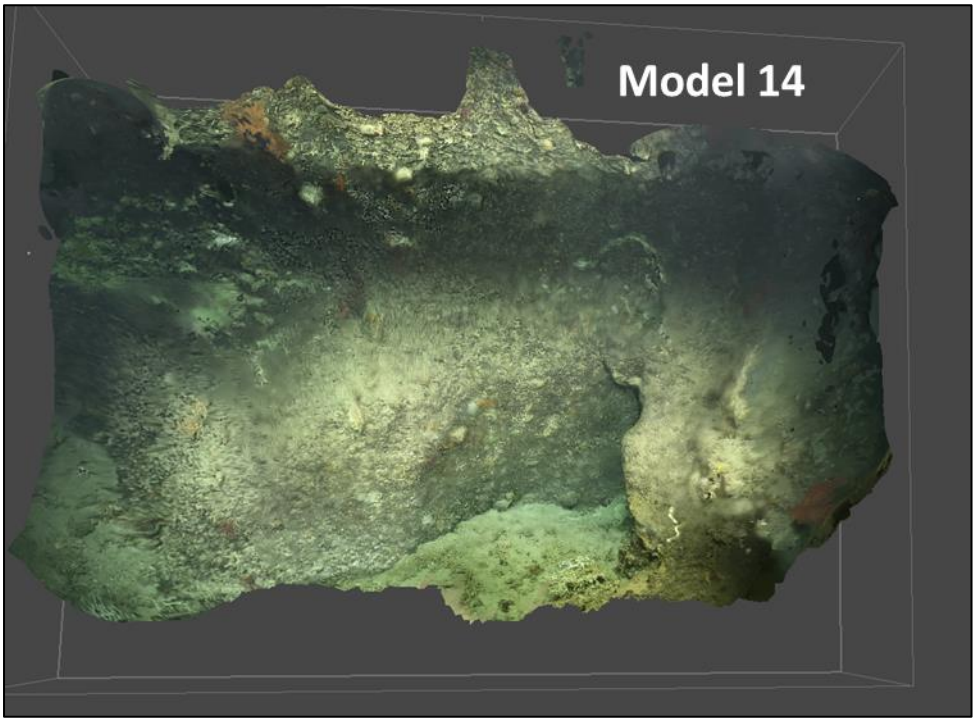


Figure 47: Model 14 from the PBC (approx.. 3 m in length).

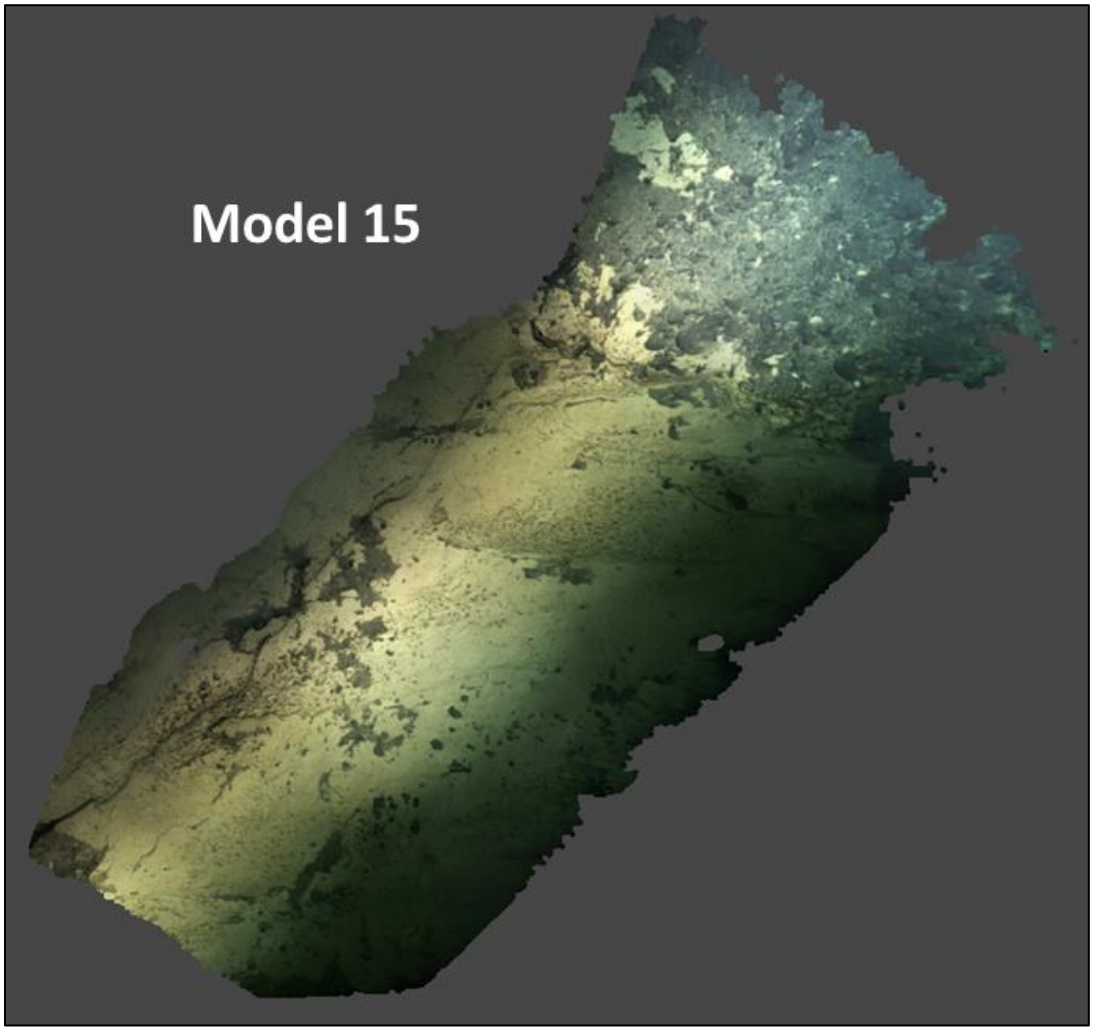


Figure 48: Model 15 from the PBC (approx.. 9 m in length).

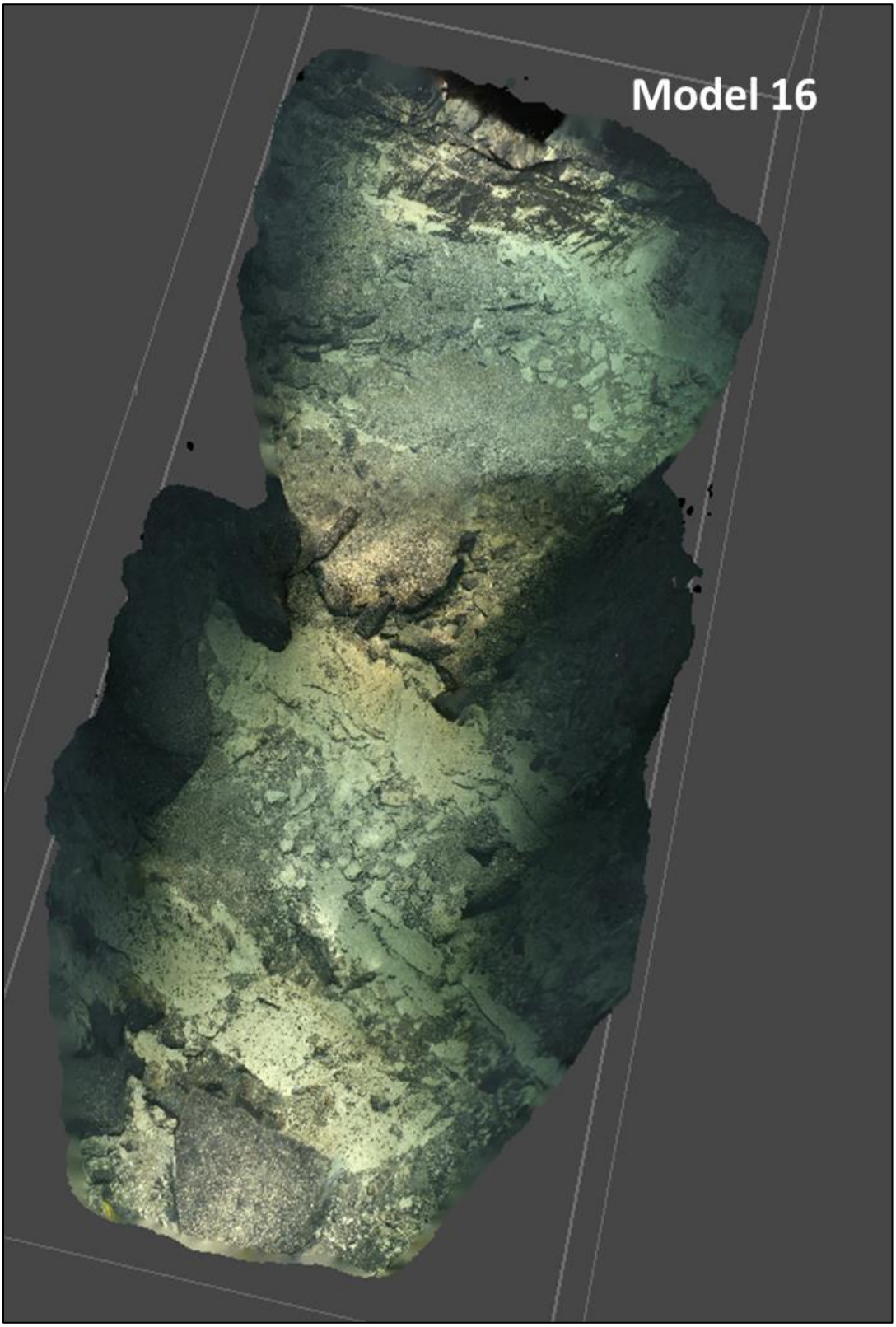


Figure 49: Model 16 from the PBC (approx.. 10 m in length).

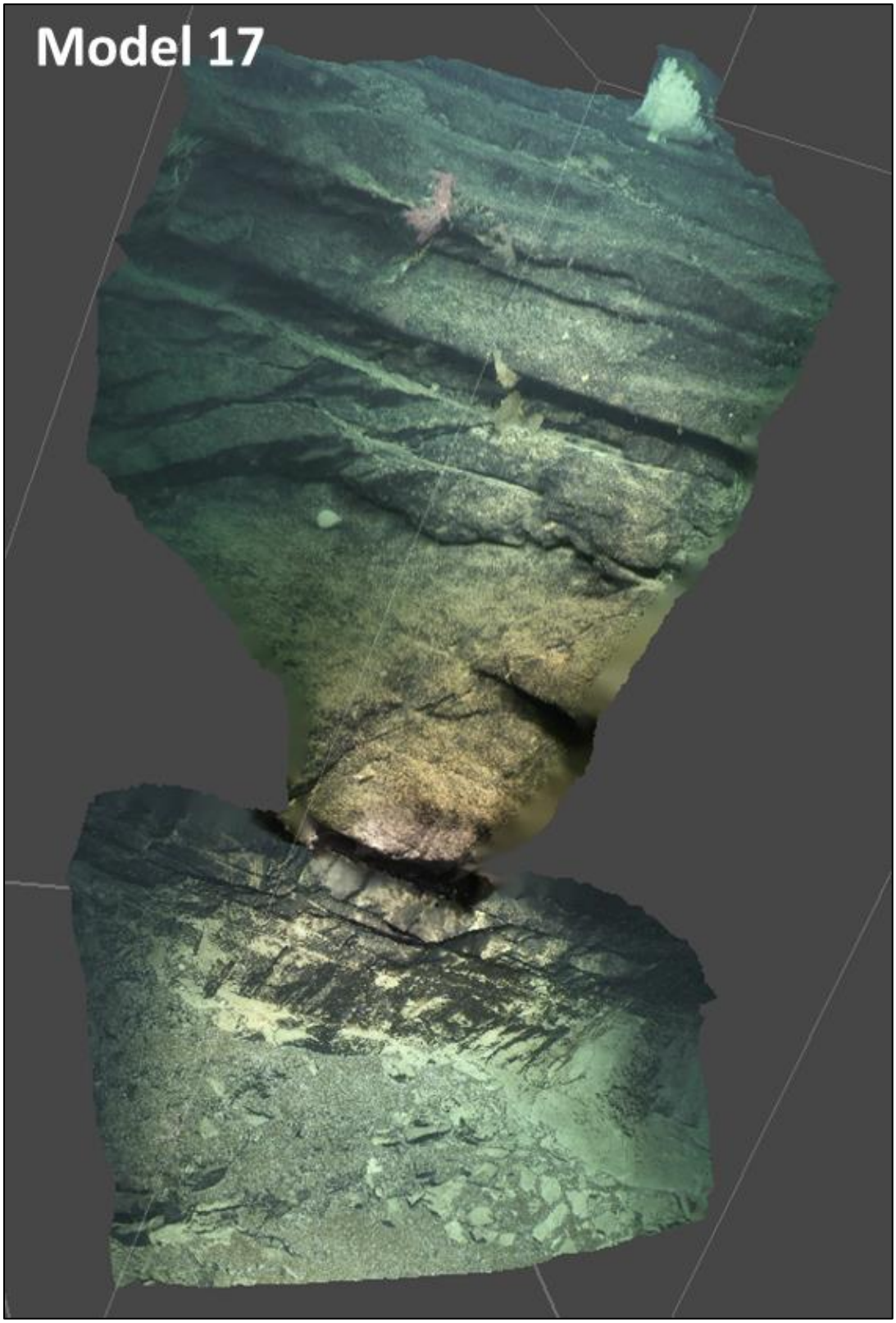


Figure 50: Model 17 from the PBC (approx.. 4 m in length).